A Novel DTFC Based Efficiency and Dynamic Performance Improvement of IPMSM Drive

by

Md. Mizanur Rahman

Submitted in partial fulfillment of the requirements
for the degree of Master of Science in Engineering

Lakehead University
Thunder Bay, Ontario

April, 2016

Abstract

With the advancements in magnetic materials and semiconductor technology, permanent magnet synchronous motor (PMSM) is becoming more and more popular in high power industrial applications due to its high energy density, high power factor, low noise and high efficiency as compared to conventional AC motors. Field oriented vector control (VC) and direct torque and flux control (DTFC) are used for high performance drives. Among these two techniques DTFC is faster and simpler than that of conventional VC scheme as DTFC scheme doesn't need any coordinate transformation, pulse width modulation and current regulators. The DTFC based motor drives utilizes hysteresis band comparators for both torque and flux controls. Both torque and flux are controlled simultaneously by the selection of appropriate voltage vectors from the inverter. However, DTFC suffers from high torque ripples due to discrete nature of control system and limited voltage vectors from the inverter. Torque ripples can be minimized by increasing the sector numbers of the DTFC scheme which increases the switching frequency of the inverter. Traditionally, researchers chose a constant value of reference air-gap flux to make the control task easy but it is not acceptable for high performance drives as the air-gap flux changes with the operating conditions and system disturbances. Furthermore, if the reference air-gap flux is maintained constant, it is not possible to control the motor over the wide speed range operation. Moreover, conventional six-sector based DTFC scheme suffers from high torque ripples, which is the major drawbacks to achieve high dynamic performance.

Therefore, this thesis presents a novel eighteen-sector based DTFC scheme to achieve high dynamic performance with minimum torque ripples. In addition, the loss minimization algorithm (LMA) is incorporated with proposed DTFC scheme in order to improve the efficiency while maintaining high dynamic performance. This thesis further presents modified eighteen-sector based DTFC scheme to overcome the unbalanced voltage effects in any sector of conventional six-sector based system to improve the dynamic performance of the proposed system. This thesis also presents a novel sector determination algorithm to determine the sector number of the stator flux linkage vector which reduces the computational burden to the microprocessor. A five level torque hysteresis comparator based DTFC scheme is also proposed to reduce the torque ripple. Further, a backstepping based nonlinear controller is developed for IPMSM drive that achieves the lowest possible torque ripples in steady state. In this controller development, the control variable is motor electromagnetic developed torque and stator air-gap flux linkages similar to classical DTFC but the errors are forced to zero using backstepping process to get better dynamic performance. The effectiveness of the proposed systems is verified through the development of a simulation model using Matlab/Simulink. Performance of the proposed nonlinear controller is investigated extensively at different operating conditions such as sudden speed and load changes. Then the complete IPMSM drives, incorporating the proposed LMA and eighteen-sector based DTFC scheme and nonlinear controller with torque and flux as virtual control variables are successfully implemented in real-time using digital signal processor (DSP) board-DS1104 board for laboratory 5-hp motor. The effectiveness of the proposed control techniques are verified in both simulation and experiment at different operating conditions. It is found that, the nonlinear controller based IPMSM drive provides the best performance in terms of torque ripple among all the DTFC scheme developed in the thesis. The results show the robustness of the drive and it’s potentiality to apply for real-time industrial drive applications.

Acknowledgements

Firstly, I would like to thank the Almighty Allah who provided me the opportunity to study in Lakehead University and then blessed me with the most precious gift of physical and mental health during the whole study period. Then, I would like to acknowledge and extend thanks to my supervisor Dr. M. N. Uddin for his valuable guidelines and support. He is the person who inspired me from the beginning of my master's degree and I even knocked him at late night for the technical support of the thesis and answered all my queries without being bored. His guidance has been key to the completion of this thesis as well as related works and publications. This work might not be possible without his guidance.

I am also thankful to Dr. K. Natarajan for his valuable suggestions in my graduate seminar which encouraged me to improve the work afterwards. Then, I am also indebted to Ifte Khairul Amin and Zhuoqun Zhai, my lab mates, to share the ideas and to make the healthy and friendly working environment. Thanks are also extended to those members of the engineering department involved in this thesis seminar and defense for dedicating their time and affording valuable feedback.

Last but not least, I like to thank my parents and my sisters for their supplications, patience and moral encouragement to do this job well in time.

Table of Contents

List of Figures

List of Tables

List of Symbols

Symbol	Meaning
v_a, v_b, v_c	a, b and c phase voltages
i_a, i_b, i_c	a, b and c phase currents
$v_{d,} v_q$	d-q axis (rotating reference frame) voltages
$i_{d,} i_q$	d-q axis stator currents (rotating reference frame)
J	moment of inertia of machine rotor
$L_{d,} L_q$	d-q axis inductances
B_m	viscous friction coefficient
$R_{s,} R_c$	stator copper-loss and iron-loss resistance (rotating reference frame)
$i_{cd,} i_{cq}$	d-q axis core-loss armature currents (rotating reference frame)
i_{od}, i_{oq}	d-q axis demagnetizing armature currents (rotating reference frame)
T_e	electrical output torque
P	machine pole pair
θ_r	rotor position
ω_r	motor rotor mechanical speed
ω	motor actual electrical rotor speed
ψ_m	rotor magnetic flux
ψ_s	motor air gap magnetic flux linkage
θ_{sr}	Angle between the stator and rotor flux linkage
P_{cu}, P_{Fe}	copper and iron loss of IPMSM
e_ω, e_T, e_ψ	error terms
k_ω, k_T, k_ψ	design coefficients
^	estimated parameter
·	derivative operation
*	command value
f_{rated}	rated frequency
T_s	sampling frequency in real-time
m_a	amplitude modulation index
m_f	frequency modulation index

List of Abbreviations

Abbreviation	Meaning
DC	Direct current
BLDC	Brushless DC
IM	Induction motor
HPD	High performance drive
PMSM	Permanent magnet synchronous motor
IPMSM	Interior permanent magnet synchronous motor
VSI	Voltage source inverter
CSI	Current source inverter
IGBT	Insulated gate bipolar transistor
VC	Vector control
DTFC	Direct torque and flux control
FLC	Fuzzy logic controller
MTPA	Maximum torque per ampere
FW	Field weakening
LMA	Loss minimization algorithm
NFC	Neuro-fuzzy controller
ANN	Artificial neural network
SC	Search controller
LMC	Loss minimization controller
IEEE	Institute of electrical and electronic engineers
PM	Permanent magnet
FOC	space vector (pulse width modulation)
ABNC	Adaptive backstepping based nonlinear controller
PWM	Pulse width modulation

Chapter 1

Introduction

1.1 Overview of Electric Motors

Electric motors are the major source of electromechanical energy conversion and consuming almost 50% of the generated electrical energy in the world. To serve the daily needs, from small household applications to large industrial plants conventional direct current (DC), induction and synchronous machines are widely used. Due to the increasing demand of electric motors, researchers are trying to develop new machines like the brushless DC (BLDC) machines, the switched reluctance machines, the permanent magnet hysteresis machine and the permanent magnet synchronous machines [1-3]. This reality draws researchers' attention to improve the performance of the electric machines.

DC motors, have dominated the drive system for many decades due to its advantages such as being able to run at wide range of speed, high starting torque for heavy load and can be controlled in a simple way due to the decoupled nature of the field and armature. However, DC motors have many disadvantages such as, robustness, increasing maintenance cost due to the sparking of brushes and commutators, power loss in the filed circuit and lacks of overload capability [4]. Therefore, researchers have developed AC motors such as induction and synchronous motors due to their high reliability and maintenance free operation. Among the AC motors, induction motors (IMs) are almost 70% of the total motors utilized in industry and hence considered as a workhorse in the industry due to their reliability, low maintenance and low cost. Although IMs have several advantageous features but they also suffers from lagging power factor as the rotor voltage is induced from the stator side, not highly efficient due to slip power loss, runs below the synchronous speed and control arrangement is complex [5]. Therefore, for high performance drive (HPD) applications, researchers have developed the synchronous motor which overcome the drawbacks of IMs with running capability at synchronous speed, doesn't have slip power loss and control algorithm is easier as compared to the IMs. However, it requires extra power supply, slip ring and brush gear at the rotor to supply DC field excitations. Thus, conventional synchronous motors need increasing maintenance cost as like as dc motors. Due to these disadvantages, the permanent magnet motor has been developed where the permanent magnets produce the flux and hence, the loss due to rotor winding is avoided [6]. The permanent magnet synchronous motor (PMSM) is becoming popular from the last two decades due to some of its advantageous features such as, high power to weight ratio, high efficiency, high reliability, high power factor, low noise and robustness.

1.2 Overview of PM Motors

With the advent of high energy rare earth magnetic material such as, neodymium-iron-boron (NdFeB), PMSM is becoming more and more popular for its several advantageous features. Depending on the position of permanent magnets on the rotor, PMSM can be divided into three categories; surface mounted type, where the permanent magnets are mounted on the surface of the rotor core and these type of PMSMs are not suitable for high speed application; inset type of PMSM where permanent magnets are typically glued or banded with a non-conducting material inside the rotor core; interior type PMSM (IPMSM), where the permanent magnets are buried with the rotor core [7]. IPMSM offers q-axis inductance higher than the d-axis inductance which enables the flux weakening operation therefore motor can be operated above the rated speed at constant voltage. This saliency adds the reluctance torque. Interior type permanent magnet synchronous motor (IPMSM) has the mechanical robustness with smaller magnetic air gap. These three types of PMSM are shown in Figs. 1.1, 1.2 and 1.3, respectively.

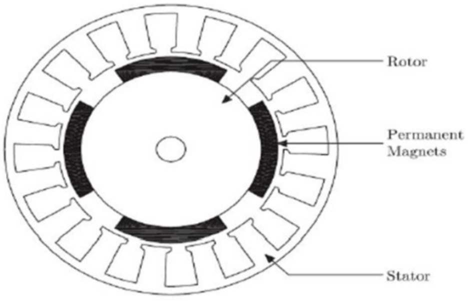

Fig. 1.1: Cross section of surface mounted PMSM.

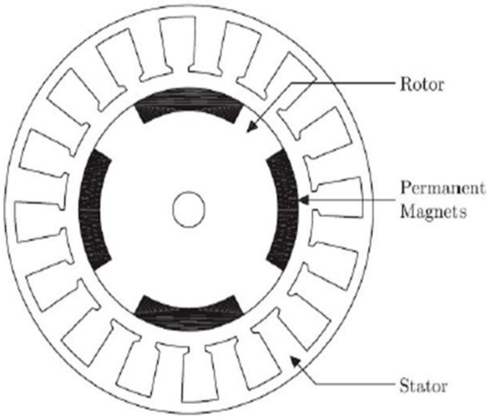

Fig. 1.2: Cross section of inset type PMSM.

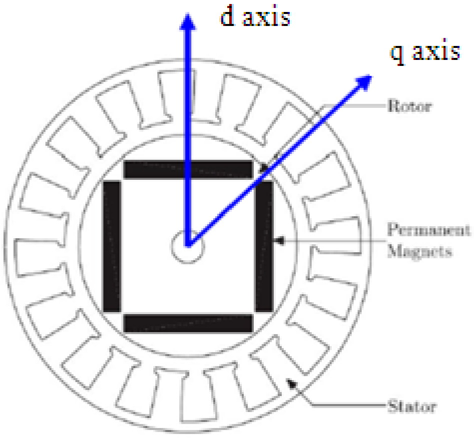

Fig. 1.3: Cross section of interior type PMSM.

Depending on the orientation of the magnets, the PM motors can be classified into three types: (a) radial type, (b) circumferential type and (c) axial type. For the surface mounted type, the orientation of magnetization is only radial where the magnetic force is perpendicular to the length of the motor/shaft. For the inset and interior types, the orientation of magnetization can be either radial or circumferential. In axial type flux motors, the magnetic force is along the same plane as the motor shaft (along the length of the motor). Depending on the rotor cage winding, the PM motors can be classified as: (a) cageless where the rotor has no cage winding and (b) cage type where the rotor is provided with the cage winding which provides starting torque and hence it is self-starting motor. As the cageless motor is operated from the voltage source inverter (VSI), proper control techniques plays the vital role so that motor can start smoothly up to the synchronous speed from standstill condition which eliminates the use of cage type PM motor.

PM synchronous motors can be used for high speed railways because it offers higher power density which decreases the weight ratio. PMSM drives are used in HPD applications such as robotics, rolling mills, tractions, spindle drives and machine tools. Among different types of PM motors, the IPMSM with radial magnetization is the most economical for manufacturing process. In addition, as the permanent magnets are buried inside the rotor core, it provides smooth rotor surface with reduced air gap. Therefore, IPMSM can be used for wide speed range of operation with better dynamic performance. That's why IPMSM is considered as a working model in this thesis [8].

1.3 Literature Review

This section of the thesis provides an overview of current research works on PMSM drives. Significant research has been performed in the field of PMSM drives. As this thesis pertains specifically to IPMSM drives, research dedicated to this specific class of PMSM will be focused on. Researchers normally concentrate on two types of control of IPMSM drives,

1. Vector control (VC)
2. Direct torque and flux control (DTFC)

Researchers either reported their works on the development of high performance IPMSM drives fed by either voltage source or current source inverter [9, 10]. Typical motor drive systems employ a 2-level three phase voltage source inverter (VSI) for commutation of the motor stator phases, and thus a simplified diagram of this configuration is shown in Fig. 1.4.

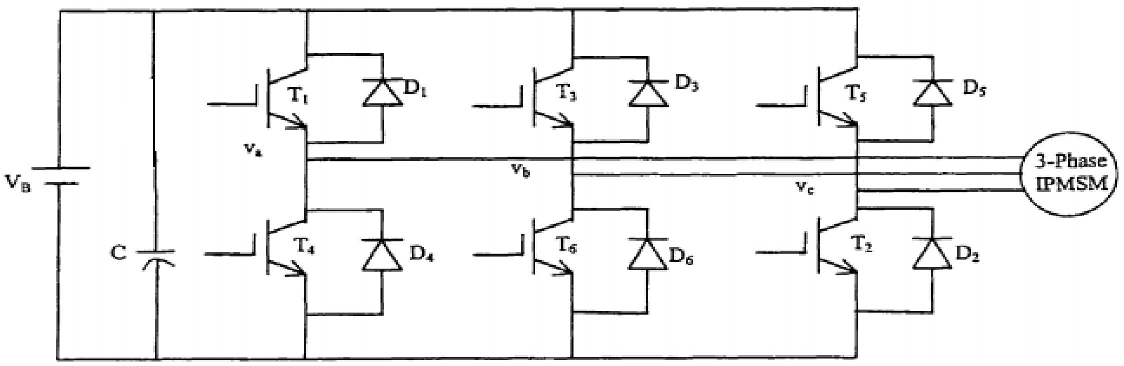

Fig. 1.4: Typical 3-phase, 2-level inverter.

For high performance drive both VC and DTFC techniques are used in AC motor drives to achieve fast and accurate speed. In VC techniques, stator voltages and currents are decomposed into d and q axis components where d-axis controls the magnetic flux and q-axis controls the torque. Thus, the IPMSM motor behaves like a separately excited DC motor while maintaining its general advantages over DC motor. A typical closed loop VC scheme of the PMSM is shown in Fig. 1.5

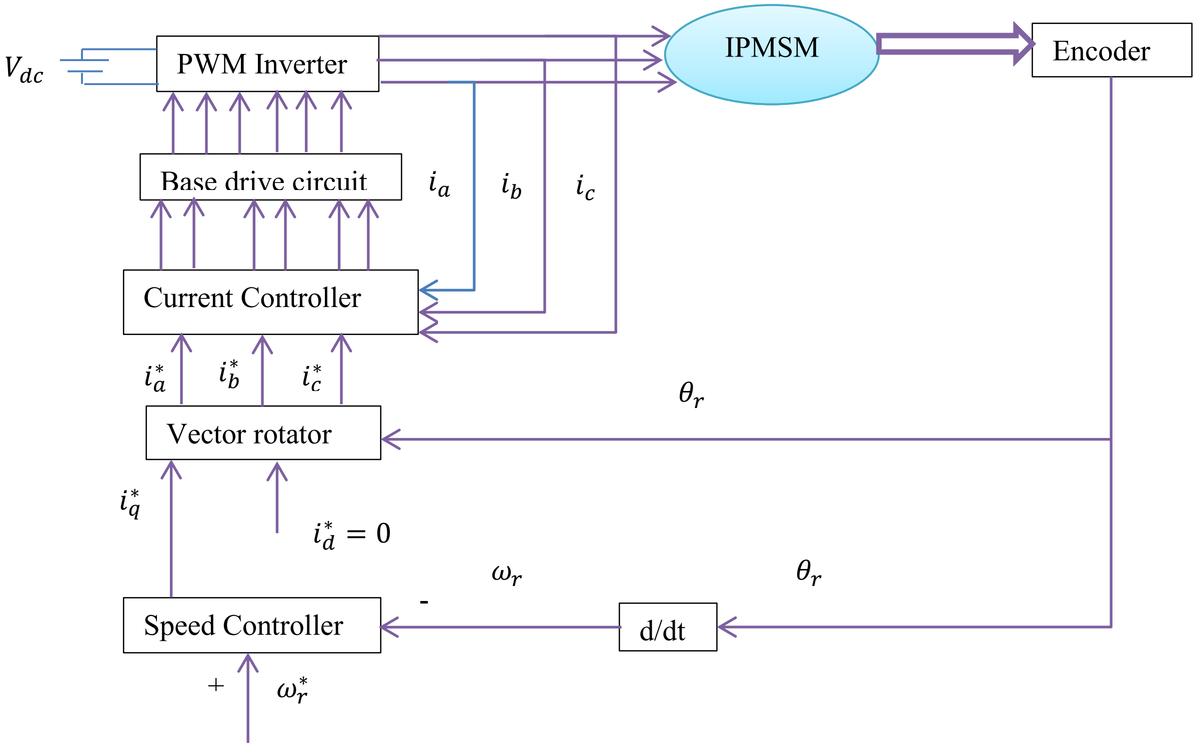

Fig. 1.5: Block diagram of the vector control scheme of the IPMSM drive.

In [9], to analyze the steady state performance of a VSI fed PMSM drive a vector control scheme is proposed and the current source inverter (CSI) fed PMSM is proposed in [10]. For both control schemes, a position feedback controller is used from a shaft position sensor so that inverter can operate in self-control mode. Other form of PMSM control is DTFC which was initially introduced for induction machines as it provides high dynamic performance which can be directly controlled from the control parameter of DTFC. DTFC uses motor stator air-gap flux linkage vector and output torque as control variables whereas VC utilizes three phase stator currents. A typical DTFC control scheme is shown in Fig. 1.6.

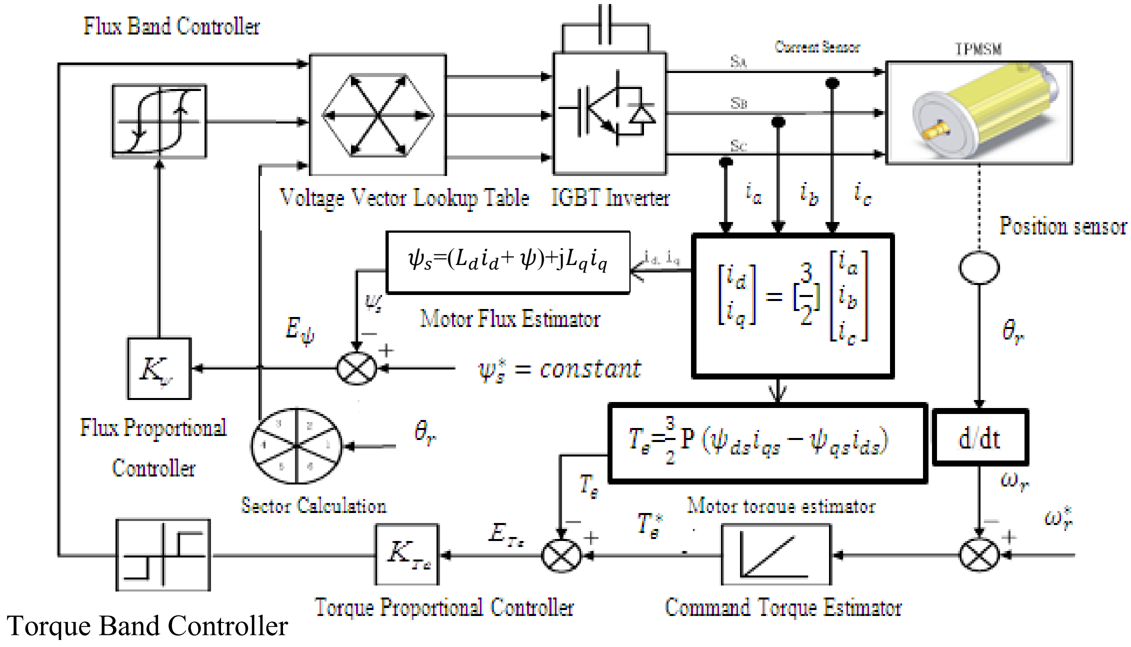

Fig. 1.6: Block diagram of the direct torque and flux control scheme of the IPMSM drive.

In [11], authors considered constant reference flux based conventional DTFC but utilized fuzzy logic controller (FLC) to improve the dynamic performance under varying dynamic conditions for induction motors (IMs). However, the DTFC still suffers from high torque ripple and hence, the motor vibrates in steady state. The reference air-gap flux for the DTFC scheme can be controlled by using either maximum torque per ampere (MTPA) control and flux weakening (FW) control to operate the motor below and above the rated speed, respectively. In [12], a varying reference flux through loss minimization algorithm (LMA) was proposed but the DTFC was conventional one.

In [13], d and q axis currents are derived from the MTPA for the reference flux estimation for DTFC scheme of PMSM drive which optimizes the reference flux. Authors considered approximation method to calculate the flux from torque hence the system suffers from torque ripples. In [14], reference flux is estimated through online search algorithm of MTPA which is based on signal injection method. For the search control of MTPA region only stator resistance is required. The proposed work suffers from high ripples for both mechanical speeds and torque.

In [15], a novel band adaptation algorithm for a three level torque hysteresis comparator was proposed for DTFC control of IM. Authors developed the band adaptation algorithm based on the slope of the estimated torque of the motor which reduces the need of extra sensor but the proposed system contains higher torque ripples at steady state. In [16], a model reference adaptive flux observer based neuro-fuzzy controller (NFC) was proposed for IM drive where d-axis reference flux linkage of the indirect field oriented control is provided by the flux weakening method and NFC is utilized as the speed controller. The authors reported fuzzy logic with the five layer artificial neural network (ANN) where in the 4th layer errors are minimized through online tuning algorithm. The proposed work suffers from higher ripples in the speed response at steady state.

In [17], DTC with flux weakening control was reported. The control scheme only requires armature resistance. Authors only reported the control algorithm but didn’t consider the efficiency issue. In [18], authors proposed a new technique for the estimation of the magnetic flux in permanent magnet synchronous machines based on field reconstruction. The distribution of the magnetic field in the air gap is independent from stator resistance value and hence errors are removed. On the other hand, there is no integration with respect to time. In [19], authors reported minimum torque ripple control while maintaining constant switching frequency for IMs. Authors derived an rms torque-ripple equation using instantaneous torque equations and minimum torque ripple condition is determined based on the torque equations. Authors claimed that the proposed algorithm improves the dynamic performance but still the torque response suffers from ripples at steady state and trajectory of the stator flux contains ripples which demonstrate the increase of the torque ripples in high speed regions as torque frequency increase with the motor speed.

In [20], a torque ripple reduction technique of direct torque control (DTC) for high power IMs driven by three-level inverters with lower switching frequency was presented. Authors claimed that, if the voltage selection is done by intermediate voltage vectors then stator flux demagnetization at low speeds could be resolved and torque ripples could be reduced by 30%. In [21], authors proposed the voltage vector selection strategy with the information of stator flux position and torque angles and utilize the space vector modulation (SVM) techniques to generate the voltage vectors.

In [22], space vector modulation (SVM) based DTFC scheme is proposed for IPMSM drive. A SVM unit generates the reference voltage vectors so that the look-up table in the conventional DTFC is replaced. The proposed, DTFC improves the dynamic performance of the DTFC scheme as compared to the conventional DTFC. It was seen that the SVM can reduce the harmonics in the motor currents. The proposed work suffers from the overshoot problem in the speed response and torque response contains higher ripples in the steady state.

Some of the researchers incorporate the intelligent control techniques such as fuzzy, neuro-fuzzy, artificial neural networks to improve the dynamic performance of the drive system where intelligent controllers are used to adjust the bandwidth of the torque hysteresis comparators. In [23], a novel duty cycle control strategy is proposed to reduce both torque and flux ripples where three vectors are applied during one control period. In the proposed method, null vectors are utilized to reduce the torque ripples and flux ripple is reduced by the duty ratios.

As mentioned earlier, estimation of stator air-gap flux is important for DTFC. In [24], based on stator currents and rotor position stator flux is estimated for surface mounted PMSM drive and performs better. The operating speed range was extended due to flux estimation [24]. But the proposed system shows better performance only for the low speed region but suffers from high ripples in the extended speed region.

In [25], researchers reported neural network controller to replace switching table of DTFC to achieve high torque response. In [26], authors reported fuzzy controller to replace the conventional hysteresis controller and estimates the stator resistance online using the learning capability of neural networks. Therefore, torque ripples are greatly reduced. In [27], ANN based on Kalman filter is used to replace the PI controller to get the better response. Proposed system has faster system response, smaller overshoot as compared to the conventional PI for DTFC of PMSM drive.

In [28], authors presented an adaptive control to find the maximum efficiency operating point where efficiency control measures the current on the DC link and adjusts the voltage output of the inverter to minimize the input power to the PMSM drive. In [29], authors reported that for the search controller (SC) the input power is not distinct for large efficiency motor. Meanwhile, air-gap flux oscillations create large torque ripples. Authors concluded that the loss minimization through the stator current is easier as compared to the loss minimization through the minimum input power to get the higher efficiency.

In [30], loss model based controller (LMC) was used to determine the flux level of IM for efficiency optimization of IMs. In order to build a simple loss model, the induction motor model is referenced to the rotor magnetizing current so there is no leakage inductance on the rotor side. Although the proposed LMC based LMA is simple but the proposed drive suffers from higher torque ripples both in transient and steady state conditions. In [31], copper and iron losses are minimized by the optimal control of the armature current vector. Authors determined the optimal current vector based on the operating speed and load conditions. Reluctance torque and flux weakening effects are utilized to minimize the controllable PMSM losses. In [32], command flux for DTFC is obtained through optimization procedure to get optimum efficiency over a wide speed range. Authors claimed that, the optimum voltage vector selection provides faster torque response for PMSM drive.

In [33], an online adaptive loss minimization controller for IPMSM drive was presented. The LMC provides novel pattern of change in d-axis current to get minimum input power at any operating conditions. In [34], efficiency optimization control algorithm is presented to minimize the electrical losses of the motor. In [35], authors incorporated both the SC and LMC to control the drive where LMC is used to get the optimum d-axis current so that search interval is reduced and convergence time of the SC algorithm is shortened which avoids the parameter variation.

1.4 Thesis Motivation

DTFC eliminates the use of current controllers which provides the higher dynamic performance of PMSM drive. Despite several advantages, DTFC suffers from high torque ripples in steady state which is a major drawback to achieve high dynamic performance. Therefore, a lot of research is going on to overcome the drawbacks of conventional DTFC. As inverter switching plays an important role to reduce the torque ripples, most of the research reported the development of various inverter control algorithms. In DTFC motor torque and stator air-gap flux linkages are control variables where actual motor torque and flux linkage are compared with their reference values to get the corresponding error variables. Based on these errors the flux and torque hysteresis controller generates the logic signals for voltage vector look up table. Therefore, flux estimation plays an important role for the DTFC scheme to get better speed and dynamic response. Researchers normally consider constant air-gap flux which hinders the speed control of IPMSM over the rated speed and at the same time suffers from high torque ripples. On the other hand, air-gap flux varies with the operating conditions. Again, with the constant air-gap flux, efficiency of IPMSM cannot be optimized. Traditionally, conventional six-sector based DTFC scheme is used. Therefore, torque ripple can be minimized by increasing the sector number for DTFC. Furthermore, conventional three level torque hysteresis comparators can be modified up to five level torque hysteresis comparators with modified sectors to get higher dynamic performance.

Therefore, this thesis makes an attempt to estimate the reference flux for the DTFC to cope with variable operating conditions. An LMA based flux estimator is incorporated in the DTFC scheme to minimize the motor electrical losses and hence to optimize the motor efficiency. Furthermore, conventional six-sector are modified into eighteen-sector incorporating LMA to minimize the torque ripple while maintaining high efficiency. This thesis further attempts to modify conventional three level torque hysteresis comparators into five level torque hysteresis comparators to maintain high dynamic performance. Finally, an adaptive backstepping based nonlinear controller is developed which achieved the lowest torque ripple among all the methods developed in this thesis.

1.5 Thesis Organization

This thesis is arranged according to major section titles pertaining to the principal focus areas of the thesis. Subsections address specific detail, and contain pertinent figures, charts, or tables and/or appropriate references.

In Chapter 1, review of literature of existing work on the conventional DTFC of PMSM is detailed, and a motivation for the thesis work is provided. Comprehensive overview of the classical DTFC scheme of IPMSM drive is also discussed.

In Chapter 2, detailed derivations of all pertinent mathematical models used in the thesis, including reference frame conversion, and synchronous machine modelling are detailed. Comparative system performance analysis of VC and DTFC is also detailed.

In Chapter 3, the development of the proposed eighteen-sector based DTFC scheme incorporating LMA are provided. Finally, five level torque hysteresis comparator developments with modified sectors and circular flux tracking is also provided.

In Chapter 4, results from multiple simulation environments are presented. The performance of the proposed DTFC scheme is established through a series of tests, including load variation, set-point changes and sectors modifications.

In Chapter 5, real-time system development of the DTFC schemes are presented. Results demonstrating the robust performance through a series of tests similar to those performed in simulation.

In Chapter 6, the development of the proposed nonlinear control algorithm of IPMSM drive is detailed. Controller is developed taking consideration of torque and flux as virtual control variable and stability is verified by the Lyapunov’s stability theory.

In Chapter 7, summary of the thesis results and findings, the contributions made and future work potential to improve the current work are detailed.

Chapter 2

IPMSM Drive Mathematical Modeling

2.1 Introduction

Analytically, the IPMSM is same as the conventional wire wound excited synchronous motor with the exception that the excitation is provided by the permanent magnets instead of wire wound dc rotor field. Therefore, the standard d-q axis model for synchronous machines can be used for the d-q axis model of the IPMSM by removing the equations related to field current and associated dynamics.

This section of the thesis details the mathematical model development of IPMSM and operating principle of conventional DTFC. The d axis refers to the ‘‘direct’’ axis which is aligned with the direction of magnetic flux (i.e. along north-south pole orientation). The q axis (quadrature axis) is 90 degree electrically apart from the positive d axis that is the convention of Institute of Electrical and Electronic Engineers (IEEE) [36].

2.2 IPMSM Mathematical Model Development

If Ψ is the constant flux provided by the permanent magnets; then the flux linkage in the three phase stator winding due to the permanent magnets (PM) in the rotor is given by,

$$\begin{bmatrix}\Psi_{am}\\ \Psi_{bm}\\ \Psi_{cm}\end{bmatrix} = \Psi\begin{bmatrix}\sin\theta_r\\ \sin(\theta_r-\frac{2\pi}{3})\\ \sin(\theta_r+\frac{2\pi}{3})\end{bmatrix} \tag{2.1}$$

where, Ψ_{am}, Ψ_{bm} and Ψ_{cm} are the flux linkages in three phase stator winding due to the permanent magnets in the rotor and θ_r is the rotor position. Total air gap flux linkage for three phases is the summation of the flux linkage for the corresponding phase current, mutual flux linkage for currents in the other phases and the flux linkages in the three phase stator winding due to the PM in the rotor. Three phase air gap flux linkage is given by,

$$\begin{bmatrix}\Psi_a\\ \Psi_b\\ \Psi_c\end{bmatrix}=\begin{bmatrix}\mathrm{L_{aa}} & \mathrm{M_{ab}} & \mathrm{M_{ac}}\\ \mathrm{M_{ba}} & \mathrm{L_{bb}} & \mathrm{M_{bc}}\\ \mathrm{M_{ca}} & \mathrm{M_{cb}} & \mathrm{L_{cc}}\end{bmatrix}\begin{bmatrix}i_a\\ i_b\\ i_c\end{bmatrix}+\Psi\begin{bmatrix}\sin\theta_\mathrm{r}\\ \sin(\theta_\mathrm{r}-\frac{2\pi}{3})\\ \sin(\theta_\mathrm{r}+\frac{2\pi}{3})\end{bmatrix} \tag{2.2}$$

where: Ψ_a, Ψ_b, Ψ_c = per phase magnetic flux

$\mathrm{L_{aa}}, \mathrm{L_{bb}}, \mathrm{L_{cc}}$ = per phase self-inductance

$\mathrm{M_{ab}}, \mathrm{M_{bc}}, \mathrm{M_{ca}}$= per phase mutual-inductance

The phase voltage is the voltage drop in each phase plus the voltage drop due to the rate of change of flux linkage. For IPMSM, three phase voltage can be developed as,

$$\begin{bmatrix}v_a\\ v_b\\ v_c\end{bmatrix}=\begin{bmatrix}r_a & 0 & 0\\ 0 & r_b & 0\\ 0 & 0 & r_c\end{bmatrix}\begin{bmatrix}i_a\\ i_b\\ i_c\end{bmatrix}+\frac{\mathrm{d}}{\mathrm{dt}}\begin{bmatrix}\Psi_a\\ \Psi_b\\ \Psi_c\end{bmatrix} \tag{2.3}$$

where: v_a, v_b, v_c = stator phase voltages

i_a, i_b, i_c = stator phase current

r_a, r_b, r_c = stator phase resistance

Thus, the net synchronous motor mathematical model in the ‘‘abc’’reference frame can be written as,

$$\begin{bmatrix}v_a\\ v_b\\ v_c\end{bmatrix}=\begin{bmatrix}r_a & 0 & 0\\ 0 & r_b & 0\\ 0 & 0 & r_c\end{bmatrix}\begin{bmatrix}i_a\\ i_b\\ i_c\end{bmatrix}+\frac{\mathrm{d}}{\mathrm{dt}}\left\{\begin{bmatrix}L_{aa} & M_{ab} & M_{ac}\\ M_{ba} & L_{bb} & M_{bc}\\ M_{ca} & M_{cb} & L_{cc}\end{bmatrix}\begin{bmatrix}i_a\\ i_b\\ i_c\end{bmatrix}+\Psi\begin{bmatrix}\sin\theta_\mathrm{r}\\ \sin(\theta_\mathrm{r}-\frac{2\pi}{3})\\ \sin(\theta_\mathrm{r}+\frac{2\pi}{3})\end{bmatrix}\right\} \tag{2.4}$$

These three phase voltage equations are dependent on the flux linkage components which are a function of rotor position, θ_r and the coefficients of the voltage equations are time varying with the exception if the motor is motionless. In order to keep away from the difficulty of calculations, all the equations have to be changed into synchronously revolving rotor reference frame where the machine equations are no longer dependent on the rotor position, θ_r. These transformations can be accomplished in two steps using Park's and Clark's transformation equations. In Clark's transformation, machine equations are changed from the balanced a-b-c frame into balanced two-phase quadrature quantities, d-q. In Park's transformation, machine equations are converted from balanced two-phase orthogonal stationary system into orthogonal rotating reference frame, d^r-q^r. In these transformations, d-q axes are orthogonal to each other but in the same plane as the three phase reference frame. The transformation is shown in Fig. 2.1.

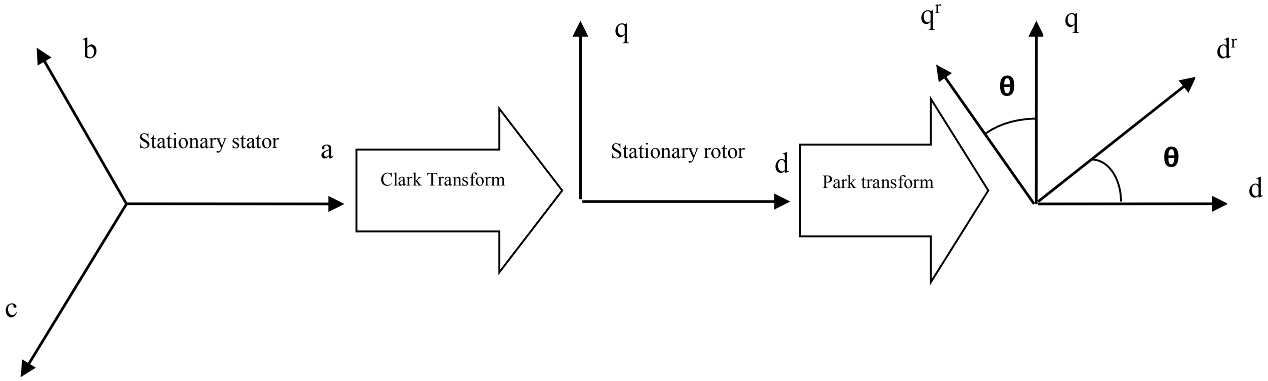

Fig. 2.1: Forward reference frame conversion.

In orthogonal rotating reference frame, d^r is at an angle **θ** (rotation angle) to the d axis and q^r is perpendicular to d^r along the q axis. The phase variables in terms of d-q-0 can be written in matrix form,

$$\begin{bmatrix} x_a \\ x_b \\ x_c \end{bmatrix} = \begin{bmatrix} \cos\theta_r & \sin\theta_r & 1 \\ \cos(\theta_r - \frac{2\pi}{3}) & \sin(\theta_r - \frac{2\pi}{3}) & 1 \\ \cos(\theta_r + \frac{2\pi}{3}) & \sin(\theta_r + \frac{2\pi}{3}) & 1 \end{bmatrix} \begin{bmatrix} x_q \\ x_d \\ x_0 \end{bmatrix} \quad (2.5)$$

Corresponding inverse relation can be written as,

$$\begin{bmatrix} x_q \\ x_d \\ x_0 \end{bmatrix} = \frac{2}{3} \begin{bmatrix} \cos\theta_r & \cos(\theta_r - \frac{2\pi}{3}) & \cos(\theta_r + \frac{2\pi}{3}) \\ \sin\theta_r & \sin(\theta_r - \frac{2\pi}{3}) & \sin(\theta_r + \frac{2\pi}{3}) \\ \frac{1}{2} & \frac{1}{2} & \frac{1}{2} \end{bmatrix} \begin{bmatrix} x_a \\ x_b \\ x_c \end{bmatrix} \tag{2.6}$$

where, the variable (x) could be voltage (v) or current (i).

The rotor position is defined as,

$$\theta_r = \int_0^t \omega_r\,(t)dt + \theta_r(0) \tag{2.7}$$

where: ω_r = angular velocity
$\theta_r(0)$ = rotor initial position

For balanced three phase system, zero sequence components (x_0) does not exist and the rotor's initial position, $\theta_r(0) = 0$. Therefore, q axis coincides with the phase ''a''. Under these conditions the Equation (2.6) can be written as,

$$\begin{bmatrix} x_q \\ x_d \end{bmatrix} = \begin{bmatrix} \frac{2}{3} & \frac{-1}{3} & \frac{-1}{3} \\ 0 & \frac{-1}{\sqrt{3}} & \frac{1}{\sqrt{3}} \end{bmatrix} \begin{bmatrix} x_a \\ x_b \\ x_c \end{bmatrix} \tag{2.8}$$

The quantities in the stationary d-q frame can be converted to synchronously rotating d^r-q^r frame where,

$$\begin{bmatrix} x_q^r \\ x_d^r \end{bmatrix} = \begin{bmatrix} \cos\theta_r & -\sin\theta_r \\ \sin\theta_r & \cos\theta_r \end{bmatrix} \begin{bmatrix} x_q \\ x_d \end{bmatrix} \tag{2.9}$$

Inverse relation is given by,

$$\begin{bmatrix} x_q \\ x_d \end{bmatrix} = \begin{bmatrix} \cos\theta_r & \sin\theta_r \\ -\sin\theta_r & \cos\theta_r \end{bmatrix} \begin{bmatrix} x_q^r \\ x_d^r \end{bmatrix} \tag{2.10}$$

Therefore, using the entire relations d^r-q^r model of IPMSM can be derived as,

$$v_q{}^r = Ri_q{}^r + \frac{d\Psi_q{}^r}{dt} + \omega_s \Psi_d{}^r \tag{2.11}$$

$$v_d{}^r = Ri_d{}^r + \frac{d\Psi_d{}^r}{dt} - \omega_s \Psi_q{}^r \tag{2.12}$$

where: $v_d{}^r$, $v_q{}^r$ = d and q axis voltages

$i_d{}^r$, $i_q{}^r$ = d and q axis currents

$\Psi_d{}^r, \Psi_q{}^r$ = d and q flux linkages

ω_s = stator frequency

d and q axis flux linkages can be written as,

$$\Psi_q{}^r = L_q i_q{}^r \text{and } \Psi_d{}^r = L_d i_d{}^r + \Psi \tag{2.13}$$

Therefore, q-axis voltage model can be written as,

$$\begin{aligned} v_q{}^r = Ri_q{}^r + \frac{d\Psi_q{}^r}{dt} + \omega_s \Psi_d{}^r &= Ri_q{}^r + (d/dt)L_q i_q{}^r + P\omega_r(L_d i_d{}^r + \Psi) \\ &= Ri_q{}^r + (d/dt)L_q i_q{}^r + P\omega_r L_d i_d{}^r + P\omega_r \Psi \end{aligned} \tag{2.14}$$

For the d-axis model,

$$v_d{}^r = Ri_d{}^r + \frac{d\Psi_d{}^r}{dt} - \omega_s \Psi_q{}^r = Ri_d{}^r + (d/dt)L_d i_d{}^r - P\omega_r L_q i_q{}^r \tag{2.15}$$

In these equations, all the stator voltages and currents are in rotor reference frame. The total average electromechanical energy coming from the source which is the developed power per phase is given by,

$$P_{phase} = \frac{1}{2} P\omega_r[\Psi i_q{}^r + (L_d - L_q) i_d{}^r i_q{}^r] \tag{2.16}$$

Therefore, total power developed by the machine is given by,

$$P_{mechanical} = \frac{3}{2} P\omega_r[\Psi i_q{}^r + (L_d - L_q) i_d{}^r i_q{}^r] \tag{2.17}$$

So, developed torque is given by,

$$T_e = \frac{P_{mechanical}}{\omega_r} = \frac{3}{2} P[\Psi i_q{}^r + (L_d - L_q) i_d{}^r i_q{}^r] \tag{2.18}$$

The d-q axis equivalent circuit diagram can be drawn as shown in Fig. 2.2

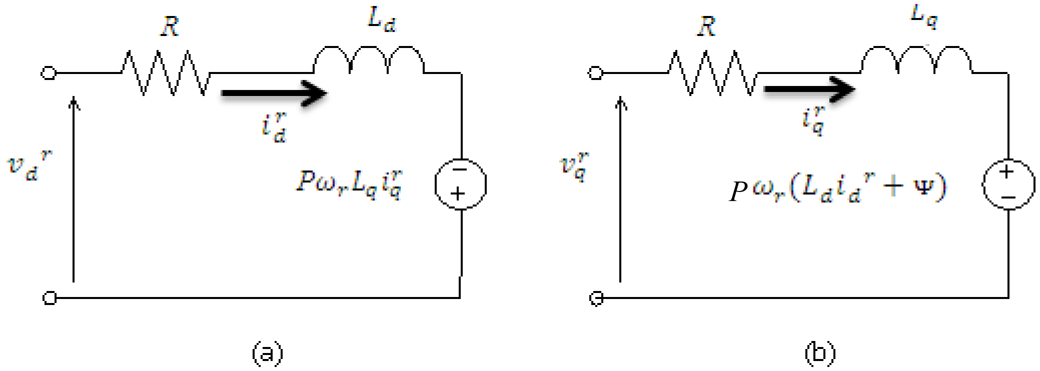

Fig. 2.2: Equivalent circuit model of IPMSM: a) d-axis b) q-axis.

The motor dynamics can be represented by the following equation,

$$T_e = T_L + B_m\omega_r + J\dot{\omega}_r \tag{2.19}$$

where: T_L = load torque in Nm

B_m = friction damping coefficient in Nm/rad/sec and J = inertia constant in kg-m^2

2.3 Vector Control of IPMSM

The vector control (VC) technique is an effective technique for control of AC motors in high performance drive applications (HPD). For VC operation of IPMSM drive, the machine equations are transformed from the stationary a-b-c frame to the synchronously rotating d-q frame where sinusoidal voltage becomes constant like a DC voltage. In case of DC motor, the developed torque equation is given by,

$$T_e = K I_a I_f \tag{2.20}$$

where: I_a= armature current

I_f = field current and K =constant

Both $I_a$and I_f are orthogonal and decoupled vectors. So, the control becomes easier for separately excited DC motor. In case of PM motor, the first term of torque equation (2.18) represents the magnet torque produced by the permanent magnet flux and q axis current and the second term represents the reluctance torque produced by the interaction of d and q axis inductances and the d-q axis currents. Most of the researchers consider the command d axis current, ${i_d}^r$=0 which makes the torque equation linear with i_q and control task becomes easier. Therefore, torque equation becomes,

$$T_e = \frac{3}{2} P \Psi {i_q}^r \tag{2.21}$$

However, with this assumption, the flux cannot be controlled in an IPMSM as per equation (2.13). Without a proper flux control, motor cannot be operated above the rated speed while maintaining voltage and current within the rated capacity of the motor/inverter. Thus, the IPMSM can be controlled like a separately excited DC motor where i_q controls torque and i_d controls flux. Using the phasor notation and taking the d^r axis as the reference phasor, the steady state voltage V_a can be derived from steady state d^r-q^r axis using the equation (2.13) and (2.14) as,

$$V_a = v_d^r + jv_q^r$$

$$=Ri_d{}^r + (d/dt)L_d i_d{}^r - P\omega_r L_q i_q{}^r + j(Ri_q{}^r + (d/dt)L_q i_q{}^r + P\omega_r L_d i_d{}^r + P\omega_r \Psi)$$

$$= Ri_d{}^r + jRi_q{}^r - P\omega_r L_q i_q{}^r + jP\omega_r L_d i_d{}^r + jP\omega_r \Psi \qquad (2.22)$$

At steady state condition, $(d/dt)\, jL_q i_q{}^r$=0.

In the case of IPMSM motor, the d^r axis current is negative and it demagnetizes the main flux provided by the permanent magnets. It can be seen from phasor diagram shown in Fig. 2.3.

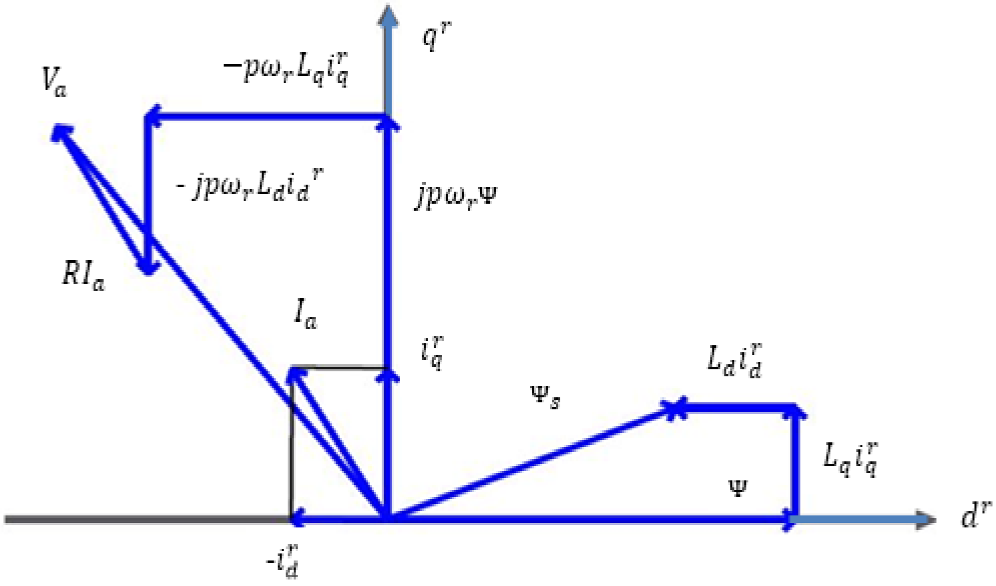

Fig. 2.3: Vector diagram of IPMSM.

With the $i_d{}^r$=0, the corresponding phasor diagram is shown in Fig. 2.4. The stator current vector can be controlled by controlling the individual d-q axis current.

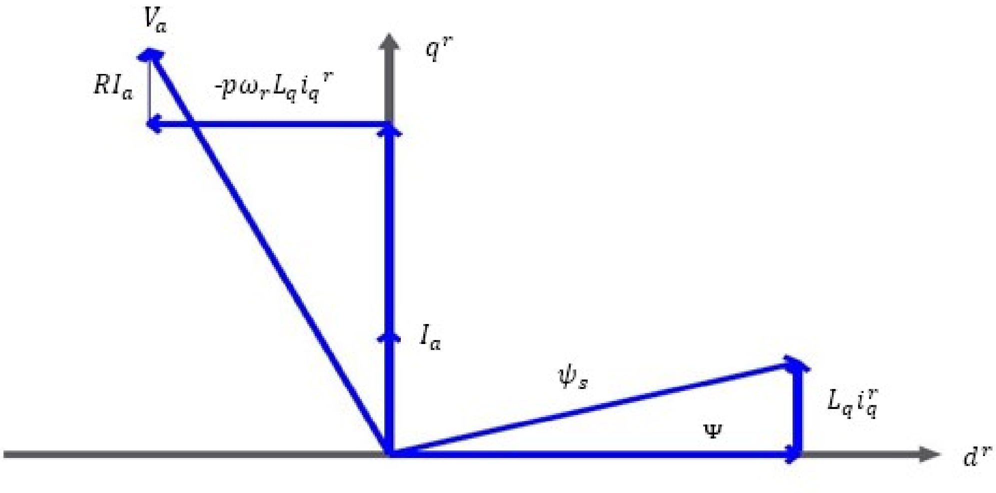

Fig. 2.4: Vector diagram of IPMSM with $i_d{}^r$=0.

2.4 Direct Torque and Flux Control (DTFC) of IPMSM

Direct torque and flux control (DTFC) is similar to vector control (VC) using variable frequency drive to control the AC motor output torque. In DTFC scheme, motor stator magnetic flux linkage vector and output torque is used as the control variable whereas three phase currents are used as control variable in VC. The DTFC scheme has the following advantages over its competitive field oriented control (FOC) scheme,

- For DTFC scheme, there is no need of pulse width modulation (PWM) signal whereas FOC needs PWM signal.
- DTFC is simpler and faster as compared to the FOC as it uses torque and flux as control parameters that directly relate to the motor itself.
- DTFC does not need any coordinate transformation which is necessary for FOC scheme.
- By optimizing the motor flux, DTFC scheme improves system efficiency with variable load/speed.

Despite several advantages of the DTFC scheme, it has some limitations which are as follows:

- DTFC controls the motor torque and flux directly which increases the ripple in these control parameters which results in motor vibration.
- The scheme is motor parameter dependent.
- DTFC scheme suffers from the start up problem as motor flux estimation involves the integration operation.

2.5 Analysis of DTFC Scheme

2.5.1 Conventional DTFC Scheme

The conventional stator flux linkage based DTFC scheme is shown in Fig. 2.5 where the motor actual torque and air-gap flux linkage values are compared with their corresponding reference values. The torque and flux hysteresis comparators take the corresponding error signals and generate the logic signals of the voltage vector lookup table.

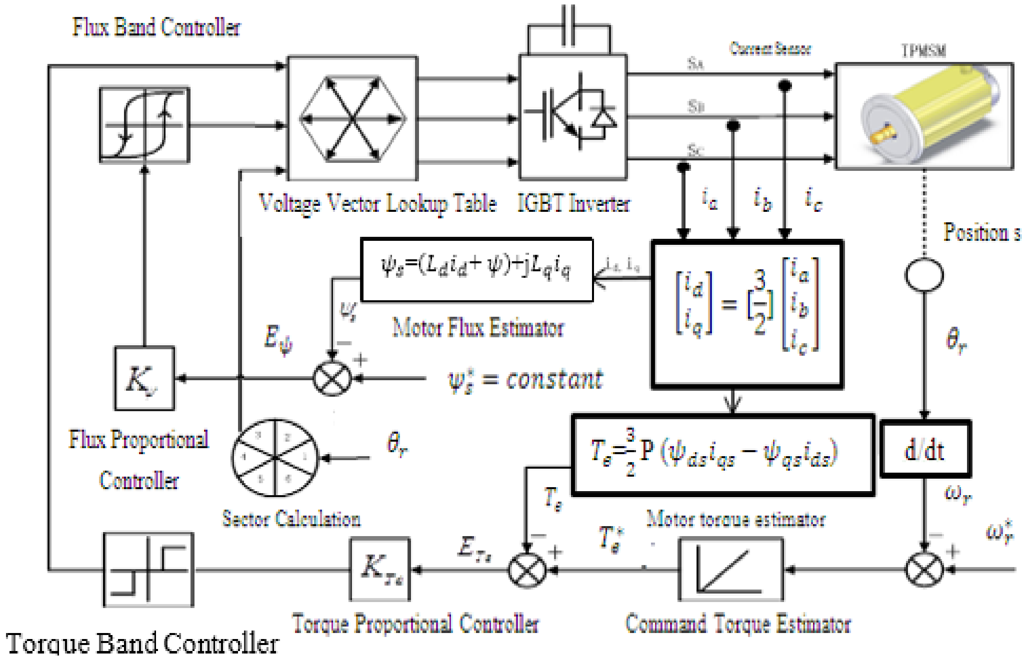

Fig. 2.5: Conventional DTFC scheme.

2.5.2 DTFC Control Principle

In DTFC stator flux linkage may be estimated as,

$$\psi_{s\alpha} = \int_0^t (V_{s\alpha} - R_s I_{s\alpha})\, dt + \psi_{s0} \qquad (2.23)$$

$$\psi_{s\beta} = \int_0^t (V_{s\beta} - R_s I_{s\beta})\, dt + \psi_{s0} \qquad (2.24)$$

where, $\psi_{s\alpha}$ and $\psi_{s\beta}$are the real and imaginary component of stator flux linkage.

This estimation of flux involves integration which needs initial condition ψ_{s0} during start-up operation. The modulus of stator flux linkage and its position is given by,

$$|\psi_s|=\sqrt{(\psi_{s\alpha}^2 + \psi_{s\beta}^2)} \qquad (2.25)$$

And, the position of stator flux linkage is determined as,

$$\theta=\tan^{-1}\left(\frac{\psi_{s\beta}}{\psi_{s\alpha}}\right) \qquad (2.26)$$

Using this angle, the sector number (1 to 6) is determined. Conventional DTFC scheme divides the stator flux into six sectors which is spaced by 60 degree is shown in Fig. 2.6. Neglecting the stator ohomic drop the flux linkage can be simplified as;

$$\vartriangle \psi_s = V_s \vartriangle t \qquad (2.27)$$

The change of the stator flux $\vartriangle \psi_s$ is caused by the application of new stator voltage vector. Equation (2.27) shows that the change in the stator flux is dependent on stator input voltage vector and the duration $\vartriangle t$ for which the voltage vector is applied. So, the trajectory of the flux linkage moves in the direction of the applied voltage vector of VSI with the speed proportional to the applied voltage. If one of the zero voltage vectors V_0 or V_7 is applied the locus of the flux linkage vector almost stands still. The stator flux linkage voltage vectors, inverter voltage vectors including the flux linkage components are shown in Fig. 2.6.

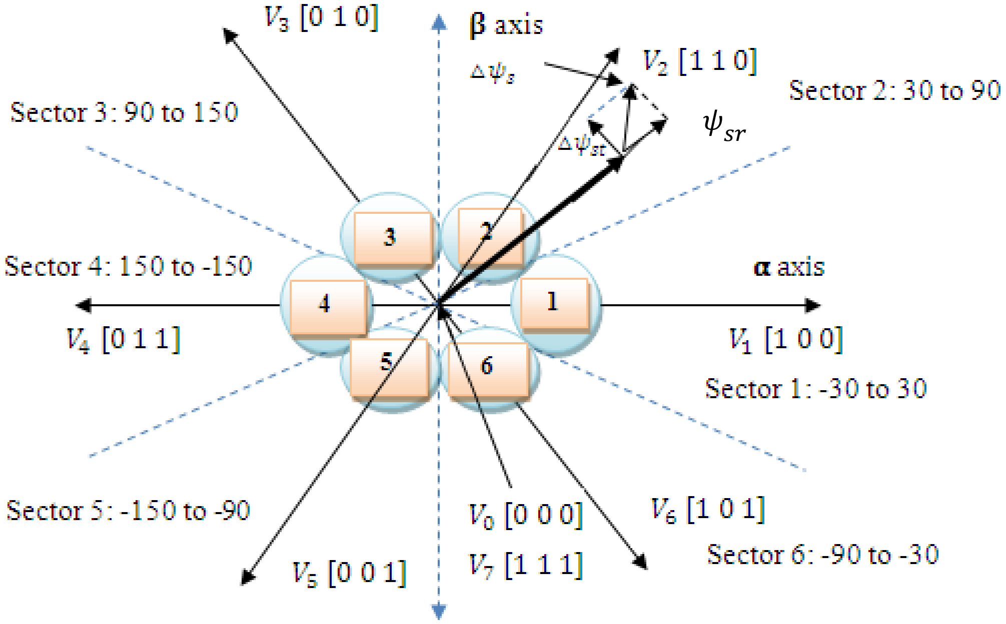

Fig. 2.6: Stator flux linkage sectors and inverter voltage vectors including the stator flux linkage.

Figure 2.6 shows that, stator flux ψ_s has the radial and tangential components ψ_{sr} and ψ_{st} respectively. In order to increase ψ_s, a voltage vector is selected which produces a higher radial components of ψ_{sr}. In steady state, $|\Delta\psi_r|$ and $|\Delta\psi_s|$ are almost constant and T_e depends on the torque angle θ_{sr}. To increase the torque, the stator voltage vector is applied in such a way that torque angle increases which is the angle between the stator and rotor flux linkages. From Fig 2.7 it can be observed that, forward switching of V_s causes rapid movement of ψ_s from ψ_r and thereby increasing θ_{sr} and T_e.

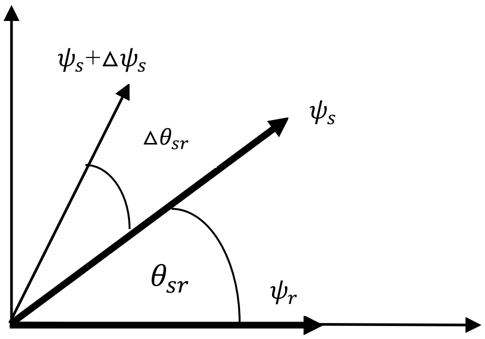

Fig. 2.7: Rotor and stator flux linkage vector.

For example, if the flux linkage vector is in sector 1, forward voltage vectors either V_2 or V_3 is selected to increase the torque. If the torque is in tolerance borders, then the flux vector must keep its position, angle does not change and zero voltage vectors are selected for it. If the actual torque is too large, then flux vector must go backward, and angle θ_{sr} decreases therefore backward voltage vectors must be selected. For example, if the flux linkage vector is in sector 1, then backward voltage vectors either V_6 or V_5 is selected. To control the torque ripple, the duration of application of any stator voltage vector plays an important role.

2.5.3 Flux and Torque Comparator

For flux hysteresis comparator, motor air-gap flux (ψ_s) is compared with the reference air gap flux (ψ_s^*). The error between ψ_s and ψ_s^* is defined as;

$$e_\psi = \psi_s^* - \psi_s \tag{2.28}$$

The flux comparator logic is given below and flux hysteresis band is shown in Fig. 2.8.

if, $e_\psi \geq +HB_\psi$ then $H_\psi = +1$

if, $e_\psi \leq -HB_\psi$ then $H_\psi = -1$

if, $-HB_\psi < e_\psi < +HB_\psi$ then $H_\psi = 0$

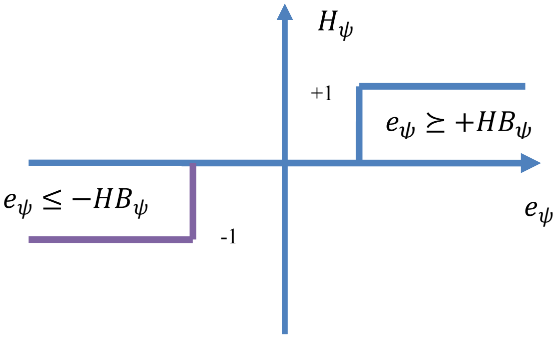

Fig. 2.8: Flux hysteresis band.

For torque hysteresis comparator, motor output torque (T_e) is compared with the reference torque (T_e^*). The error between T_e and T_e^* is defined as;

$$e_T = T_e^* - T_e \tag{2.29}$$

The torque comparator logic is given below and torque hysteresis band is shown in Fig. 2.9.

if, $e_T \geq +HB_T$ then $H_T = +1$

if, $e_T \leq -HB_T$ then $H_T = -1$

if, $-HB_T < e_T < +HB_T$ then $H_T = 0$

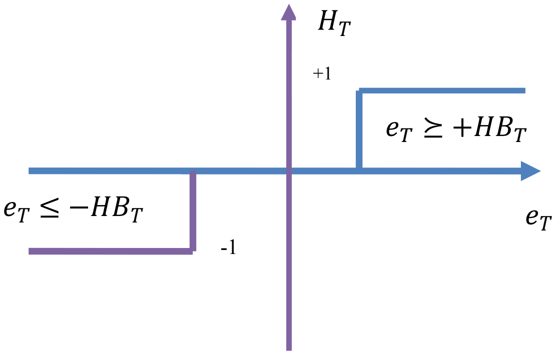

Fig. 2.9: Torque hysteresis band.

2.5.4 Three Phase IGBT Inverter

The voltage source inverter (VSI) is widely used in HPD applications to control the rotating field machines. In large number of industries the PMSM's are required to be operated at different speeds or torques. In order to meet the variable speed or torque demand, these motors are fed from the inverters with variable voltage and variable frequency supply. The VSI with 3-phase winding can generate voltage vectors. The voltage vectors are defined by the combinations of switch positions (S_A , S_B , S_C). S_A= 1 implies T_1 on and S_A= 0 implies T_2 on. For two-level VSI there are 8 possible combinations of power switches which can produce six active voltage vectors and two zero voltage vectors. Typical structure of two-level VSI drive is shown in Fig. 2.10. In Fig. 2.10, T_1, T_3, T_5 indicate the high side and T_2, T_4 , T_6 indicate the low side of the inverter.

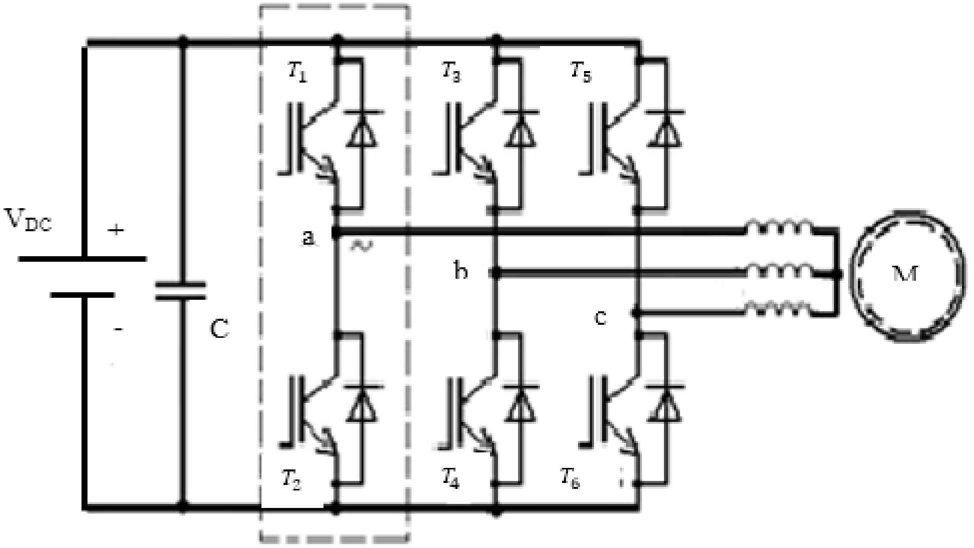

Fig. 2.10: Two-level VSI drive.

Voltage vectors of a two-level VSI in a stationary XY reference frame are shown in Fig. 2.11. Voltage polarities at the three-phase terminals of the inverter are marked near the vectors where '+' means upper switch of corresponding phase in ON and '-' means lower switch of corresponding phase is ON.

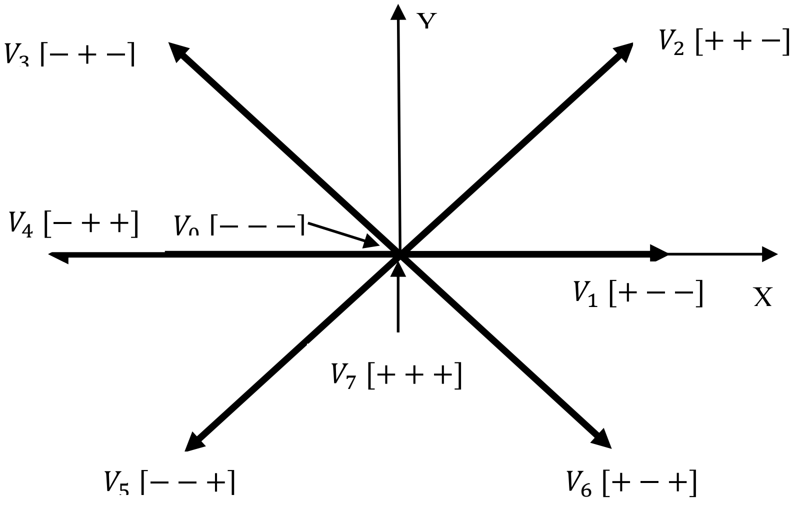

Fig. 2.11: Two-level VSI voltage vectors.

2.5.5 DTFC Switching Table

The output signal of the torque hysteresis comparator possesses three different values: +1, -1, and 0. $H_T = +1$ corresponds actual value of the torque is below the reference torque and torque must be increased; at $H_T = -1$ torque must be decreased; $H_T = 0$ means that torque is in the hysteresis limits. The output signal of the flux hysteresis comparators has two values 1 and -1. If the current magnitudes of the stator flux linkage are significantly less than the reference value, then flux linkage magnitude should be increased which corresponds to $H_\psi = +1$. But, if the magnitude of the flux linkage is above the reference value, then flux linkage magnitude must be decreased which corresponds $H_\psi = -1$. Signals from the torque and flux hysteresis comparators as well as position information (sector number) about the flux linkage vector are the elements of switching table of DTFC. The control of the switches is adjusted only when the torque or flux linkage differs from the reference value. When hysteresis limit is reached next voltage vector is selected from the switching table of DTFC so that actual flux linkage (ψ_s) tracks the reference flux linkage (ψ_s^*). The DTFC switching table is shown in Table 2.1.

Table 2.1: DTFC look-up table for inverter

H_ψ	H_T	S_1	S_2	S_3	S_4	S_5	S_6
+1	+1	V_2	V_3	V_4	V_5	V_6	V_1
	0	V_0	V_7	V_0	V_7	V_0	V_7
	-1	V_6	V_1	V_2	V_3	V_4	V_5
-1	+1	V_3	V_4	V_5	V_6	V_1	V_2
	0	V_7	V_0	V_7	V_0	V_7	V_0
	-1	V_5	V_6	V_1	V_2	V_3	V_4

For example, at sector 1 (-30~+30), if the flux is too high (H_ψ= +1) and the torque is too high (H_T= +1), the voltage vector V_2 is applied to the IGBT inverter. The voltage vector follows the zigzag path within the flux hysteresis band ($2|\Delta\psi_s|$). Thus, actual flux follows the reference flux. The selection of voltage vector is made so as to restrict the flux and torque errors within the hysteresis bands and to obtain the fastest torque response to reduce the torque ripple contents.

The selected voltage vectors will make the air gap flux to follow the reference flux where the ψ_s^* and $\psi_s$will follow the following relation;

$$-|\Delta\psi_s| \leq (\psi_s^* - \psi_s) \leq +|\Delta\psi_s| \tag{2.30}$$

The voltage vector plane is divided into six sectors so that each voltage vector divides each region into two equal parts as shown in Fig. 2.12. In each sector four of the six non-zero voltage vectors along with zero vectors may be used. For example, for sector 1, V_2, V_3, V_5 and V_6 voltage vectors are used either to increase or decrease the torque depending upon the condition of flux hysteresis comparators output.

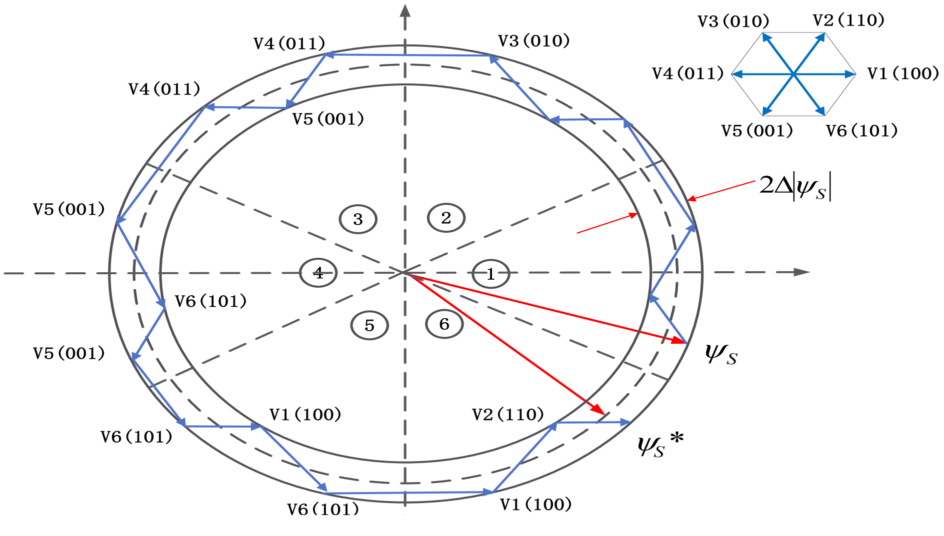

Fig. 2.12: Motor air-gap flux zigzag path.

2.6 Conclusion

This Chapter details the mathematical model development of IPMSM drive and operating principle of conventional DTFC scheme. There are several limitations of the conventional DTFC scheme. Firstly, due to the dependency of the air gap flux linkages on motor operating conditions, it is essential to estimate the motor air-gap flux linkage which is assumed constant for conventional system. Secondly, unbalance voltage effects in one sector can result in error flux which increases torque ripples, therefore to avoid the unbalance voltage effects sector numbers must be modified to get better dynamic performance of the drive system. Realistically, current sector number calculation of stator flux linkage vector involves trigonometric function (tangent), which is a time consuming calculation, but can be replaced by logic decisions of digit by digit calculations.

The following Chapter details the proposed novel DTFC scheme to overcome the drawbacks of conventional DTFC scheme and hence to improve dynamic performance of IPMSM drive.

Chapter 3

Proposed Novel DTFC Scheme

3.1 Introduction

High performance motor drives require accurate speed response, quick recovery of speed from any disturbances with almost no steady state torque ripple. Most of the existing DTFC scheme either consider reference air-gap flux constant or utilize conventional six-sector based algorithm for easier implementation. However, dynamic performance is sacrificed with the conventional DTFC algorithm.

To meet high dynamic performance demand, the control algorithm proposed in this thesis incorporates adaptive flux observer based loss minimization algorithm (LMA) and conventional six-sector based algorithm has been modified into eighteen-sector based algorithm. Finally, three level torque hysteresis comparators are modified into five levels for eighteen-sector based DTFC scheme.

3.2 Loss Minimization Algorithm (LMA) based DTFC Scheme

Most of the reported work on DTFC considered reference air-gap flux (ψ_s^*) as constant, hence the efficiency cannot be optimized also DTFC of IPMSM drive suffers from large torque ripples. Therefore, a model based LMA is developed to obtain the optimum air-gap flux linkage, which acts as a command flux for the DTFC based IPMSM drive which is shown in Fig. 3.1. As the motor stator flux rotates in the air-gap, the DTFC scheme will select the right voltage vector from the look up table. The selected voltage vector will make the air-gap flux (ψ_s) to track the flux reference (ψ_s^*). In PMSM, the flux cannot be controlled directly as the main flux is supplied by the permanent magnets. In an IPMSM the d-axis armature reaction current i_d is utilized to control the flux. LMA is utilized to calculate the minimum value of i_d which reduces the power losses of the motor. The modified DTFC maintains higher efficiency and high dynamic performance.

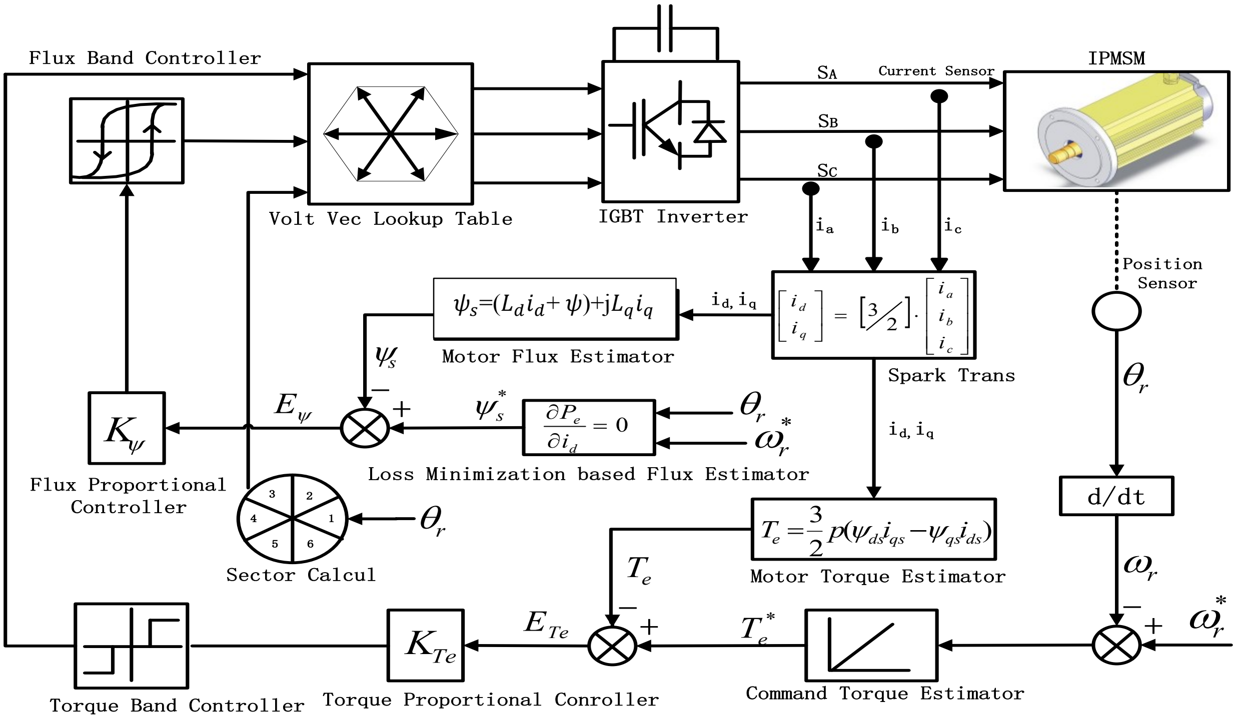

Fig. 3.1: LMA based conventional DTFC scheme for IPMSM drive.

3.3 Proposed Stator Flux Linkage Sector Number Determination Algorithm

The sector number determination in DTFC involves a trigonometric function. For real-time implementation, the microprocessor evaluates the trigonometric function by using time consuming complex calculations as compared to normal arithmetic relations. In an effort to simplify such systems, in this thesis a novel sector determination algorithm is developed, which just requires shifting and additions [37]. Thus, iteration becomes simpler and can be performed very rapidly. Fig. 3.2 shows the proposed novel sector determination algorithm of the conventional six-sector based DTFC scheme.

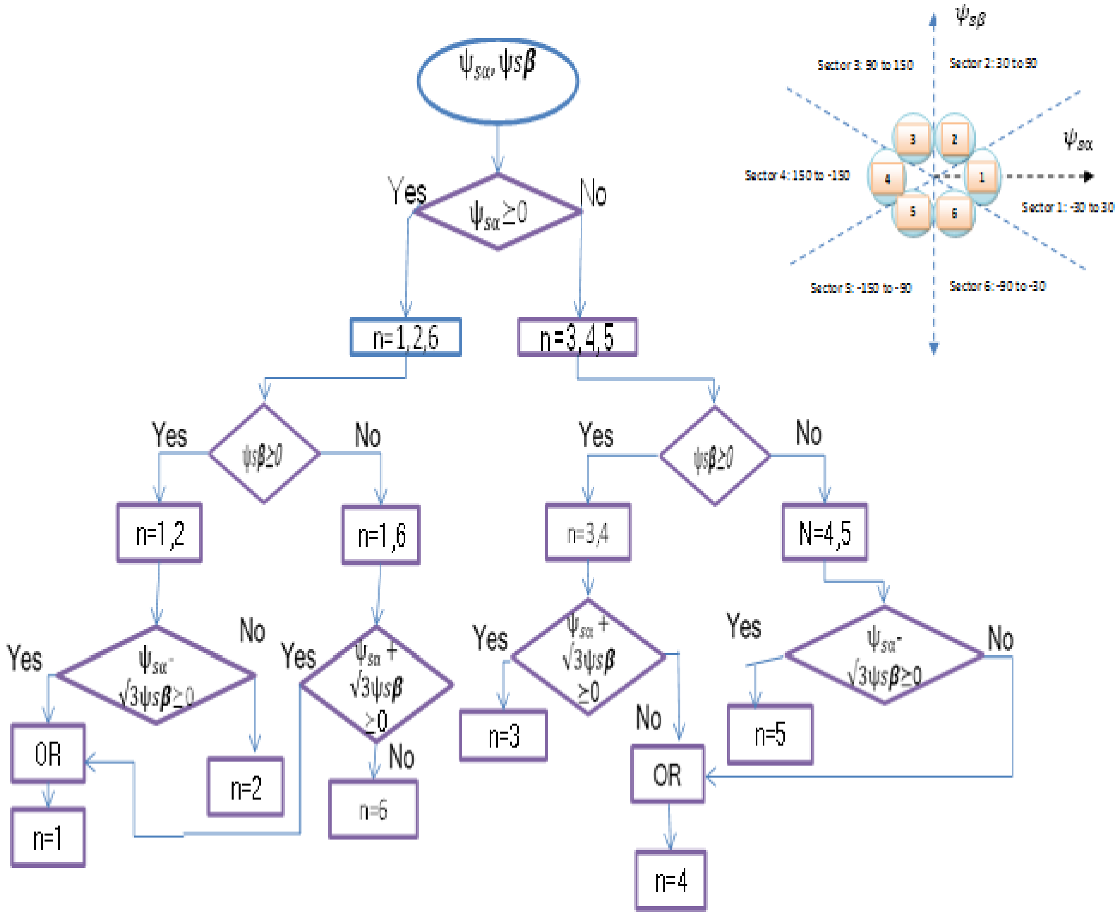

Fig. 3.2: Proposed flow chart for sector determination algorithm.

3.4 LMA Based Reference Flux Estimation

Several LMAs for PMSM drives have been reported in the literature [38-39]. The loss minimization can be done either by using search controller (SC) or loss model controller (LMC) algorithm. For SC based LMA, motor current or flux value is decremented in steps until the minimum input power point is detected for certain load and speed to achieve minimum loss condition. Although SC is simple and flexible but also it creates the torque ripples as control variables are decremented to find the minimum input power. Furthermore, SC is slow and needs to find minimum input power for each operating conditions. On the other hand, model based LMA calculates the motor stator current or air gap flux linkage based on loss model of the motor which reduces the power loss. This process is faster and does not have torque ripples like SC based LMA. Therefore, this thesis incorporates the model based LMA to estimate the reference air gap flux linkage to ensure high dynamic performance of the drive for different speed and load conditions. The model based LMA is used to calculate the optimum i_d^* which ensures the minimum power losses of the motor. The d-q axis model of IPMSM drives incorporating the iron loss is shown in Fig. 3.3.

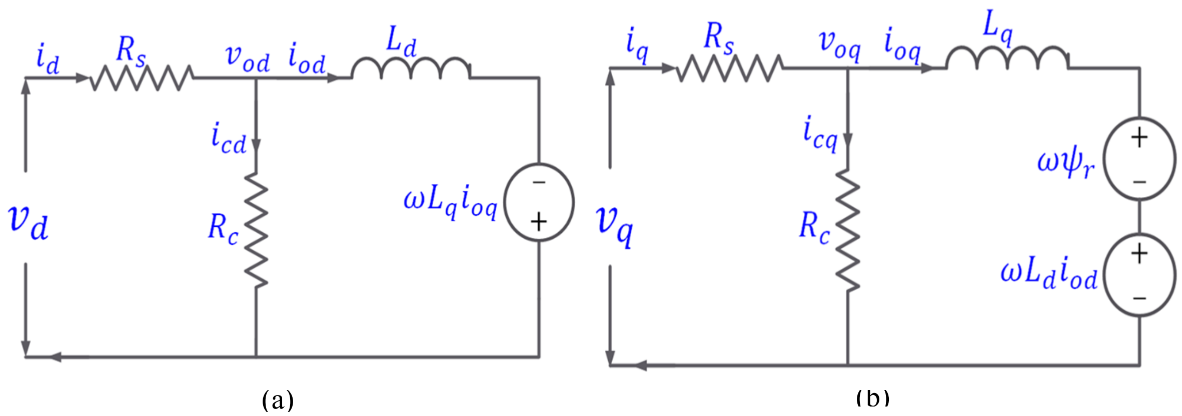

Fig. 3.3: IPMSM model incorporating iron loss; (a) d-axis model, (b) q axis model.

From the loss model of IPMSM, the d-axis voltage and current can be written as,

$$v_d = R_s i_d + v_{od} \tag{3.1}$$

$$i_d = i_{od} + i_{cd} \tag{3.2}$$

where:

i_{cd} = d-axis core loss current

i_{od} = magnetizing components of i_d

Substituting the d-axis current value in equation (3.1),

$$v_d = R_s(i_{od} + i_{cd}) + v_{od}$$

$$\Rightarrow v_d = R_s i_{od} + R_s i_{cd} + L_d \frac{di_{od}}{dt} - L_q i_{oq} \omega \tag{3.3}$$

From d-axis loss model of IPMSM, d-axis iron loss current can be written as,

$$i_{cd} = \frac{v_{od}}{R_c} = \frac{L_d \frac{di_{0d}}{dt} - L_q i_{oq}\omega}{R_c} \tag{3.4}$$

Substituting the values of d-axis iron loss current in equation (3.3),

$$v_d = R_s i_{od} + R_s \frac{v_{od}}{R_c} + L_d \frac{di_{od}}{dt} - L_q i_{oq}\omega$$

$$\Rightarrow \; v_d = R_s i_{od} + R_s \frac{L_d \frac{di_{od}}{dt} - L_q i_{oq}\omega}{R_c} + L_d \frac{di_{od}}{dt} - L_q i_{oq}\omega$$

$$\Rightarrow \; v_d = R_s i_{od} + \frac{R_s}{R_c}\left(L_d \frac{di_{od}}{dt} - L_q i_{oq}\omega\right) + L_d \frac{di_{od}}{dt} - L_q i_{oq}\omega$$

$$\Rightarrow v_d = R_s i_{od} + \left(\frac{R_s}{R_c} + 1\right) L_d \frac{di_{od}}{dt} - (\frac{R_s}{R_c} + 1) L_q i_{oq}\omega$$

$$\Rightarrow v_d = R_s i_{od} + \left(\frac{R_s}{R_c} + 1\right)\left(L_d \frac{di_{od}}{dt} - L_q i_{oq}\omega\right) \tag{3.5}$$

The q-axis voltage (v_q) and current (i_q) can be written as,

$$v_q = R_s i_q + v_{oq} \tag{3.6}$$

$$i_q = i_{oq} + i_{cq} \tag{3.7}$$

where:

i_{cq} = q-axis core loss current

i_{oq} = magnetizing components of i_q

Substituting the q-axis current value in equation (3.6),

$$v_q = R_s(i_{oq} + i_{cq}) + v_{oq} \tag{3.8}$$

From q-axis loss model of IPMSM drive,

$$v_{oq} = L_q \frac{di_{0q}}{dt} + L_d i_{od} \omega + \Psi_r \omega \tag{3.9}$$

$$i_{cq} = \frac{v_{oq}}{R_c} = \frac{L_q \frac{di_{0q}}{dt} + L_d i_{od} \omega + \Psi_r \omega}{R_c} \tag{3.10}$$

Substituting the values of v_{oq} and i_{cq} in equation (3.8),

$$v_q = R_s i_{oq} + R_s \frac{L_q \frac{di_{oq}}{dt} + L_d i_{od} \omega + \Psi_r \omega}{R_c} + L_q \frac{di_{0q}}{dt} + L_d i_{od} \omega + \Psi_r \omega$$

$$\Rightarrow v_q = \left(\frac{R_s}{R_c} + 1\right) \left[L_q \frac{di_{0q}}{dt} + \Psi_r \omega + L_d i_{od} \omega\right] + R_s i_{oq} \tag{3.11}$$

From d-q axis loss model of IPMSM, iron loss components i_{cd} and i_{cq} can be written as,

$$i_{cd} = i_d - i_{0d}$$
$$i_{cq} = i_q - i_{0q}$$

The d-axis iron loss current can be written from d-axis model (Fig. 3.3 (a)) where steady state condition is assumed. Therefore, $L_d \frac{di_{0d}}{dt}$=0.

$$i_{cd} = \frac{v_{od}}{R_c} = \frac{L_d \frac{di_{0d}}{dt} - L_q i_{oq} \omega}{R_c}$$

$$\Rightarrow i_{cd} = \frac{L_d \frac{di_{0d}}{dt} - L_q \omega (i_q - i_{cq})}{R_c}$$

$$\Rightarrow i_{cd} = \frac{-L_q \omega (i_q - i_{cq})}{R_c} \tag{3.12}$$

Considering steady-state condition, from the q-axis model (Fig. 3.3 (b)),

$$i_{cq} = \frac{v_{oq}}{R_c} = \frac{L_q \frac{di_{oq}}{dt} + L_d i_{od}\omega + \Psi_r\omega}{R_c} = \frac{L_q \frac{di_{oq}}{dt} + L_d\omega\ (i_d - i_{cd}) + \Psi_r\omega}{R_c}$$

$$= \frac{L_d\omega\ (i_d - i_{cd}) + \Psi_r\omega}{R_c} \tag{3.13}$$

Total electric power loss can be written as,

$$P_E = \frac{3}{2}\left(R_s {i_d}^2 + R_s {i_q}^2 + R_c {i_{cd}}^2 + R_c {i_{cq}}^2\right) \tag{3.14}$$

To get the minimum power loss condition differentiate the total electric power with respect to i_d.

$$\frac{dP_E}{di_d} = \frac{3}{2}[2R_s i_d + 2R_s i_q \frac{di_q}{di_d} + 2R_c i_{cd} \frac{di_{cd}}{di_d} + 2R_c i_{cq} \frac{di_{cq}}{di_d}]$$

$$\Rightarrow \frac{dP_E}{di_d} = 3\left[R_s i_d + R_s i_q \frac{di_q}{di_d} + R_c i_{cd} \frac{di_{cd}}{di_d} + R_c i_{cq} \frac{di_{cq}}{di_d}\right] \tag{3.15}$$

Higher efficiency is achieved when the total power losses are minimum and minimum power loss condition is obtained by differentiating the total power loss with respect to i_d and then setting it to zero to get optimum i_d. For the minimum power loss condition,

$$\frac{dP_E}{di_d} = 0$$

$$\Rightarrow \left[R_s i_d + R_s i_q \frac{di_q}{di_d} + R_c i_{cd} \frac{di_{cd}}{di_d} + R_c i_{cq} \frac{di_{cq}}{di_d}\right] = 0$$

$$\Rightarrow R_s i_d = -[R_s i_q \frac{di_q}{di_d} + R_c i_{cd} \frac{di_{cd}}{di_d} + R_c i_{cq} \frac{di_{cq}}{di_d}]$$

$$\Rightarrow i_d = \frac{-[R_s i_q \frac{di_q}{di_d} + R_c i_{cd} \frac{di_{cd}}{di_d} + R_c i_{cq} \frac{di_{cq}}{di_d}]}{R_s} \tag{3.16}$$

d-axis core loss current i_{cd} can be calculated from equation (3.12),

$$i_{cd} = \frac{-L_q\omega\left(i_q - i_{cq}\right)}{R_c}$$

$$\Rightarrow i_{cd} = -\frac{L_q\omega i_q}{R_c} + \frac{L_q\omega i_{cq}}{R_c}$$

$$\Rightarrow \; i_{cd} = -\frac{L_q\omega i_q}{R_c} + \frac{L_q\omega}{R_c}[\frac{L_d\omega\,(i_d - i_{cd}) + \Psi_r\omega}{R_c}]$$

$$\Rightarrow \; i_{cd} = -\frac{L_q\omega i_q}{R_c} + \frac{L_q\Psi_r\omega^2 + L_dL_q\omega^2(i_d - i_{cd})}{R_cR_c}$$

$$\Rightarrow {R_c}^2 i_{cd} = -L_q\omega i_q R_c + L_q\Psi_r\omega^2 + L_dL_q\omega^2(i_d - i_{cd})$$

$$\Rightarrow {R_c}^2 i_{cd} + L_dL_q i_{cd}\omega^2 = -L_q\omega i_q R_c + L_q\Psi_r\omega^2 + L_dL_q i_d\omega^2$$

$$\Rightarrow i_{cd} = \frac{-L_q i_q\omega R_c + L_q\Psi_r\omega^2 + L_dL_q\omega^2 i_d}{{R_c}^2 + L_dL_q\omega^2} \qquad (3.17)$$

The steady state value of core loss current component i_{cq} can be calculated from equation (3.13),

$$i_{cq} = \frac{L_d\omega\,(i_d - i_{cd}) + \Psi_r\omega}{R_c}$$

$$\Rightarrow i_{cq} = \frac{\Psi_r\omega}{R_c} + \frac{L_d\omega\, i_d}{R_c} - \frac{L_d\omega i_{cd}}{R_c}$$

$$\Rightarrow i_{cq} = \frac{\Psi_r\omega}{R_c} + \frac{L_d\omega\, i_d}{R_c} - \frac{L_d\omega}{R_c}[\frac{-L_q\omega(i_q - i_{cq})}{R_c}]$$

$$\Rightarrow i_{cq} = \frac{\Psi_r\omega}{R_c} + \frac{L_d\omega i_d}{R_c} + \frac{L_dL_q i_q\omega^2}{{R_c}^2} - \frac{L_dL_q i_{cq}\omega^2}{{R_c}^2}]$$

$$\Rightarrow {R_c}^2 i_{cq} = \Psi_r\omega R_c + L_d\omega i_d R_c + L_dL_q i_q\omega^2 - L_dL_q i_{cq}\omega^2$$

$$\Rightarrow {R_c}^2 i_{cq} + L_dL_q i_{cq}\omega^2 = \Psi_r\omega R_c + L_d\omega i_d R_c + L_dL_q i_q\omega^2$$

$$\Rightarrow [{R_c}^2 + L_dL_q\omega^2] i_{cq} = \Psi_r\omega R_c + L_d\omega i_d R_c + L_dL_q i_q\omega^2$$

$$\Rightarrow i_{cq} = \frac{\Psi_r\omega R_c + L_d\omega\, i_d R_c + L_dL_q i_q\omega^2}{{R_c}^2 + L_dL_q\omega^2} \qquad (3.18)$$

Differentiating d-axis core loss current i_{cd} with respect to i_d,

$$\frac{di_{cd}}{di_d} = \frac{-L_q \omega R_c \frac{di_q}{di_d} + L_q \Psi_r \frac{d}{di_d}(\omega^2) + L_d L_q \omega^2 \frac{di_d}{di_d}}{{R_c}^2 + L_d L_q \omega^2}$$

$$\Rightarrow \frac{di_{cd}}{di_d} = \frac{L_d L_q \omega^2}{{R_c}^2 + L_d L_q \omega^2} \tag{3.19}$$

Differentiating q-axis core loss current $i_{cq}$with respect to i_d,

$$\frac{di_{cq}}{di_d} = \frac{\frac{d}{di_d}(\Psi_r \omega R_c) + L_d \omega R_c \frac{di_d}{di_d} + L_d L_q \omega^2 \frac{di_q}{di_d}}{{R_c}^2 + L_d L_q \omega^2}$$

$$\Rightarrow \frac{di_{cq}}{di_d} = \frac{L_d \omega R_c}{{R_c}^2 + L_d L_q \omega^2} \tag{3.20}$$

To get the minimum d-axis current, from equation (3.16),

$$i_d = \frac{-[R_s i_q \frac{di_q}{di_d} + R_c i_{cd} \frac{di_{cd}}{di_d} + R_c i_{cq} \frac{di_{cq}}{di_d}]}{R_s}$$

$$\Rightarrow\ i_d = -\frac{0 + [R_c i_{cd} \frac{L_d L_q \omega^2}{{R_c}^2 + L_d L_q \omega^2}] + R_c i_{cq} [\frac{L_d \omega R_c}{{R_c}^2 + L_d L_q \omega^2}]}{R_s}$$

$$\Rightarrow\ i_d = -\frac{R_c i_{cd} L_d L_q \omega^2 + R_c i_{cq} L_d \omega R_c}{R_s({R_c}^2 + L_d L_q \omega^2)}$$

$$\Rightarrow\ i_d = -\frac{R_c L_d \omega [i_{cd} L_q \omega + i_{cq} \omega]}{R_s({R_c}^2 + L_d L_q \omega^2)}$$

$$\Rightarrow\ i_d = {i_d}^* \tag{3.21}$$

Using equation (3.13) and (3.21),

$$i_{cq} = \frac{L_d\omega\,(i_d - i_{cd}) + \Psi_r\omega}{R_c}$$

$$\Rightarrow i_q - i_{0q} = \frac{L_d\omega i_{od} + \Psi_r\omega}{R_c}$$

$$\Rightarrow i_q = \frac{L_d\omega\, i_{0d} + \Psi_r\omega}{R_c} + i_{0q}$$

$$\Rightarrow\ i_q = {i_q}^* \tag{3.22}$$

For DTFC, reference flux is estimated from the reference d-q axis current as,

$$\mathit{\Psi_s}^* = \psi_d^* + j\psi_q^* = (\mathit{\Psi}_r + L_d i_d^*) + jL_q i_q^* \tag{3.23}$$

Total Power developed by the motor;

$$P_{out} = T_L\omega$$

$$P_{total} = P_{out} + P_E + P_{mechanical}$$

$$P_{mechanical} = \text{Mechanical frictional constant} * \omega$$

Motor efficiency is given by, $\eta = \frac{P_{out}}{P_{total}} * 100\%$

3.5 Loss of Voltage Source Inverter (VSI)

The harmonic losses of the motor and the steady-state torque ripple can be minimized by increasing the inverter switching frequency. But, the increase in the switching frequency increases the inverter switching losses. That’s why in this thesis inverter losses are also investigated in simulation. The aim of this section is to provide the analytical model for the calculation of power losses in IGBT based VSI inverter for IPMSM drive. The inverter parameters of the semiconductor switches in the inverter have been extracted from the data sheets of SEMIKRON, SKHI 22 AR [40]. The losses in a power-switching device consist of conduction losses, switching losses and off-state blocking loss.

3.5.1 Switching Losses of VSI

During the commutations, losses appear due to the switching pattern. Switching losses are due to the energy dissipated during the commutations ON and OFF in the semiconductor (IGBT) and in the power diode due to reverse recovery current in the off state. The equation for the switching losses is given by [40],

$$P_{switching} = \frac{\sqrt{2}}{\pi}.f_{sw}\left(E_{on,I} + E_{off,I} + E_{off,D}\right).\frac{V_{dc}}{V_r}.\frac{I_L}{I_r} \quad (3.25)$$

where:

f_{sw}= VSI switching frequency

V_{dc}= dc link voltage

I_L= peak value of ac line current that is assumed sinusoidal

$E_{on,I}$= turn-on energies of IGBT

$E_{off,I}$= turn-off energy of IGBT

$E_{off,D}$= turn-off energy of the power diode due to reverse recovery current

3.5.2 Conduction Losses of VSI

In contrast to the switching losses, the conduction losses are directly depending on the modulation function. Conduction losses are due to the losses in the IGBT and diode, which can be expressed as [40],

$$P_{conduction(IGBT)} = \frac{1}{2}\left(V_{ceo}.\frac{I_L}{\pi} + r_{tran}\frac{I_L^2}{\pi}\right) + m.cos\varphi\left(V_{ceo}.\frac{I_L}{8} + r_{tran}\frac{I_L^2}{3\pi}\right) \quad (3.26)$$

$$P_{conduction(Diode)} = \frac{1}{2}\left(V_{Fo}.\frac{I_L}{\pi} + r_{diode}\frac{I_L^2}{\pi}\right) - m.cos\varphi\left(V_{Fo}.\frac{I_L}{8} + r_{diode}\frac{I_L^2}{3\pi}\right) \quad (3.27)$$

where:

m = modulation index

φ= angle between the fundamental of modulation function and load current

r_{tran}= transistor resistance

r_{diode}= diode resistance

V_{ceo}= transistor saturation voltage

V_{Fo}= diode threshold voltage

However, increasing the motor speed requires higher line to line voltage and causes the motor to draw higher current for constant load torque. Therefore, inverter losses are increased.

3.6 Proposed Eighteen-Sector Based DTFC

The problems of conventional DTFC scheme has been alluded earlier. In conventional DTFC scheme motor reference air-gap flux linkage is considered constant therefore, motor efficiency cannot be optimized and it cannot be operated above the rated speed. Therefore, this thesis incorporates LMA to estimate the motor air gap flux to optimize the motor efficiency. On the other hand, six-sector based DTFC suffers from torque ripples. That's why conventional six-sector based algorithm is modified into eighteen-sector based algorithm to improve the dynamic performance of the DTFC in which maintaining higher efficiency through LMA. Fig. 3.4 shows the proposed modified eighteen-sector based DTFC scheme incorporating LMA for reference flux estimation.

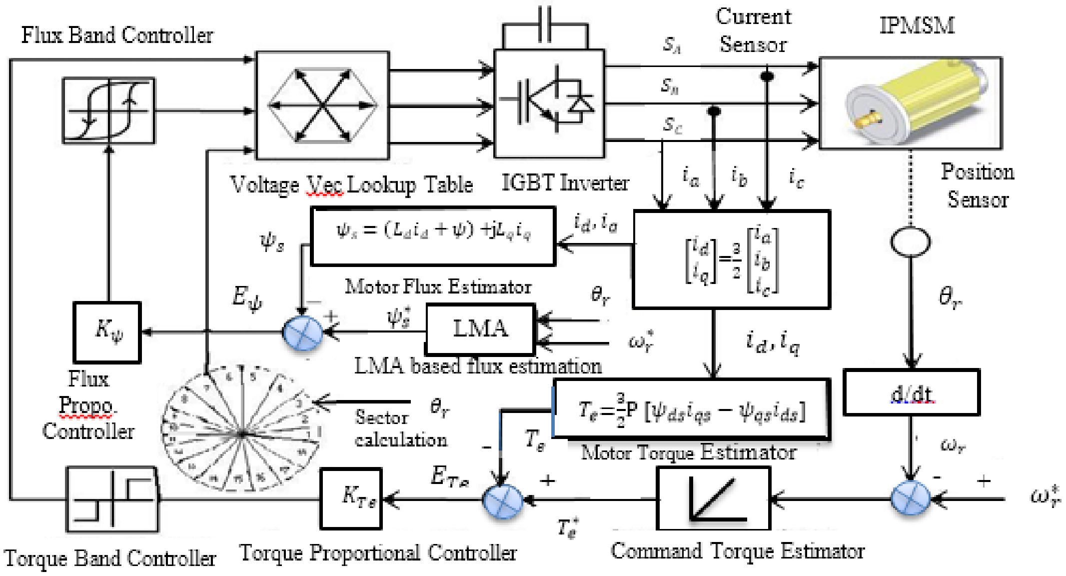

Fig. 3.4: Modified eighteen-sector based proposed DTFC scheme.

3.6.1 Improvements of Eighteen-Sector

The traditional DTFC divides the stator flux vector into six-sector. In one sector, the unbalanced effect of stator voltage can cause the unbalanced change of flux track. The flux track will not be round. The distortion of flux exerts bad influences on the system performance and it also causes distortion of the current. In order to improve the situation, the method of subdividing stator flux angles is proposed in this work. According to the position of stator flux, the spaces are dived into 18 sectors such as $(-10^{\circ}, 10^{\circ})$, $(10^{\circ}, 30^{\circ})$………$(-50^{\circ}, -30^{\circ})$ and $(-30^{\circ}, -10^{\circ})$. Fig. 3.5 shows the eighteen-sector and choices of the vectors are shown in Table.3.1. For torque hysteresis controller, H_T = 1 means reference torque is less than the estimated one and a voltage vector should be selected in a way to increase the torque. H_T =-1 means the reference torque is higher than the estimated one and voltage vector should be selected in a way to decrease the torque. This is exactly same control to the amplitude of stator flux. For example, if the stator flux is in sector 1, to decrease flux (H_ψ=-1) and to increase the torque (H_T=+1), voltage vector is applied two steps ahead of the current sector voltage vector. Thus the voltage vector V_3 is applied. When H_T =-1 and H_ψ=-1 and flux linkage space vector is in sector 1 then voltage vector is applied that is 2 steps backward of the current sector number. That’s why voltage vector V_5 is applied, which is shown in Table-3.1.

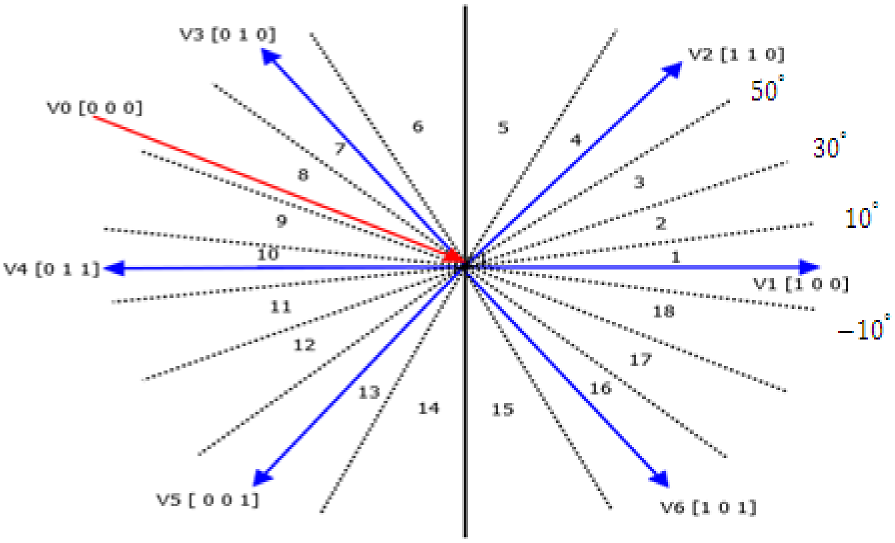

Fig. 3.5: Division of eighteen-sector.

Table 3.1: DTFC look-up table with three level torque hysteresis comparator inverter switching

H_ψ	H_T	S_1	S_2	S_3	S_4	S_5	S_6	S_7	S_8	S_9	S_{10}	S_{11}	S_{12}	S_{13}	S_{14}	S_{15}	S_{16}	S_{17}	S_{18}
+1	+1	V_2	V_2	V_3	V_3	V_3	V_4	V_4	V_4	V_5	V_5	V_5	V_6	V_6	V_6	V_1	V_1	V_1	V_2
	0	V_0	V_0	V_0	V_7	V_7	V_7	V_0	V_0	V_0	V_7	V_7	V_7	V_0	V_0	V_0	V_7	V_7	V_7
	-1	V_6	V_1	V_1	V_1	V_2	V_2	V_2	V_3	V_3	V_3	V_4	V_4	V_5	V_5	V_5	V_5	V_6	V_6
-1	+1	V_3	V_3	V_3	V_4	V_4	V_4	V_5	V_5	V_5	V_6	V_6	V_6	V_1	V_1	V_1	V_2	V_2	V_2
	0	V_7	V_7	V_7	V_0	V_0	V_0	V_7	V_7	V_7	V_0	V_0	V_0	V_7	V_7	V_7	V_0	V_0	V_0
	-1	V_5	V_6	V_6	V_6	V_1	V_1	V_1	V_2	V_2	V_2	V_3	V_3	V_4	V_4	V_4	V_2	V_5	V_5

Fig. 3.6 shows the control of stator flux linkage by selection of the suitable voltage vectors.

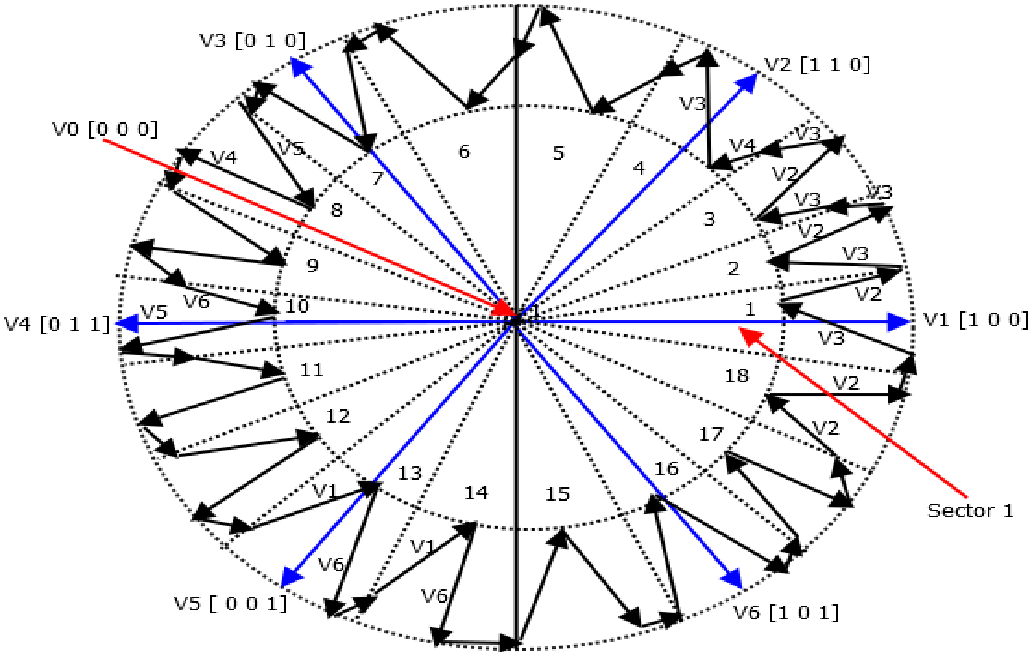

Fig. 3.6: Proposed motor air-gap flux zigzag path.

3.6.2 Modified DTFC Table with 5-level torque hysteresis Comparators

In the proposed eighteen-sector based DTFC, six voltage vectors are used in all eighteen-sector. But, still the performance of the DTFC scheme can be improved with the idea of small torque increase instead of torque increase, mainly due to the fact that the tangential voltage vector component is very small and consequently the torque variation will be small as well. Fig. 3.7 shows the eighteen-sector modified DTFC where FD/FI denotes flux decrease/increase, TD/TI denotes torque decrease/increase, TsD/TsI denotes torque small decrease/increase, respectively. It is obvious that, V_1 will produce a large increase in flux and small increase in torque in sector S_{18} . On the contrary, V_2 will increase the torque in large proportion and the flux in a small one.

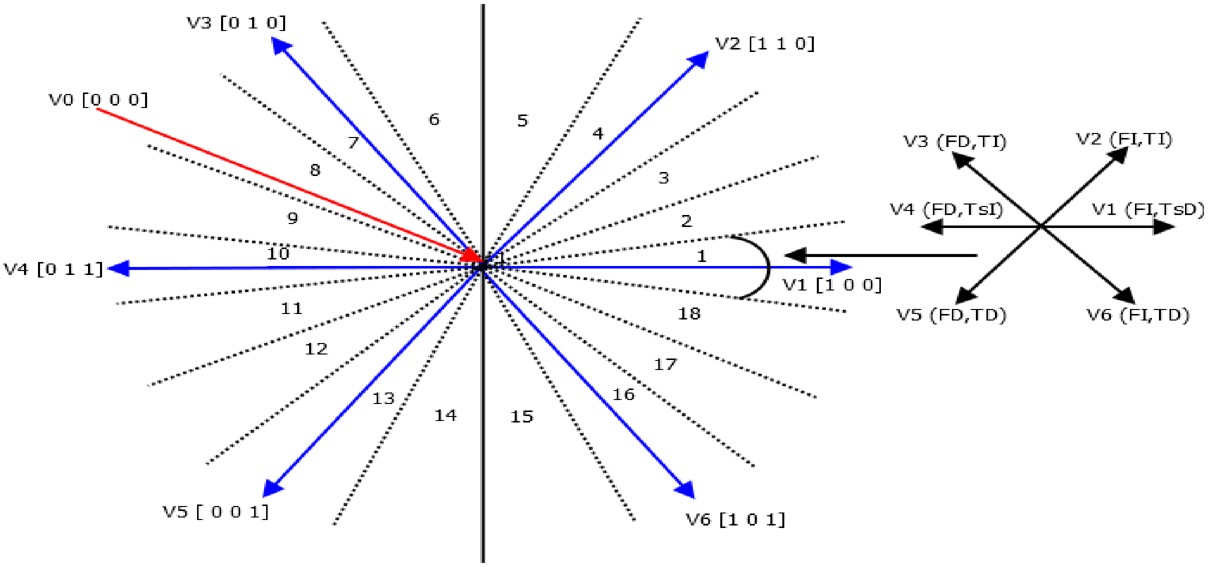

Fig. 3.7: Modified eighteen sector DTFC with five level torque hysteresis comparators.

If the flux and torque effects are divided into eight groups, torque ripples are further reduced which is shown in Fig. 3.8.

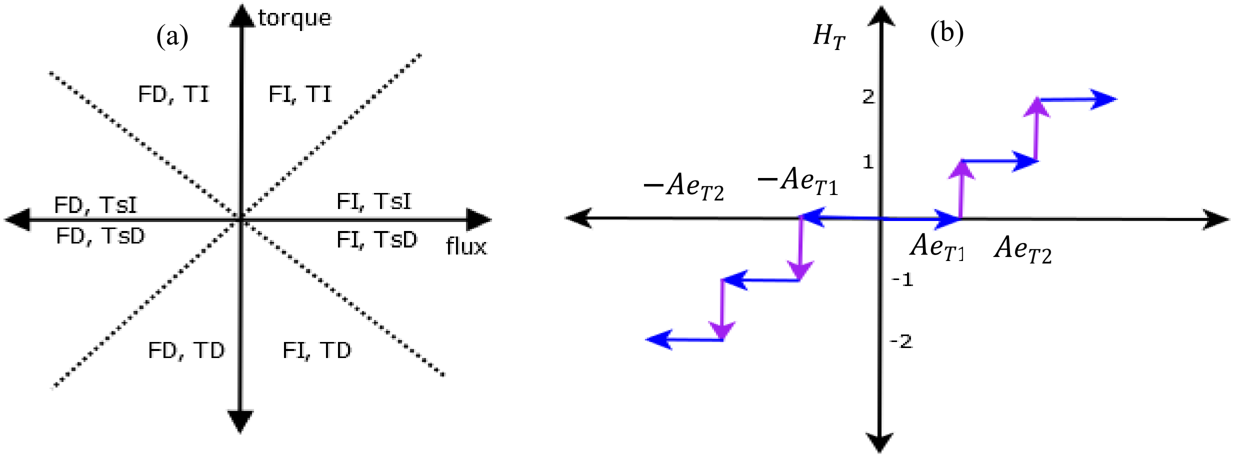

Fig. 3.8: Modified DTFC scheme: (a) Flux and torque variation; (b) five level torque hysteresis comparators.

Finally, a switching table is developed where torque errors are divided into small intervals. The flux increase and decrease is denoted by +1 and -1. The torque hysteresis is considered as

1, 2, -2, and -1. Look-up table for inverter switching with eighteen sector based DTFC and 5-level torque hysteresis comparator is shown in Table. 3.2.

Table 3.2: Five level torque hysteresis comparator based DTFC look-up table

H_ψ	H_T	S_1	S_2	S_3	S_4	S_5	S_6	S_7	S_8	S_9	S_{10}	S_{11}	S_{12}	S_{13}	S_{14}	S_{15}	S_{16}	S_{17}	S_{18}
+1	+2	V_2	V_2	V_3	V_3	V_3	V_4	V_4	V_4	V_5	V_5	V_5	V_6	V_6	V_6	V_1	V_1	V_1	V_2
	+1	V_2	V_2	V_2	V_3	V_3	V_3	V_4	V_4	V_4	V_5	V_5	V_5	V_6	V_6	V_6	V_1	V_1	V_1
	0	V_0	V_0	V_0	V_7	V_7	V_7	V_0	V_0	V_0	V_7	V_7	V_7	V_0	V_0	V_0	V_7	V_7	V_7
	-1	V_1	V_1	V_1	V_2	V_2	V_2	V_3	V_3	V_3	V_4	V_4	V_4	V_5	V_5	V_5	V_6	V_6	V_6
	-2	V_6	V_1	V_1	V_1	V_2	V_2	V_2	V_3	V_3	V_3	V_4	V_4	V_5	V_5	V_5	V_5	V_6	V_6
-1	+2	V_3	V_3	V_3	V_4	V_4	V_4	V_5	V_5	V_5	V_6	V_6	V_6	V_1	V_1	V_1	V_2	V_2	V_2
	+1	V_4	V_4	V_4	V_5	V_5	V_5	V_6	V_6	V_6	V_1	V_1	V_1	V_2	V_2	V_2	V_3	V_3	V_3
	0	V_7	V_7	V_7	V_0	V_0	V_0	V_7	V_7	V_7	V_0	V_0	V_0	V_7	V_7	V_7	V_0	V_0	V_0
	-1	V_7	V_5	V_0	V_6	V_7	V_1	V_0	V_2	V_7	V_3	V_0	V_4	V_7	V_5	V_0	V_6	V_7	V_1
	-2	V_5	V_6	V_6	V_6	V_1	V_1	V_1	V_2	V_2	V_2	V_3	V_3	V_4	V_4	V_4	V_2	V_5	V_5

3.7 Conclusion

This chapter details the improvement of conventional DTFC scheme for IPMSM drive. Firstly, LMA is incorporated in the proposed DTFC to estimate the motor air gap flux linkage in order to minimize the losses in electric machines. Secondly, unbalance voltage effects in one sector of conventional DTFC is reduced by adding additional twelve sectors. Finally, as the tangential component of voltage vector is reduced by additional twelve sectors therefore, torque ripples are further reduced by introducing the idea of small torque increase through 5-level torque hysteresis comparators. The following chapter details the simulation model of the conventional and proposed DTFC scheme of IPMSM drive.

Chapter 4

Simulation of Novel DTFC and LMA based IPMSM Drive

4.1 Introduction

The performance of the proposed DTFC and LMA based IPMSM drive is investigated extensively in a simulation environment using MATLAB/Simulink software.

The constant reference flux performance of the proposed DTFC scheme is also compared with the classical six-sector DTFC scheme to demonstrate the improvement in dynamic performance and efficiency over a wide speed range. The proposed DTFC scheme is tested in simulation for step change in command speed, load and parameter variations. The simulation tests are shown in the following sections, and are intended to reflect typical operational scenarios which include system with constant flux and six sector, system with LMA and six-sector, system with LMA and eighteen-sector. At the end, five level torque hysteresis comparator based DTFC scheme is simulated to see the dynamic speed and torque response in comparison to conventional 3-level torque hysteresis comparator.

4.2 Simulation Software

Using mathematical model of IPMSM drive incorporating LMA, comprehensive system is developed in MATLAB/Simulink software. Mathematical model contains the inverter block, IPMSM block, torque and flux estimation block and sector calculation block. Each stage of the system is expressed in Simulink as a function reflecting the mathematical model. After system development in MATLAB/Simulink software, the performance of the proposed DTFC is investigated. The Simulink block diagram of the proposed eighteen-sector based DTFC incorporating LMA is shown in Appendix B. The parameters of the IPMSM used in simulation are shown in Appendix A.

4.3 Simulation Results

Extensive simulation investigations are performed for the proposed eighteen-sector and LMA based IPMSM drive. Sample results are presented below. Figs. 4.1 (a) and (b) show the starting responses of the six-sector LMA based DTFC and proposed eighteen-sector LMA based DTFC scheme of IPMSM drive, respectively at rated conditions (183 rad/s and 19 Nm). It is clearly seen from Figs. 4.1 (a) and (b) that, motor torque ripples are reduced significantly with proposed eighteen-sector LMA based DTFC while maintaining similar speed and efficiency responses as compared to the conventional six-sector LMA based DTFC scheme.

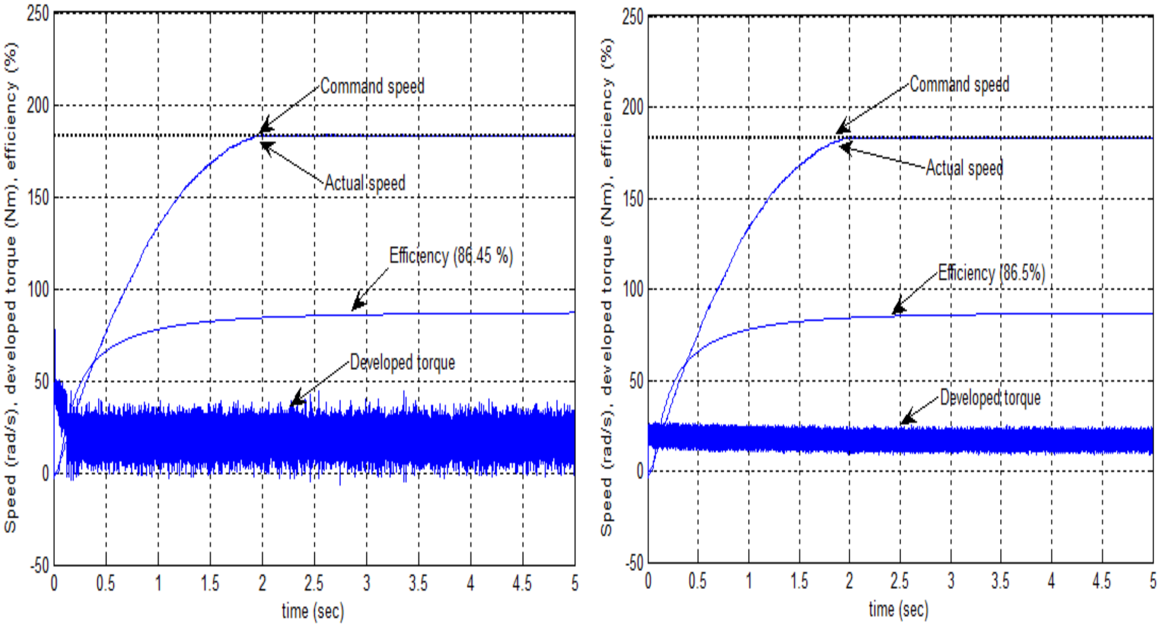

(a) (b)

Fig. 4.1: Speed, torque and efficiency responses of LMA based DTFC scheme at rated conditions: (a) six-sector based DTFC; (b) proposed eighteen-sector based DTFC.

Figs. 4.2(a) and (b) show the comparative dynamic performance analysis of the proposed eighteen-sector LMA based DTFC with conventional six-sector LMA based DTFC scheme for step change of command speed from 30~183 rad/s in a step of 30 rad/s at rated load (19 Nm). It is seen from Fig. 4.2 (b) that, for the proposed eighteen-sector based DTFC scheme torque ripple is confined to a small bandwidth without any abrupt peak from low speed up to the rated speed whereas conventional six-sector LMA based DTFC scheme contains higher torque ripples in steady state. Therefore, proposed DTFC maintains higher dynamic performance over a wide speed range of operation while both the proposed and conventional system follows the command speed quickly without any oscillations. Fig. 4.3 shows the speed, d and q axis current responses of the proposed eighteen-sector based DTFC scheme incorporating LMA at rated conditions. It is found that d-axis current is negative which indicates that the proposed LMA can utilize the reluctance torque to optimize the efficiency. Fig. 4.4 shows the balanced three phase current response of the proposed eighteen-sector based DTFC scheme incorporating LMA at rated conditions which verifies the balanced operation of the drive system.

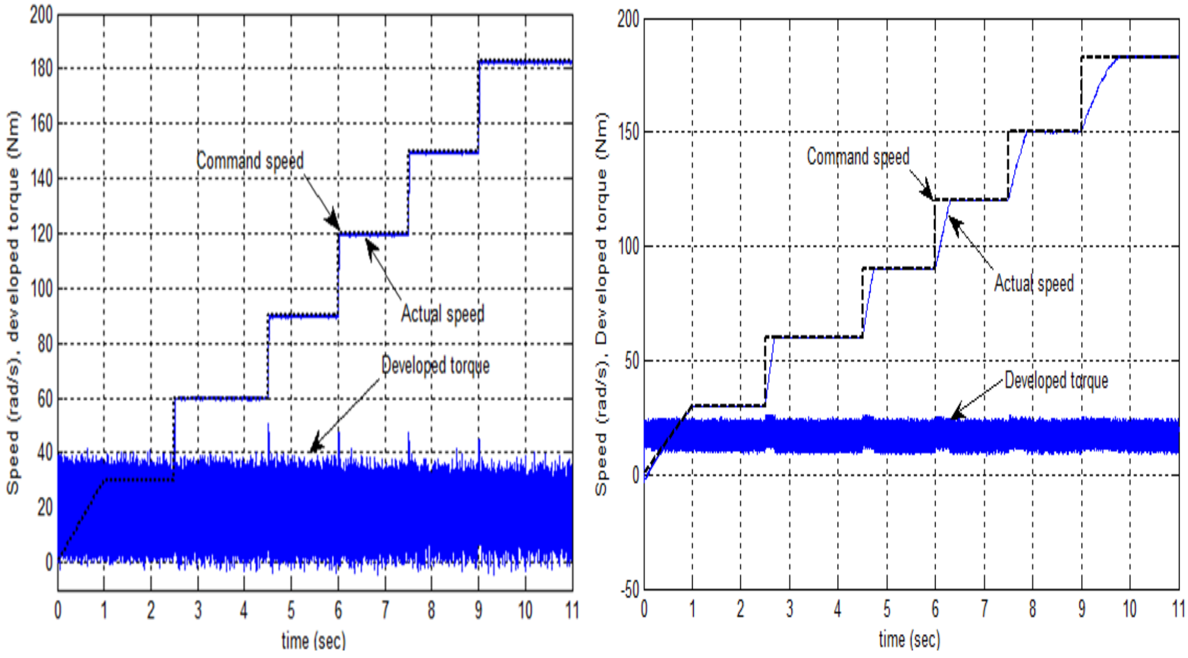

(a) (b)

Fig. 4.2: Simulated speed and torque responses of DTFC scheme incorporating LMA for a step change in command speed from 30~183 rad/s at rated load (19 Nm): (a) six-sector based DTFC; (b) proposed eighteen- sector based DTFC.

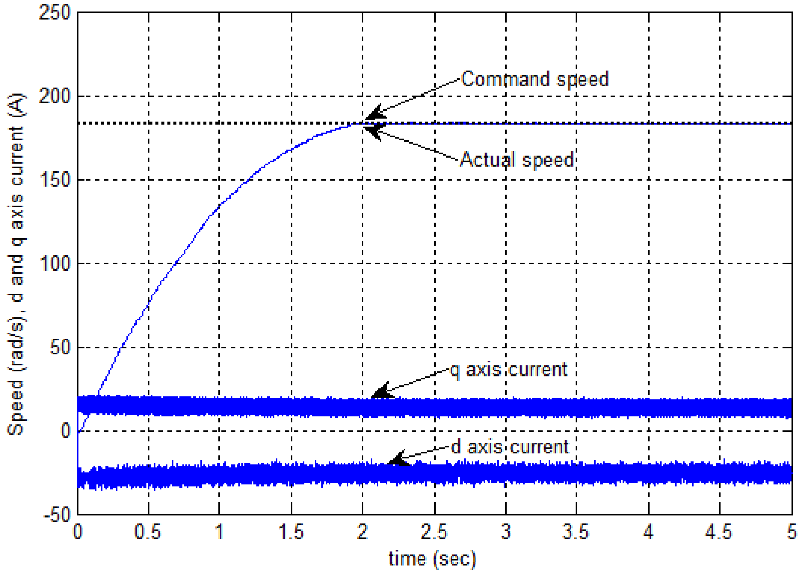

Fig. 4.3: Simulated speed, d and q axis current responses of the proposed eighteen-sector based DTFC scheme incorporating LMA at rated conditions.

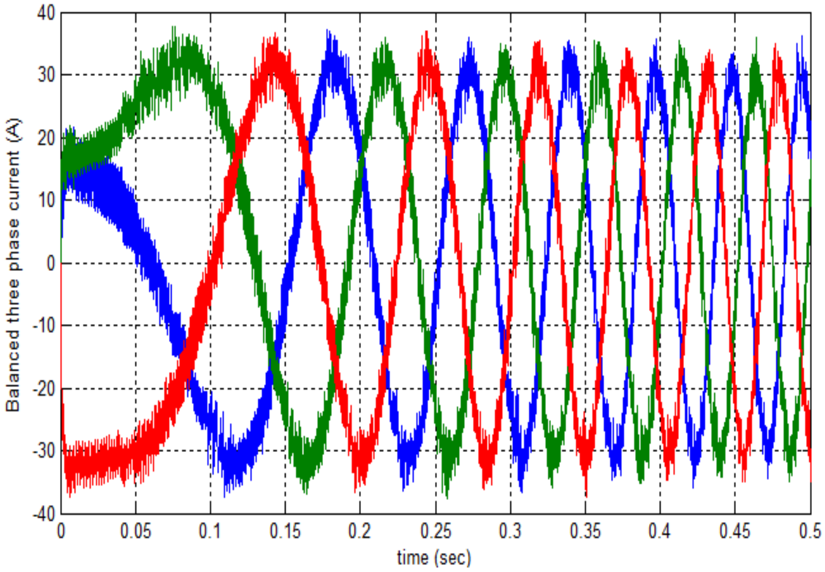

Fig. 4.4: Simulated three phase current responses of the proposed eighteen-sector based DTFC scheme incorporating LMA at rated conditions.

Fig. 4.5 shows the speed; torque and efficiency responses of the proposed eighteen-sector based DTFC incorporating LMA drive for a step change in command speed from 30 rad/s to 183 rad/s in a step of 30 rad/s. It is found that the motor can follow the command speed smoothly while maintaining higher efficiency (≥86%) over a wide speed range. It is also seen from Fig. 4.5 that the proposed DTFC scheme has lower torque ripples from low speed to the rated speed. Fig. 4.6 shows that for step change of command speed from 30~183 rad/s, stator current increases hence, the d-axis demagnetizing current i_d increases in the negative direction. On the other hand, q-axis current i_q remains constant as the load remains constant (19 Nm).

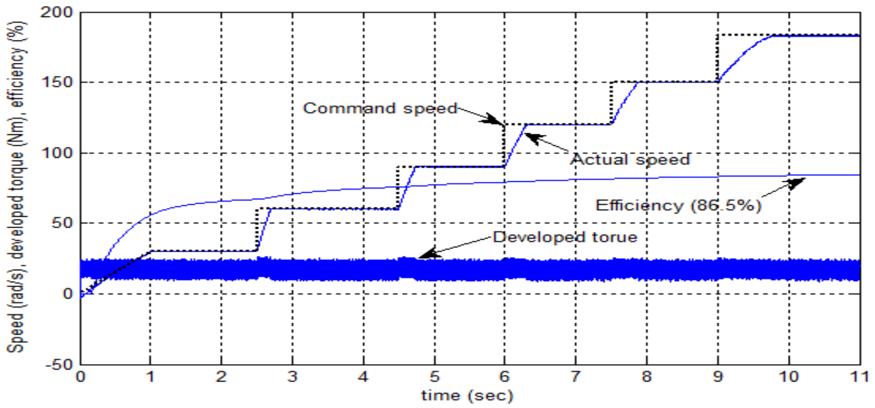

Fig. 4.5: Simulated responses of the proposed eighteen-sector based DTFC scheme incorporating LMA for a step change in command speeds from 30~183 rad/s at rated load: speed, efficiency and developed torque.

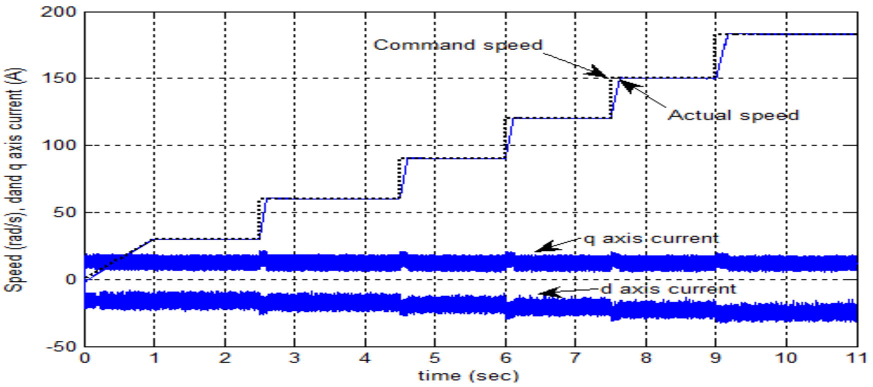

Fig. 4.6: Simulated responses of the proposed eighteen-sector based DTFC scheme incorporating LMA for a step change in command speeds from 30~183 rad/s at rated load: speed, d and q axis current responses.

Fig. 4.7 shows that for a step change of command speed from 30~183 rad/s, the stator air gap flux decreases, although most of the researchers consider it constant for the operation of DTFC scheme. This is due to the fact that the stator current increases, and hence, the d-axis demagnetizing current i_d increases with the increase in speed. Thus, the stator air-gap-flux decreases with the increase in speed. Robustness of the drive system is important for high performance drive applications as change of load is very common type of disturbance. Fig. 4.8 shows that, if the motor is operated at rated speed for a step change of load torque from 4~19 Nm in a step of 5 Nm, the speed can follow the command speed without any overshoot or undershoot and developed torque maintains higher dynamic performance in steady state.

Fig. 4.9 (a) shows the motor speed, developed torque and efficiency responses for a step change in command speed from 30~183 rad/s in a step of 30 rad/s at rated load with conventional constant-flux-based DTFC scheme. If the command flux value is kept constant at rated value of 0.184 V/rad/s, the motor was not able to follow the command speed. It can be seen from Fig. 4.9 (a) that the motor was able to follow up to 165 rad/s, but the efficiency was almost same as the proposed eighteen-sector based DTFC scheme incorporating LMA. If the command speed is more than 165 rad/s, the motor became unstable and came to stop. Fig. 4.9 (b) shows the corresponding results with low constant flux (0.139 V/rad/s). In this case, the motor can follow the command speed smoothly, but the efficiency was very low (especially at low speed) as compared to the proposed eighteen-sector based DTFC scheme. These scenarios happen due to the nonoptimum value of the stator flux as it changes with operating conditions for the PMSM drive.

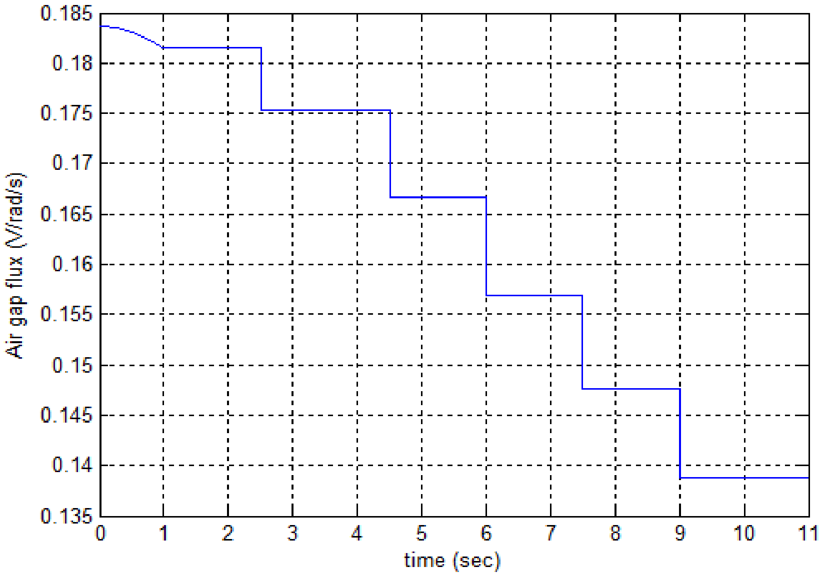

Fig. 4.7: Simulated responses of the proposed eighteen-sector based DTFC scheme incorporating LMA for a step change in command speeds from 30~183 rad/s at rated load (19Nm): estimated flux response.

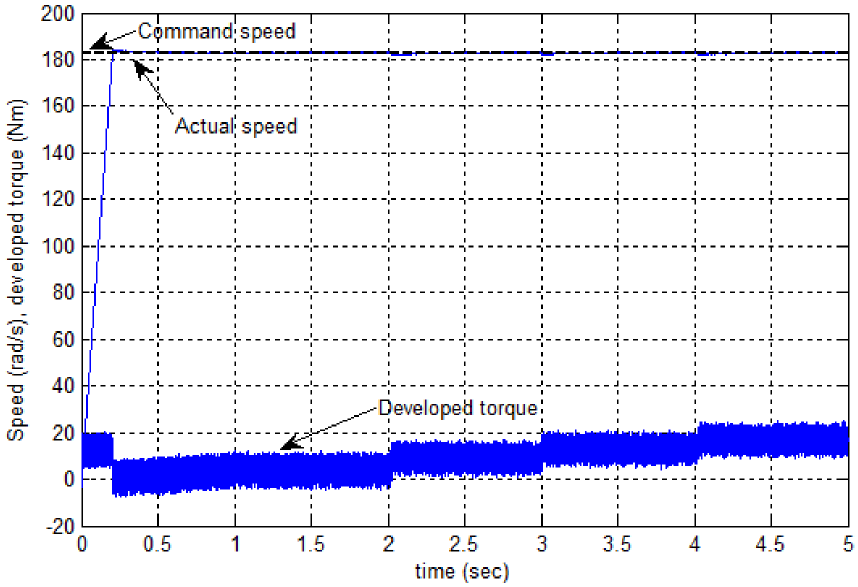

Fig. 4.8: Simulated responses of the proposed eighteen-sector based DTFC scheme incorporating LMA for a step change in load from 4~19 Nm in a step of 5 Nm at rated speed: speed and developed torque response.

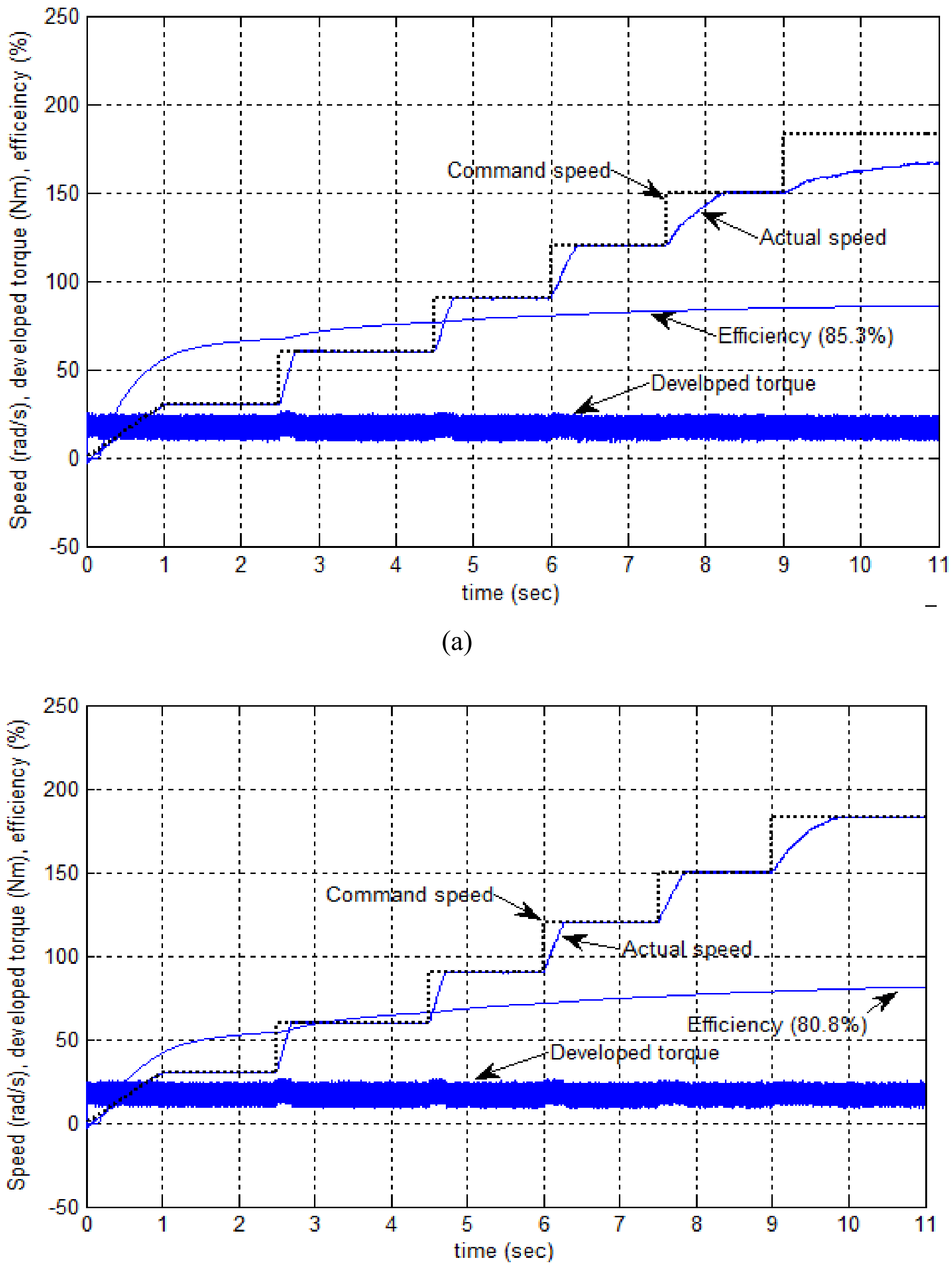

(a)

(b)

Fig. 4.9: Motor speed, developed torque and efficiency responses for a step changes in command speed from 30~183 rad/s at rated load with (a) constant rated flux command value (0.184 V/rad/s) and (b) constant low flux command value (0.139 V/rad/s).

Figs. 4.10 (a) and (b) show the speed, efficiency and load torque responses of the proposed eighteen-sector based DTFC incorporating LMA and conventional constant flux (0.184 V/rad/s) based DTFC scheme, respectively for a step change in load torque from 4 Nm to 19 Nm in a step of 5 Nm. It is found from Fig. 4.10 (a) that the proposed eighteen-sector based DTFC incorporating LMA drive can follow the command speed smoothly at different load conditions. However, the efficiency is relatively low at light load conditions. On the other hand, constant-flux-based DTFC has same efficiency response but the speed cannot follow the command speed at rated load and drops at 165 rad/s is shown in Fig. 4.10 (b).

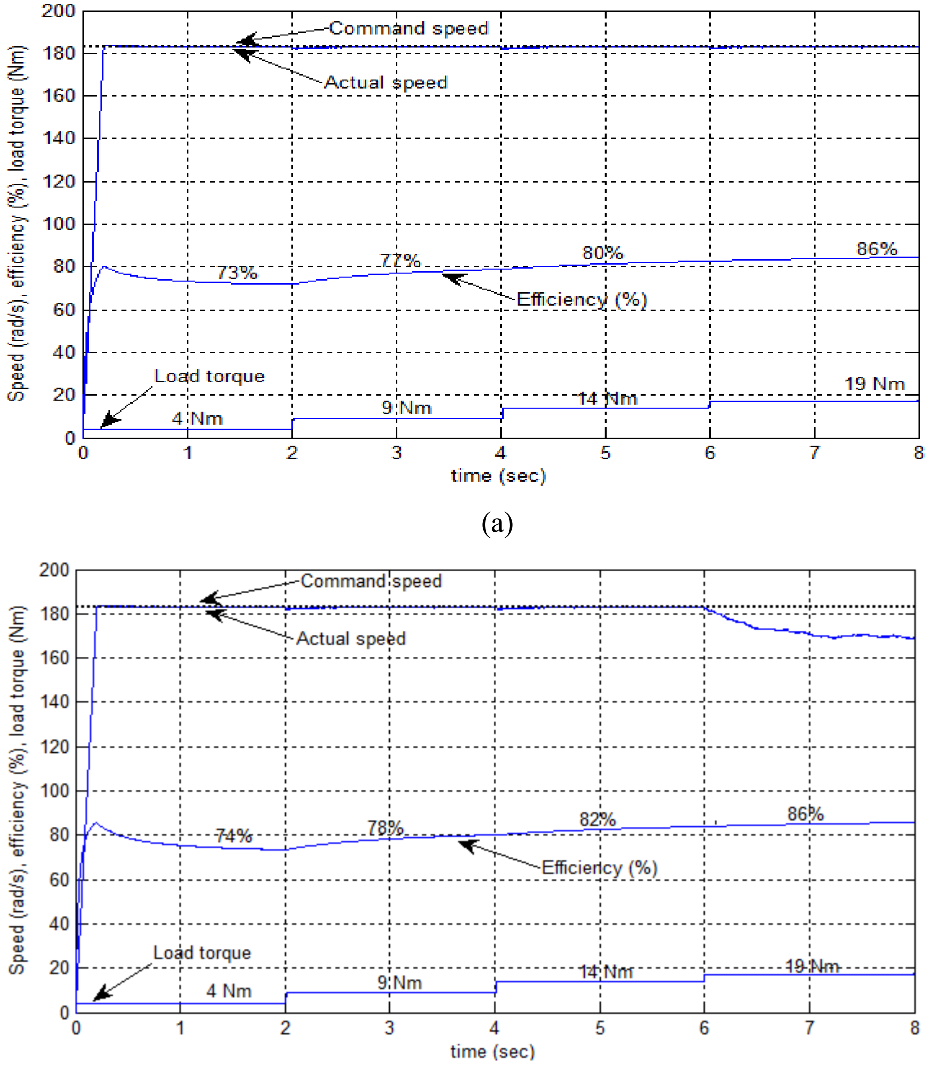

(a)

(b)

Fig. 4.10: Simulated speed, efficiency and load torque response's for a step change in load at rated speed: (a) proposed DTFC incorporating LMA; (b) constant flux (0.184 V/rad/s) based DTFC.

Figs. 4.11 and 4.12 show the comparative performance analysis of the conventional VC scheme with the proposed eighteen-sector based DTFC scheme incorporating LMA, respectively at rated conditions. It is clearly seen that the speed response of the VC is faster than that of the DTFC scheme but efficiency of the proposed DTFC based drive system (86.5%) is higher than that of the VC scheme (85.4%). In the case of developed torque the VC scheme contains higher torque ripples as compared to the proposed DTFC scheme. Therefore, proposed eighteen-sector based DTFC incorporating LMA maintains higher efficiency and better dynamic performance over wide speed range operation.

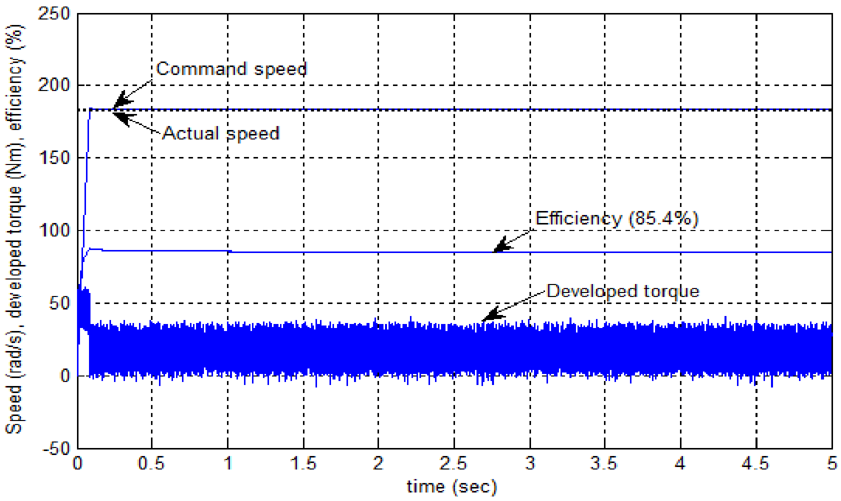

Fig. 4.11: Speed, developed torque and efficiency responses of the VC scheme at rated conditions.

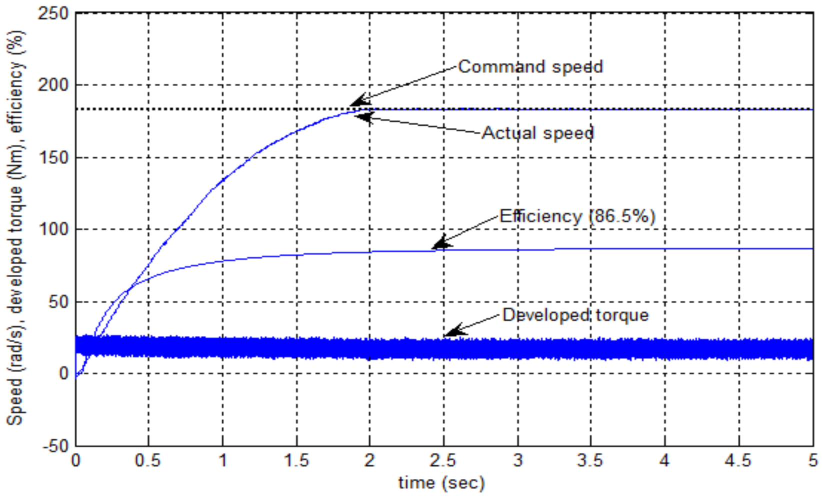

Fig. 4.12: Speed, developed torque and efficiency responses of the proposed eighteen-sector based DTFC scheme incorporating LMA at rated conditions.

Figs. 4.13 show the comparative dynamic performance and efficiency analysis of the proposed eighteen-sector based DTFC incorporating LMA with the conventional VC scheme for step change of load torque from 4~19 Nm in a step of 5 Nm at rated speed (183rad/s). It is seen from Fig. 4.13 (b) that, for the proposed DTFC torque ripple is confined to a small bandwidth without any abrupt peak whereas conventional VC scheme contains higher torque ripples in steady state. It found that the proposed DTFC has higher efficiency than that of the conventional VC scheme both in light load and rated load conditions whereas proposed and conventional VC drive follow the command speed smoothly at different load conditions.

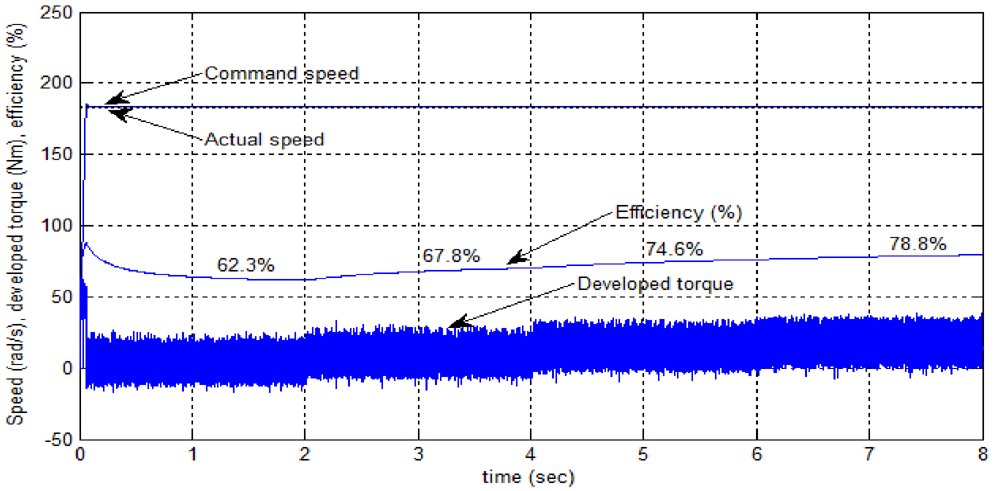

(a)

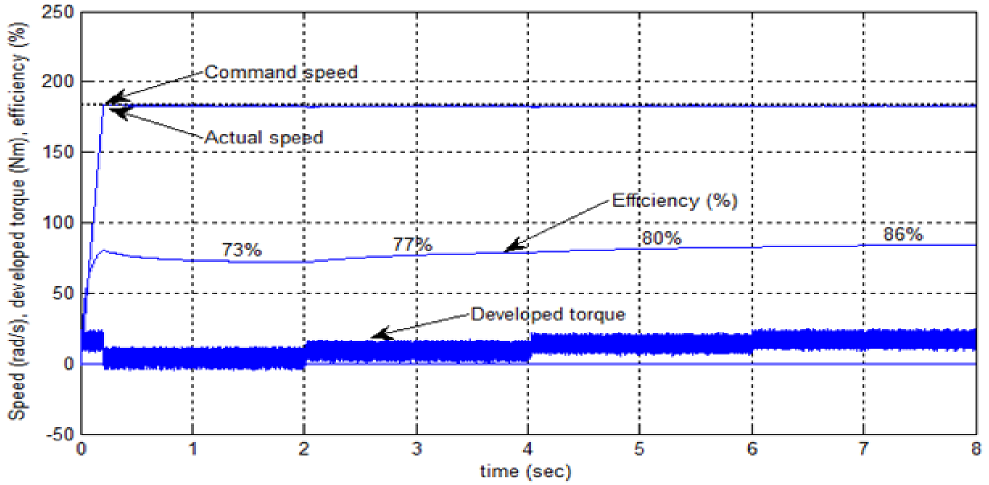

(b)

Fig. 4.13: Simulated speed, developed torque and efficiency responses for a step change in load from 4~19 Nm in a step of 5 Nm at rated speed: (a) conventional VC scheme; (b) proposed DTFC scheme.

Fig. 4.14 shows the comparative three phase stator current responses of the proposed DTFC and conventional VC schemes. For the fair comparison, the LMA is incorporated in both DTFC and VC scheme. It is found that the proposed DTFC takes less stator current than that of the conventional VC scheme in both transient and steady state. Thus, the VC scheme takes more input power from the source to carry the same load which signifies that the power loss in VC scheme is higher as compared to the proposed eighteen-sector based DTFC scheme incorporating LMA. Therefore, VC scheme creates more thermal stress on the motor. Figs. 4.15 show the locus of the stator flux of the drive system at rated conditions in the stationary frame. It is noticed that the flux profile attains circular shape very quickly which means that the stator flux has fast transient response. Comparative stator flux locus shows that the proposed eighteen-sector based DTFC incorporating LMA of IPMSM drive is nearly ripple free as compared to the eighteen-sector constant flux and conventional six-sector based DTFC scheme.

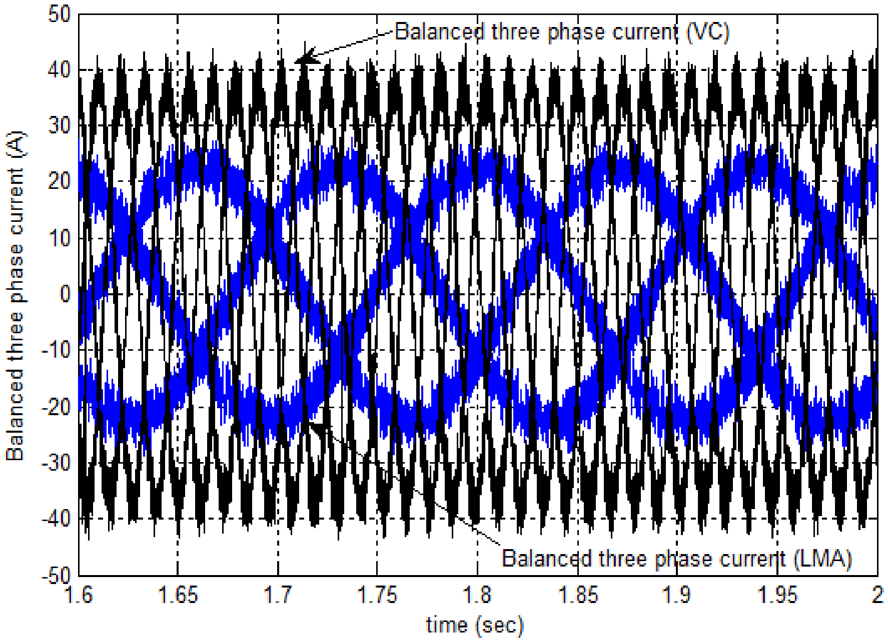

Fig. 4.14: Balanced three phase stator current comparison between proposed eighteen-sector based DTFC incorporating LMA and conventional VC schemes.

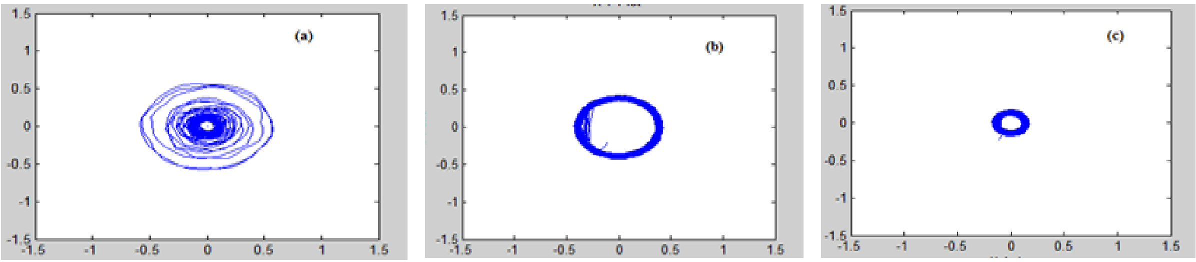

Fig.4.15: Locus of the stator flux in stationary frame at rated conditions: (a) Conventional six-sector based DTFC scheme; (b) eighteen-sector constant flux based DTFC scheme; (c) proposed eighteen-sector based DTFC scheme incorporating LMA.

Fig. 4.16 shows the comparative developed torque analysis of the three level and proposed five level torque hysteresis comparator based DTFC scheme at rated conditions. It is clearly seen that, the proposed five level torque hysteresis comparator based DTFC maintains lower torque ripples as compared to the three level torque hysteresis comparator based DTFC scheme. Blue one indicates the developed torque with five level torque hysteresis comparators whereas black one indicates the developed torque with three level torque hysteresis comparators.

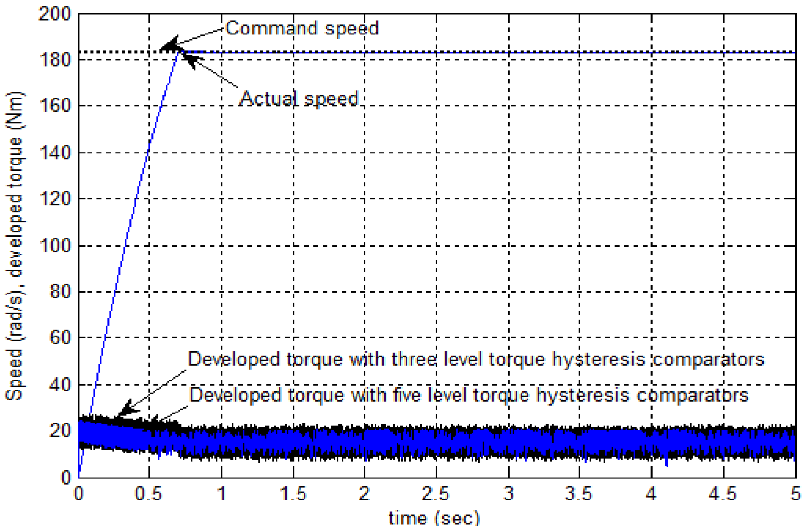

Fig.4.16: Developed torque performance analysis of three level and proposed five level torque hysteresis comparator based DTFC.

4.4 Conclusion

The simulation result presented in this Chapter is successful in several aspects. Motor efficiency is improved using LMA and motor developed torque ripple is reduced using the proposed eighteen-sector based DTFC. The torque ripple is further reduced by five level torque hysteresis comparators. The following Chapter details the experimental verification of the proposed eighteen-sector based DTFC scheme incorporating LMA.

Chapter 5

Real Time Implementation

5.1 Introduction

Simulation results may be used as an indication of relative performance, however are insufficient and ultimately do not provide realistic enough results to make appropriate conclusions. Therefore, this Chapter is devoted to the experimental verification of the proposed IPMSM drive. It concisely provides the details of DSP controller DS1104 and other supporting equipment used in the experimental verifications. The experimental setup and extensive real time results are presented to prove the effectiveness of the proposed eighteen-sector based DTFC scheme incorporating LMA.

5.2 Hardware Overview & Implementation of the Drive

The block diagram of hardware schematic of VSI fed IPMSM is shown in Fig. 5.1. The DSP board DS1104 board is installed in PC with uninterrupted communication through dual port memory to implement the control scheme in real time [45-47]. The DS1104 board is mainly based on a Texas Instrument MPC8240 64-bit floating point digital signal processor. PPC603e processor is used which operates at a clock of 250 MHz with 32 bit cache. The DS1104 board has a 32 MB of SDRAM global memory and 8 MB of flash memory. Analog to digital (A/D) converter, digital to analog (D/A) and digital incremental encoders are used in digital systems for the DSP board. 16 bit microprocessor (TI TMS320F240) acts as a slave processor where slave processor is used only for I/O configuration. The motor currents are measured by the Hall Effect sensors, which has good frequency response and are fed to the DSP board through the A/D converter. As the motor neutral is not grounded therefore only two phase currents are fed back and the other phase current is calculated from them. The rotor position angle is measured by the incremental encoder that is mounted on the shaft of the rotor and the signal is fed back to the DSP board through encoder interface. In order to get better resolution, the encoders output is increased by 4 times by built-in 4 fold pulse to get 4096 pulses per revolution, which are fed to one of the two incremental encoder interface channels of the board. A 10-bit position counter is used to count the encoder pulses and is read by a calling function in the software. By using index pulse generated from the encoder the encoder is reset once per revolution. The motor speed is computed from the measured rotor position angles using numerical differentiation. The output current signals of the sensors are converted into voltage across the resistor connected between output terminals of the sensor and ground. The command voltages are generated and are compared with the triangular carrier wave. This generates logic signals which act as firing pulses for the inverters. Thus, six logic signals are the outputs of the DSP board and are fed to the base drive circuit of the IGBT inverter power module. The output of the digital I/O subsystem of the DS1104 is six pulses with a magnitude of 5 V which is shifted to +15 V through a base drive circuit.

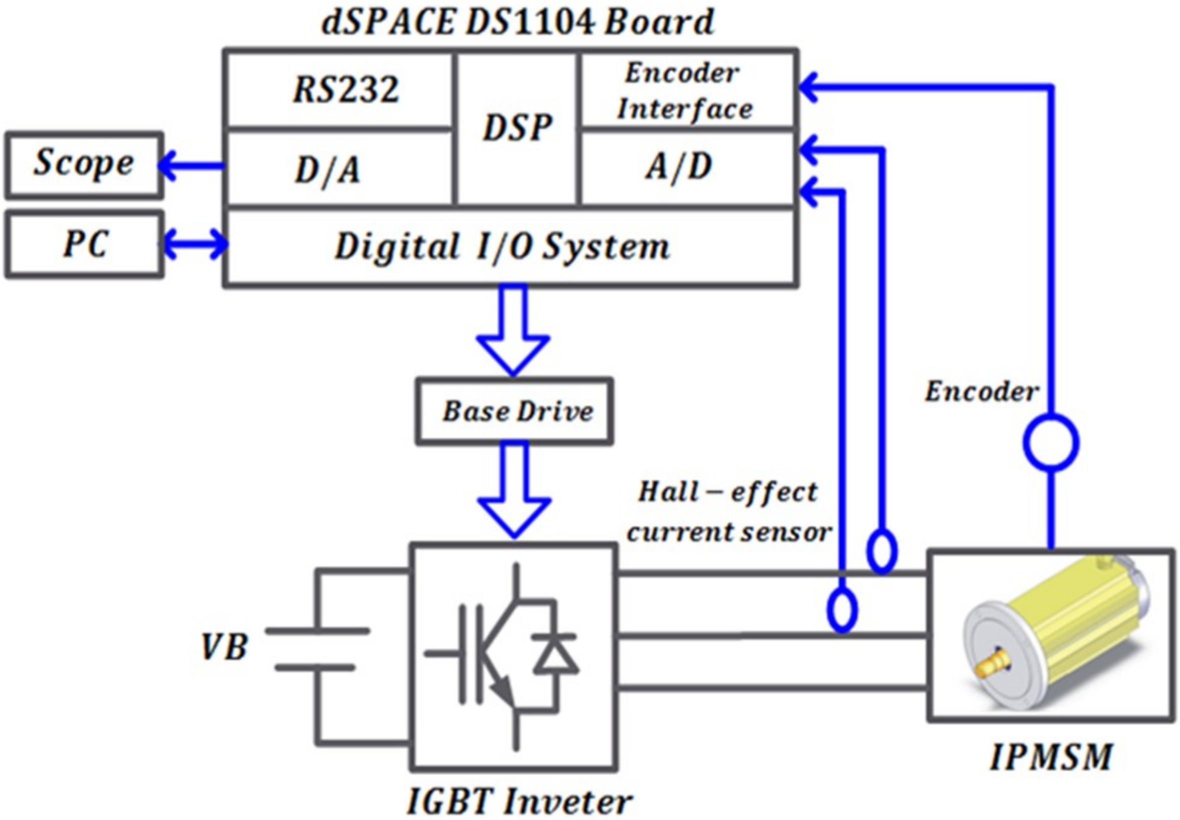

Fig. 5.1: Block diagram of hardware schematic of VSI fed IPMSM drive.

The drive system incorporates some major functional components that are detailed in Table 5.1, in conjuncture with the specific rating and manufacturer details that pertain to the thesis.

Table 5.1: System specifications & ratings

System Component	Manufacturer	Model	Characteristic(s)	Specification	Notes
Controller Board	dSPACE GmbH	DS1104	Clock frequency ADC DAC Encoder PWM	250 MHz 16-bit 16-bit 10-bit 12-bit	
Inverter	Semikron		DC supply Phase current Drive input	<750v <30A 0/15v	
Motor	Yaskawa	686SS	see Table 1		IPMSM
Current sensor		CS100A-P	Current rating	<100A	
Position sensor	Sumtak	LMA-102	Supply Resolution	12v 10-bit	
Power Supply	Sorensen	SGA 200/25	Voltage Current Ripple	200v 25A 0.02%	SMPS

5.3 Experimental Setup

The detailed experimental setup for the implementation of the proposed eighteen-sector based DTFC scheme incorporating LMA of IPMSM drive is shown in Fig. 5.2. A three phase autotransformer is used as a source of variable AC supply. It is connected to rectifier through a switch. A single assembly ‘RFI’ encompasses the rectifier, filtering capacitor and inverter. The DC bus voltage of the VSI is obtained by rectifying the ac voltage and filtered by a large capacitor (≈ 100 uF). The inverter is equipped with short circuit protection, under voltage and thermal abnormalities. The gating signals generated by the DSP board are available on its D/A ports. These signals are not strong to trigger the IGBTs of the inverter. Therefore, a driver circuit is used to increase the power level of the firing pulses so that these are sufficient to drive the IGBT switches. The gate driver circuit also provides isolation between low power control and the high power supply circuits. The inverter output is connected with the IPMSM drive. The actual motor currents are measured by Hall-effect current transducers. Interface circuit is located between the Hall-effect sensor and A/D channel of the DSP board. The speed of the IPMSM drive is measured by using an optical incremental encoder that is directly connected to the rotor shaft. The DSP board DS1104 is installed, in personal computer (PC). Analog signals that are coming through the D/A port of the DSP board are captured by the oscilloscope. The IPMSM is coupled with a DC machine which works as a generator to act as a loading machine to the motor. Resistors are connected as a load to the output voltage terminals of the DC machine. Each major component of the experimental system is labelled in Fig. 5.2.

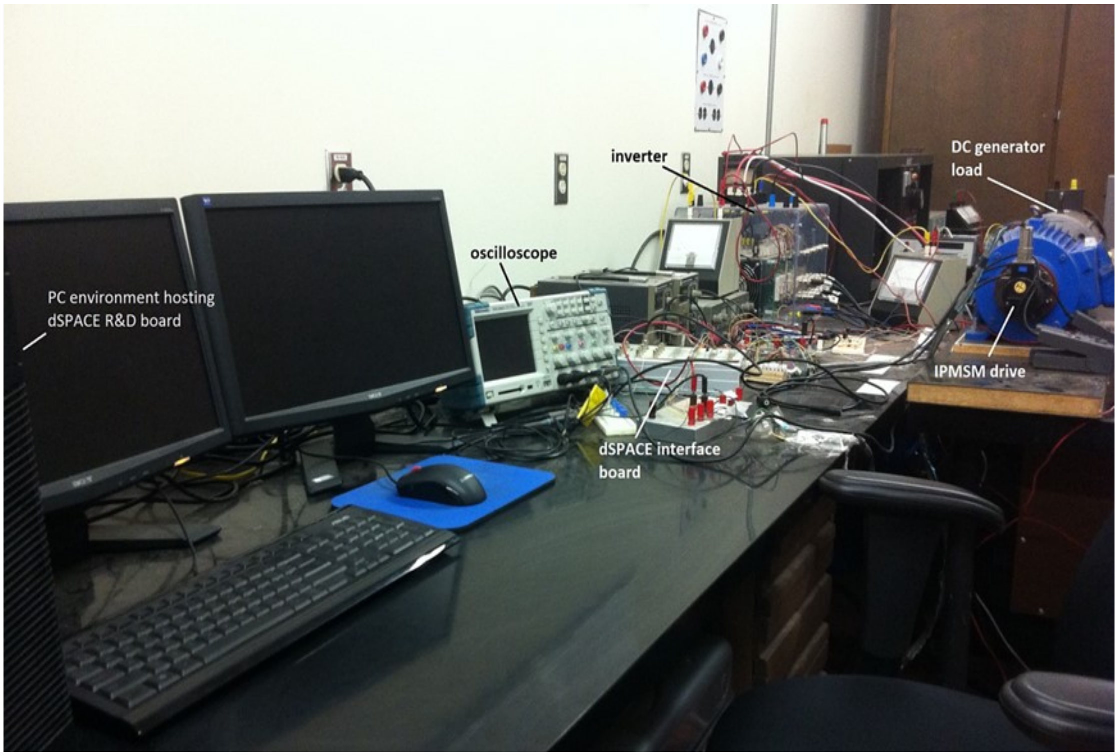

Fig. 5.2: Experimental setup.

5.4 Software Development

The DS1104 board is inherently equipped with the microprocessor. Therefore, it can work independently without using the PC. Though the processor is combined with the PC slot still it performs its entire task without using it. This board needs to download the drive system software for its functionality. As a result, the board requires that software to be created and downloaded to the board system. Therefore, to implement the control algorithm, a real-time Simulink model of the whole proposed system is developed (shown in Appendix F). Using the 'ControlDesk' software this model is downloaded to the DS1104 board.

Data from the ControlDesk user interface for command variables is sent to the DS1104, and data is returned to the user interface for monitoring system variables in real-time. The system may be controlled and monitored through the ControlDesk real time interface (RTI). This enables the user to create custom graphical interfaces, adding to the functionality of the DSP. The permissible maximum sampling frequency is 10 kHz, if it exceeds then 'overrun' error occurs, which indicates the computational burden of the processor. The flow chart for the real-time implementation of the proposed system is shown in Fig. 5.3. For start-up processes all the variables needs initializations. After initializations, the timer interrupt routine is set-up which reads the variables; stator currents, voltages and rotor positions by using the respective sensors. The signals measured by the sensors are adjusted so that they present the actual quantities. Using the speed error the reference motor torque is calculated by the processor of the board. Similarly, the calculation for estimated torque and flux linkage is performed by the processor using the drive software. To compute the gating signal for the VSI all the parameters such as stator voltages, currents and rotor speeds are stored in the memory. These gating signals are available at the I/O subsystem of the board and are applied to the IGBT switches through drive circuit. The process continues in cycle to run the IPMSM drive.

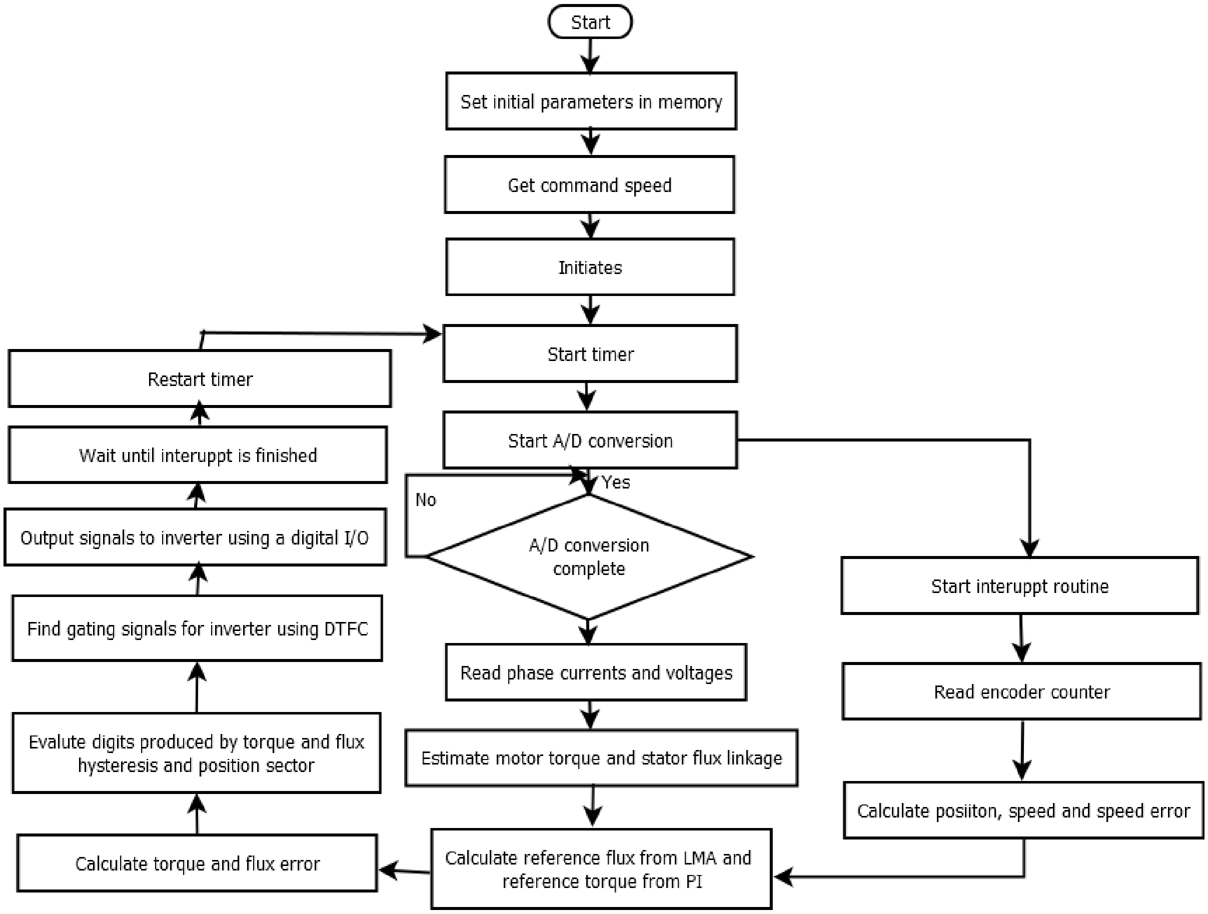

Fig. 5.3: Flow chart of the software development for real-time implementation of the proposed DTFC based IPMSM drive.

The DS1104 I/O for both the master and slave processors is made available through a connector panel (CP1104), exterior to the computer host which is shown in Fig. 5.4. In brief, the slave I/O is used for PWM output to the inverter, encoder is connected to “*Inc1*”, the current feedback is fed into “*ADC1/2*” and visualization of key system variables on an external oscilloscope may be achieved by using the 8 available digital to analog converter (DAC) channels.

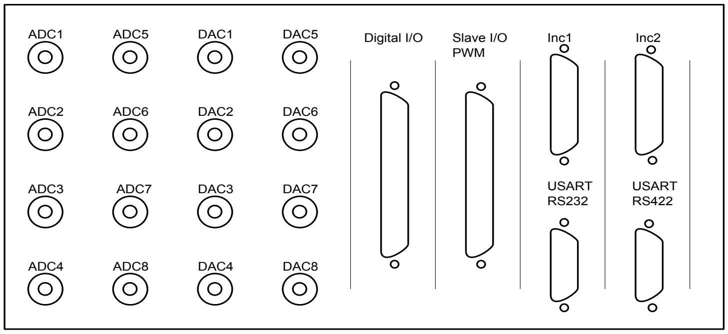

Fig. 5.4: CP1104 connection panel.

5.5 Feedback Systems

A feedback signal is essential for the closed loop control system. Position and indirectly angular velocity are measured using a 10-bit two quadrant indexed optical encoder with complementary outputs. The encoder is connected to "*Inc1*" on the connection panel, as seen in Fig. 5.4. The index pulse generated by the encoder is significant only at the start-up. At the time of starting as the index pulse is generated, the counter is reset to zero so that the maximum rotor angle equals 2π. The rotor speed is calculated by differentiation by differentiation from the present and past samples of rotor positions. The current feedback is acquired through dual Hall effect based sensors on phases "a" and "b", the sensor signals are conditioned and amplified to the 5V level before being fed into the "ADC1" and "ADC2" analog to digital channels on the CP1104.

5.6 Experimental Results

The effectiveness of the proposed eighteen-sector based DTFC scheme incorporating LMA is verified by the experimental work. Extensive experimental tests are carried out under various operating conditions of IPMSM drive. The parameters of the IPMSM used for the real time implementation of the DTFC scheme is given in Appendix-A. The results for conventional DTFC scheme are also given for the comparative purposes. Furthermore, performance of the proposed DTFC scheme is compared with the VC scheme to verify the effectiveness of the proposed scheme over VC scheme.

Fig. 5.5 shows the starting speed and d-q axis current responses of the proposed eighteen-sector based DTFC incorporating LMA scheme at initial low reference speed of 60 rad/s at no load. It is found from Fig. 5.5 (a) that the proposed DTFC can follow the command speed smoothly without any overshoot/undershoot. The d-q axis currents are shown in Fig. 5.5 (b). Fig. 5.6 shows the speed and efficiency responses of the proposed DTFC scheme at rated speed (183 rad/s) and 50% rated load. It is seen that, at rated speed condition proposed DTFC based IPMSM drive can follow the rated command speed smoothly and quickly while maintaining higher efficiency (85%) of the drive.

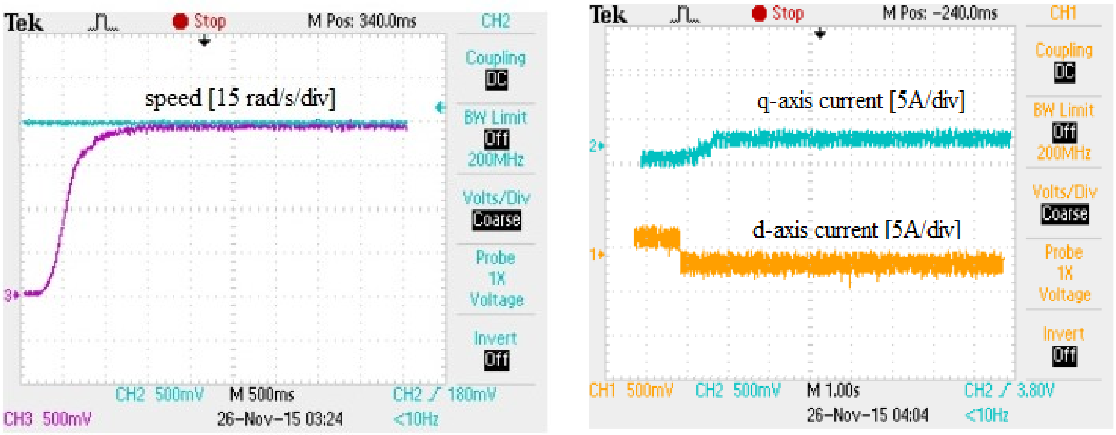

(a) (b)

Fig. 5.5: Experimental starting responses of the proposed DTFC at a speed of 60 rad/s and no load: a) speed; (b) d-q axis currents.

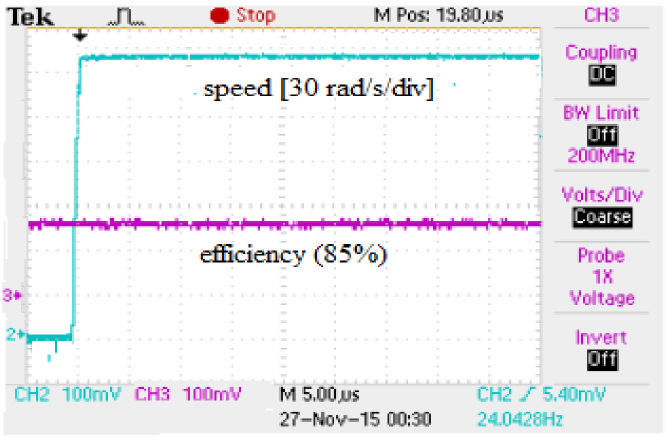

Fig. 5.6: Experimental speed and efficiency responses of the proposed DTFC at rated speed and 50% rated load.

Fig. 5.7 shows the speed response of the proposed eighteen-sector based DTFC scheme incorporating LMA based IPMSM drive for a step change in reference speed from 90-183 rad/s at 50% rated load. During the step command in speed, the proposed DTFC scheme demonstrates a rapid convergence to the command speed without any oscillations. Figure 5.8 shows the speed response of the proposed DTFC scheme for a command speed of 120 rad/s and for a step increase in load from 50%-75% of rated load. It is clearly seen that, there is a slight dip in speed, but the proposed eighteen-sector based DTFC scheme incorporating LMA drive can quickly recover the speed.

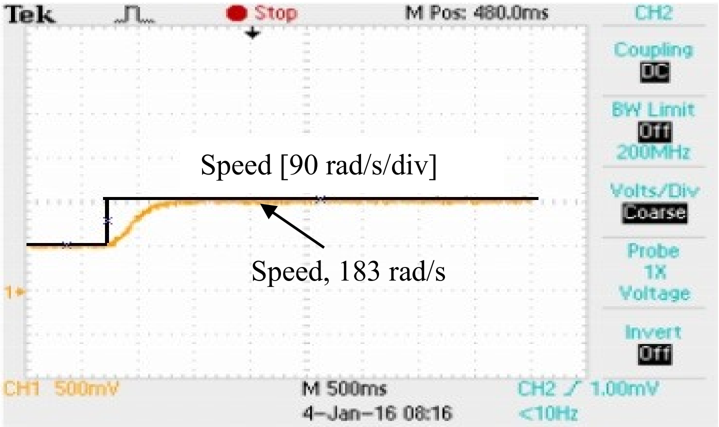

Fig. 5.7: Speed response of the proposed DTFC scheme for step change in command speed at 50% rated load.

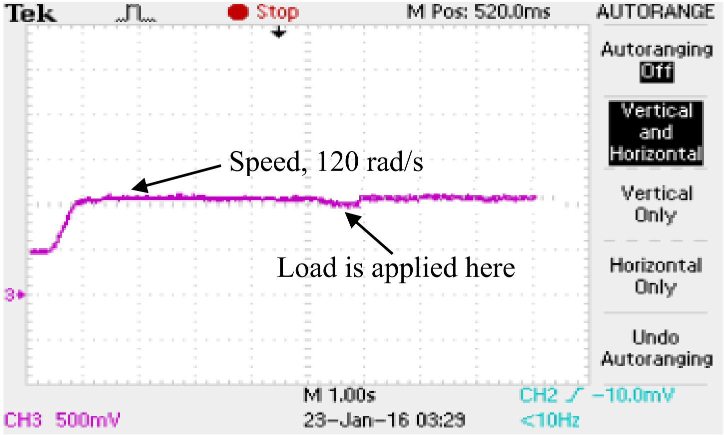

Fig. 5.8: Speed response of the proposed DTFC scheme for a step increase in load (50-75%).

Fig. 5.9 and 5.10 shows the steady state operation of the proposed DTFC and the conventional VC scheme at rated speed (183 rad/s) and 50% rated load, respectively. All traces are labelled on the oscilloscope image and magnitude per division is also indicated for each relevant channel. The proposed DTFC in Fig. 5.9 with eighteen-sector incorporating LMA is able to maintain the command speed with negligible variations. Fig. 5.10 shows the performance with the VC scheme. It is clearly seen from the Figs. 5.9 and 5.10 that, the proposed eighteen-sector based DTFC scheme incorporating LMA maintain low torque ripples as compared to the VC scheme at rated speed with 50% rated load.

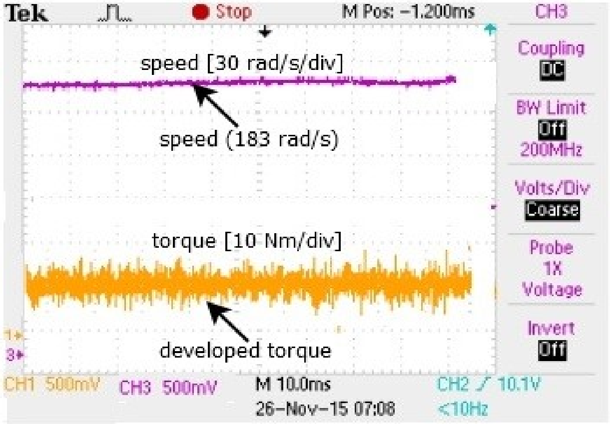

Fig. 5.9: Speed and torque response of the proposed DTFC scheme at rated speed and 50% rated load.

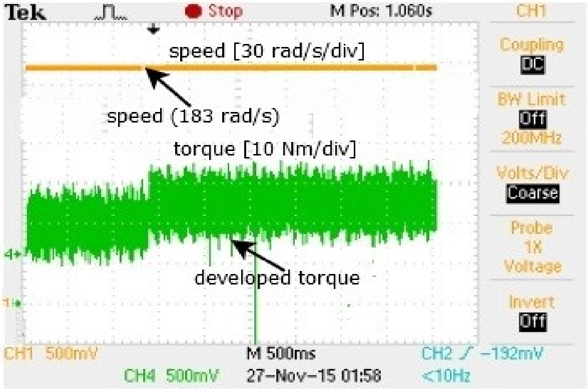

Fig. 5.10: Speed and torque response of the VC scheme at rated speed and 50% rated load.

Fig. 5.11 demonstrate the comparative dynamic performance analysis of the proposed eighteen-sector based DTFC incorporating LMA, eighteen-sector based DTFC with constant flux and six-sector based DTFC with LMA at rated speed and 50% rated load. It is found that the proposed DTFC scheme with LMA maintain the lowest torque ripple among all the control schemes. Therefore, real time result verifies the effectiveness of the proposed eighteen-sector based DTFC scheme.

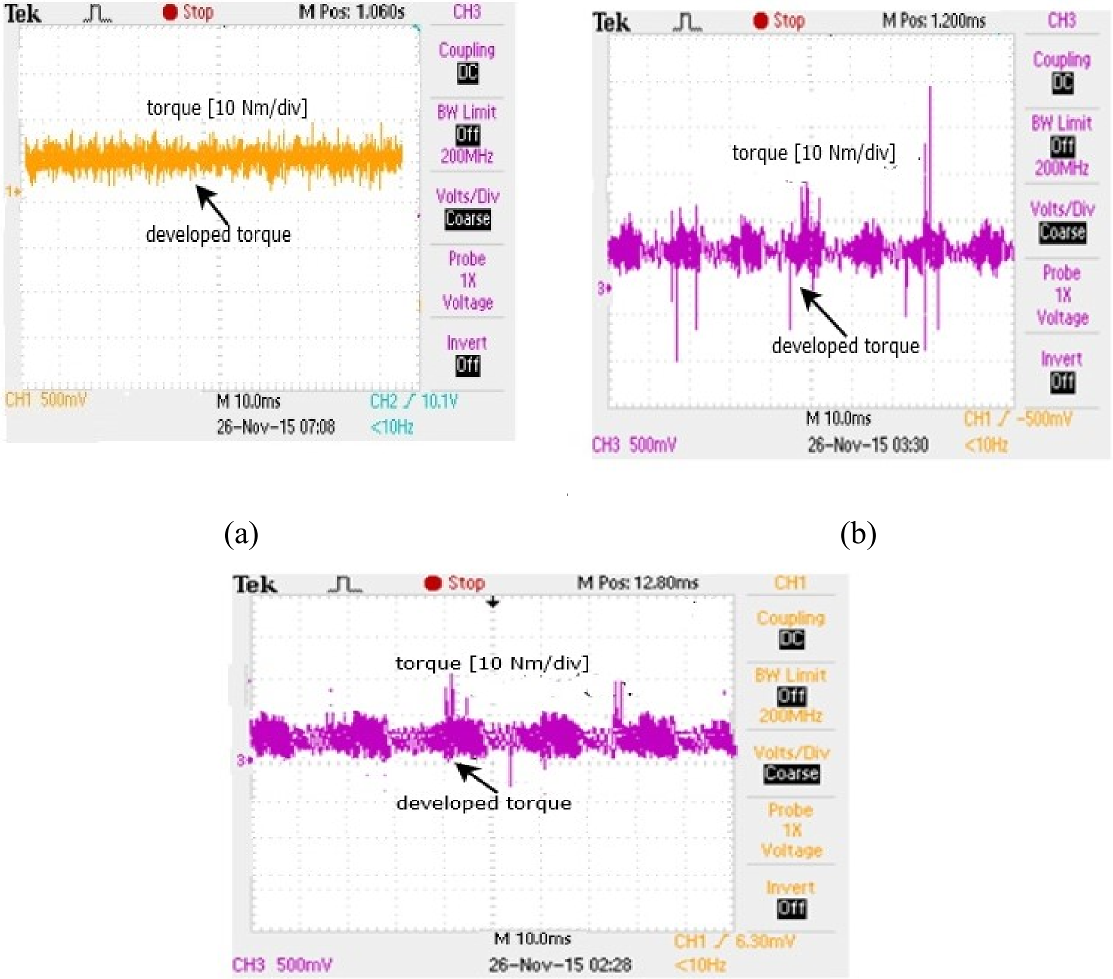

(a) (b)

(c)

Fig. 5.11: Torque responses at rated speed and 50% rated load: a) eighteen-sector based DTFC with LMA; (b) eighteen-sector based DTFC with constant flux; (c) six-sector based DTFC with LMA.

Finally, to verify that the phase currents are balanced, Fig. 5.12 shows the phase currents of the proposed eighteen-sector based DTFC scheme incorporating LMA. It is seen from the figure that, the phase currents are balanced thus ensures all assumptions made for reference frame transformation are corroborated experimentally. Fig. 5.13 shows the balanced three phase currents for the conventional VC scheme incorporating LMA where phase currents are slightly distorted.

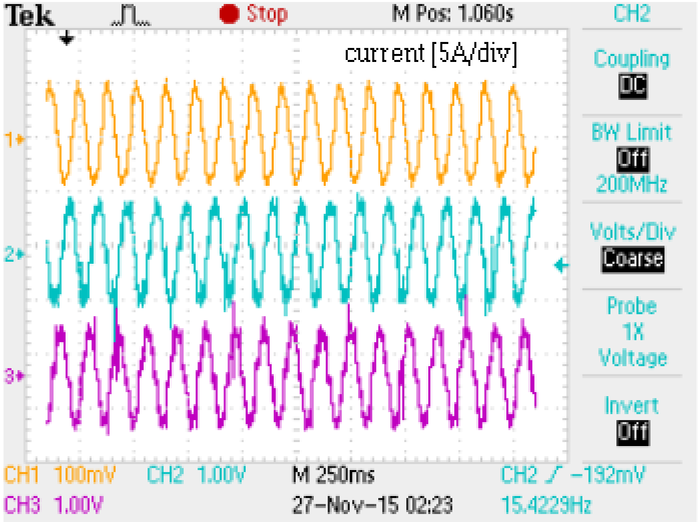

Fig. 5.12: Balanced phase currents of the proposed DTFC scheme.

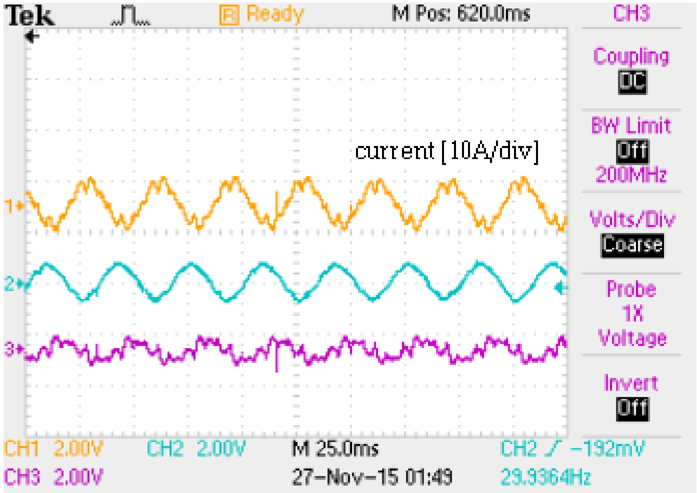

Fig. 5.13: Balanced phase currents of the VC scheme incorporating LMA.

5.7 Conclusion

A novel DTFC based efficiency and dynamic performance improvement of IPMSM drive for wide speed range of operation has been presented in this Chapter. The proposed DTFC has been thoroughly tested in a real-time experimental environment with a series of tests similar to that performed in simulation. The proposed DTFC scheme has been successfully implemented using the DSP board DS1104 for a prototype of 5-hp motor. A series of step speed response with the dynamic performance improvement have been documented in this section. Performance of the proposed DTFC has been compared with the conventional DTFC and VC scheme. The proposed DTFC demonstrated better dynamic performance while maintain higher efficiency during loading transitions. However, the torque ripple for the proposed eighteen-sector based DTFC scheme is still found an issue; therefore, in the next Chapter a novel nonlinear DTFC scheme considering both motor electromagnetic developed torque and air-gap flux linkage as virtual control variable is developed.

Chapter 6

Nonlinear Controller for IPMSM Drive Considering Torque and Flux as Control Variables

6.1 Introduction

Accurate regulation of motor speed maintaining high dynamic performance is key to many applications. Conventional and modified DTFC schemes still suffers from torque ripples. Therefore, this thesis further attempts to develop a nonlinear controller considering both motor electromagnetic developed torque and stator air-gap flux linkage as virtual control variables. Most of the existing nonlinear controllers are designed by considering d-q axis currents as control variables in vector control scheme. In order to take the advantage from both nonlinear and DTFC scheme, this thesis proposed a nonlinear controller of IPMSM drives by considering motor electromagnetic developed torque and air-gap flux linkage as virtual control variables.

Thus, the stability of the proposed nonlinear controller is verified through the Lyapunov's stability theory.

6.2 Control Techniques

Typical existing control methodologies of the DTFC have been rigorously detailed in the literature review section, and include linear, intelligent and model based control techniques. Among linear controllers, PI/PID type control is arguably most common for the DTFC control. However, nonlinear controllers are rarely applied for DTFC based AC motor drives.

Therefore, this thesis proposes a backstepping based nonlinear controller for IPMSM drive. In the first steps, motor electromagnetic developed torque is considered as virtual control variable and the performance of the controller is investigated. To overcome the limitations of the controller, this thesis further propose a nonlinear controller where motor electromagnetic developed torque and stator air-gap flux linkages are considered as control variable as like conventional DTFC and their respective error dynamics are forced to zero. Therefore, drawbacks of the conventional, modified DTFC and nonlinear controller with torque as a virtual control variable can be improved by the proposed nonlinear controller.

6.3 Nonlinear Controller with Torque as Virtual Control Variable

The foundation of backstepping controller is the identification of a virtual control variable and forcing it to become a stabilizing function. Thus, it generates a corresponding error variable which can be stabilized by proper input selection via Lyapunov's stability theory [42-44]. In backstepping based nonlinear controller, command d and q axis input voltages are developed to guarantee high speed tracking performance of the IPMSM [41]. The first step of the velocity tracking is to select the input variable with proper value to ensure the convergence of the motor speed to the command speed. In order to derive the control algorithms the mathematical model of IPMSM as derived in Chapter 2 is considered.

$$\frac{di_d}{dt}=\frac{1}{L_d}[v_d-R_s i_d+P\omega_r L_q i_q] \tag{6.1}$$

$$\frac{di_q}{dt}=\frac{1}{L_q}[v_q-R_s i_q-P\omega_r L_d i_d-P\omega_r \psi_m] \tag{6.2}$$

$$\frac{d\omega_r}{dt}=\frac{1}{J}[T_e-T_L-B_m\omega_r] \tag{6.3}$$

$$T_e=\frac{3}{2}P[\psi_d i_q-\psi_q i_d] \tag{6.4}$$

$$\frac{d\psi_d}{dt}=v_d-R_s i_d \tag{6.5}$$

$$\frac{d\psi_q}{dt}=v_q-R_s i_q \tag{6.6}$$

$$\Psi=\psi_d^2+\psi_q^2 \tag{6.7}$$

The main basis of nonlinear controller design is to force the error between reference and actual speeds to zero. The speed error is defined as,

$$e_\omega=\omega_r^*-\omega_r \tag{6.8}$$

where: e_ω= speed error, ω_r = actual motor speed and ω_r^*= speed reference.

Differentiating and substituting state expression (6.8) yields:

$$\dot{e_\omega}=-\dot{\omega_r}=\frac{1}{J}(B_m\omega_r+T_L-T_e) \tag{6.9}$$

where:

$\dot{e_\omega}$= rate of change of speed error (error dynamic)

Figure 6.1 shows the block diagram of proposed backstepping based nonlinear controller taking into consideration motor electromagnetic developed torque as a virtual control variable.

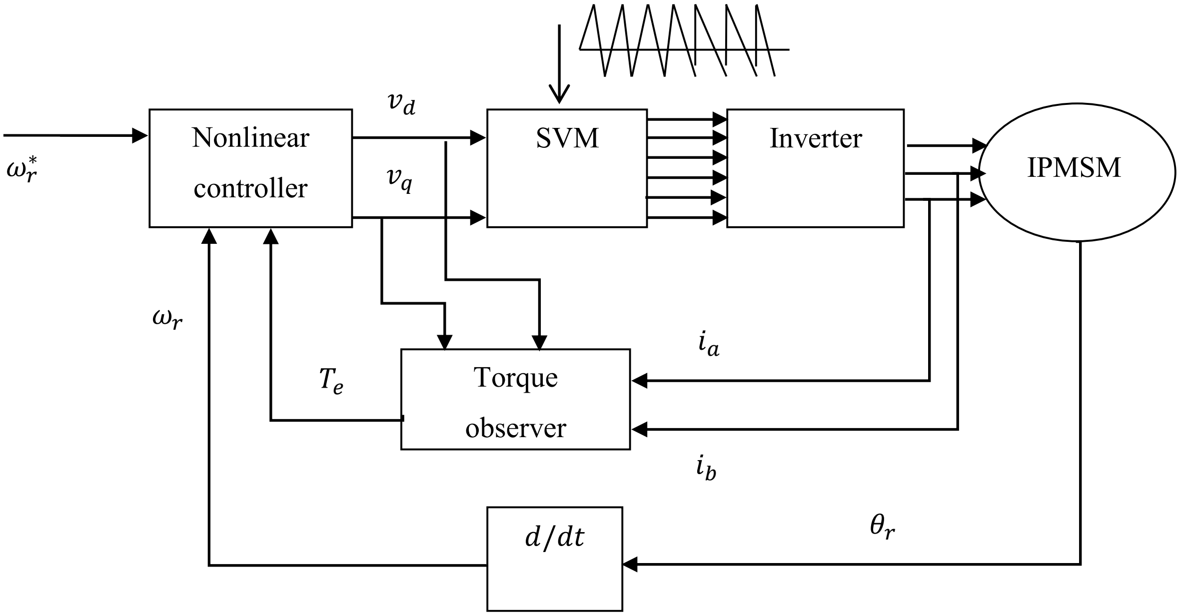

Fig. 6.1: Block diagram of backstepping based nonlinear controller with torque as control variable.

Note that the reference speed derivative may be regarded as zero, except in instances of rapid change, and thus will be regarded as having an insignificant contribution to the error dynamic. Considering the Lyapunov's function as, $V=\frac{1}{2}e_\omega^2$, the derivative of the Lyapunov's function is given by,

$$\dot{V}=e_\omega\dot{e_\omega}=\frac{e_\omega}{J}(B_m\omega_r+T_L-T_e) \tag{6.10}$$

In the first step of controller development, motor electromagnetic developed torque (T_e) is considered as the only control variable so that equation (6.10) becomes negative semi-definite. Therefore,

$$T_e^*=B_m\omega_r+T_L+k_\omega J e_\omega \tag{6.11}$$

The stability criterion for the preliminary Lyapunov's function is then validated, with the resultant Lyapunov's derivative term negative semi-definite.

$$\dot{V}=-k_\omega e_\omega^2 \tag{6.12}$$

where, k_ω is closed loop feedback gain. Therefore, if $k_\omega > 0$; then Lyapunov's function becomes negative semi-definite which ensures the asymptotic stability.

Defining the electromagnetic torque error,

$$e_T= T_e^* - T_e \tag{6.13}$$

For stabilizing the electromagnetic torque, the torque error dynamics can be defined as,

$$\dot{e_T} = \dot{T_e^*} - \dot{T_e} \tag{6.14}$$

From the derivative of reference electromagnetic torque,

$$\begin{aligned}\dot{T_e^*}&=B_m\frac{d}{dt}(\omega_r)+\frac{d}{dt}(T_L)+k_\omega J\frac{d}{dt}(e_\omega) = \frac{B_m}{J}[T_e-T_L-B_m\omega_r]+ k_\omega J * \frac{1}{J}(B_m\omega_r+T_L-T_e)\\
&=\frac{1}{J}[B_m*(T_e-T_L)-B_m * B_m\omega_r+k_\omega J * B_m\omega_r+k_\omega J * (T_L-T_e)]\\
&=\frac{1}{J}[(T_e-T_L)(B_m-k_\omega J)-B_m\omega_r(B_m-k_\omega J)]\\
&=\frac{1}{J}(B_m-k_\omega J)(T_e-T_L-B_m\omega_r)\end{aligned} \tag{6.15}$$

From the derivative of motor actual electromagnetic torque,

$$\dot{T_e}=\frac{d}{dt}[\frac{3}{2}P(\psi_d i_q\text{-}\psi_q i_d)]=\frac{3}{2}P[\psi_d\frac{d}{dt}(i_q)+\dot{\psi_d}i_q\text{-}\psi_q\frac{d}{dt}(i_d)\text{-}\dot{\psi_q}i_d] \tag{6.16}$$

Substituting the values of $\dot{T_e^*}$ and $\dot{T_e}$ in torque error dynamics equation (6.14),

$$\dot{e_T} = \dot{T_e^*} - \dot{T_e}=\frac{(B_m-k_\omega J)}{J}(T_e\text{-}T_L\text{-}B_m\omega_r)\text{-}\frac{3}{2}P\psi_d[\frac{1}{L_q}(v_q\text{-}R_si_q\text{-}P\omega_rL_di_d\text{-}P\omega_r\psi_m)]\text{-}\frac{3}{2}P(v_d\text{-}R_si_d)i_q+\frac{3}{2}P\psi_q[\frac{1}{L_d}(v_d\text{-}R_si_d+P\omega_rL_qi_q]+\frac{3}{2}P(v_q\text{-}R_si_q)i_d$$

$$=\frac{(B_m-k_\omega J)}{J}(T_e\text{-}T_L\text{-}B_m\omega_r)-\frac{3}{2}P\psi_d[\frac{1}{L_q}(\text{-}R_si_q\text{-}P\omega_rL_di_d\text{-}P\omega_r\psi_m)]+\frac{3}{2}P(i_d-\frac{\psi_d}{L_q})v_q+\frac{3}{2}P\psi_q[\frac{1}{L_d}(\text{-}R_si_d+P\omega_rL_qi_q)]\text{-}\frac{3}{2}P(i_q-\frac{\psi_q}{L_d})v_d \tag{6.17}$$

Based on the error dynamics, final Lyapunov's function including the speed and motor electromagnetic developed torque variables can be defined as,

$$V_1=\frac{1}{2}e_\omega^2+\frac{1}{2}e_T^2 \tag{6.18}$$

By differentiating the Lyapunov's function,

$$\dot{V_1}=e_\omega\dot{e_\omega}+e_T\dot{e_T} \tag{6.19}$$

Substituting the error dynamics value in equation (6.19),

$$\dot{V_1}=-k_\omega e_\omega^2+e_T[\frac{(B_m-k_\omega J)}{J}(T_e\text{-}T_L\text{-}B_m\omega_r)-\frac{3}{2}P\psi_d[\frac{1}{L_q}(\text{-}R_si_q\text{-}P\omega_rL_di_d\text{-}P\omega_r\psi_m)]+\frac{3}{2}P(i_d-\frac{\psi_d}{L_q})v_q+\frac{3}{2}P\psi_q[\frac{1}{L_d}(\text{-}R_si_d+P\omega_rL_qi_q)]\text{-}\frac{3}{2}P(i_q-\frac{\psi_q}{L_d})v_d] \tag{6.20}$$

The control d-q voltages are chosen as;

$$v_d = \frac{\psi_q}{L_d\left(i_q - \frac{\psi_q}{L_d}\right)}[-R_s i_d + P\omega_r L_q i_q + 2\frac{L_d}{3P\psi_q}k_T e_T] \tag{6.21}$$

$$v_q = \frac{\psi_d}{L_q\left(i_d - \frac{\psi_d}{L_q}\right)}[-R_s i_q - P\omega_r L_d i_d - P\omega_r \psi_m - \frac{2L_q}{3PJ\psi_d}[\frac{(B_m - k_\omega J)}{J}(T_e - T_L - B_m\omega_r)] \tag{6.22}$$

where, k_ω and k_T are feedback constants.

Substituting the v_d and v_q in equation (6.20),

$$\begin{aligned}\dot{V}_1 =& -k_\omega e_\omega^2 + e_T[\frac{(B_m - k_\omega J)}{J}(T_e - T_L - B_m\omega_r) - \frac{3}{2}P\psi_d[\frac{1}{L_q}(-R_s i_q - P\omega_r L_d i_d - P\omega_r\psi_m)] + \frac{3}{2}P(i_d - \\ & \frac{\psi_d}{L_q})v_q + \frac{3}{2}P\psi_q[\frac{1}{L_d}(-R_s i_d + P\omega_r L_q i_q)] - \frac{3}{2}P(i_q - \frac{\psi_q}{L_d})v_d] \\ =& -k_\omega e_\omega^2 + e_T\Bigg[\frac{(B_m - k_\omega J)}{J}(T_e - T_L - B_m\omega_r) - \frac{3}{2}P\psi_d[\frac{1}{L_q}(-R_s i_q - P\omega_r L_d i_d - P\omega_r\psi_m)] + \\ & \frac{3}{2}P(i_d - \frac{\psi_d}{L_q})\Bigg\{\frac{\psi_d}{L_q\left(i_d - \frac{\psi_d}{L_q}\right)}[-R_s i_q - P\omega_r L_d i_d - P\omega_r\psi_m - \frac{2L_q}{3PJ\psi_d}[\frac{(B_m - k_\omega J)}{J}(T_e - T_L - \\ & B_m\omega_r) + \frac{2L_q}{3P\psi_d}k_T e_T]\Bigg\} + \frac{3}{2}P\psi_q[\frac{1}{L_d}(-R_s i_d + P\omega_r L_q i_q)] - \frac{3}{2}P(i_q - \frac{\psi_q}{L_d})\Bigg\{\frac{\psi_q}{L_d\left(i_q - \frac{\psi_q}{L_d}\right)}[-R_s i_d + \\ & P\omega_r L_q i_q + 4\frac{L_d}{3P\psi_q}k_T e_T]\Bigg\}\Bigg]\end{aligned} \tag{6.23}$$

Equation (6.23) can be simplified in the following form,

$$\dot{V}_1 = -k_\omega e_\omega^2 - k_T e_T^2 \tag{6.24}$$

If k_ω, $k_T > 0$, then the Lyapunov's function guarantees asymptotic stability of the system.

6.4 Simulation Results of the Nonlinear Controller with Torque as Control Variable

The performance of the proposed backstepping based nonlinear controller of IPMSM drive has been investigated extensively at different operating conditions. Some results are presented below. The speed and torque responses of the proposed nonlinear based IPMSM drive at rated speed (183 rad/s) and 50% rated load is shown in Fig. 6.2. It is found from the Figure that the proposed controller can follow the command speed very quickly with speed overshoot at the starting. The corresponding speed and torque errors are shown in Figs. 6.3 (a) and 6.3 (b), where the speed and torque errors converge to zero. Thus, it ensures the global stability of the drive system which is the main goal to design the backstepping based nonlinear controller. The speed and d-q axis currents response at rated speed and 50% rated load is shown in Fig. 6.4 (a) and balanced three phase current responses are shown in Fig. 6.4 (b). The d-q axis current responses are found smooth with negligible ripple in steady-state.

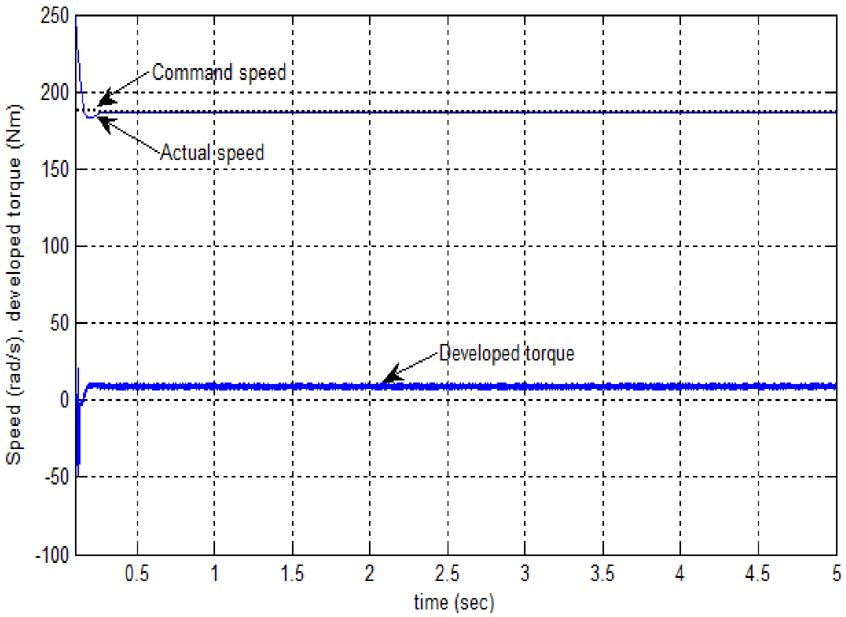

Fig.6.2: Simulated speed and developed torque responses of the proposed backstepping based nonlinear controller of IPMSM drive at rated speed (183 rad/s) and 50% rated load.

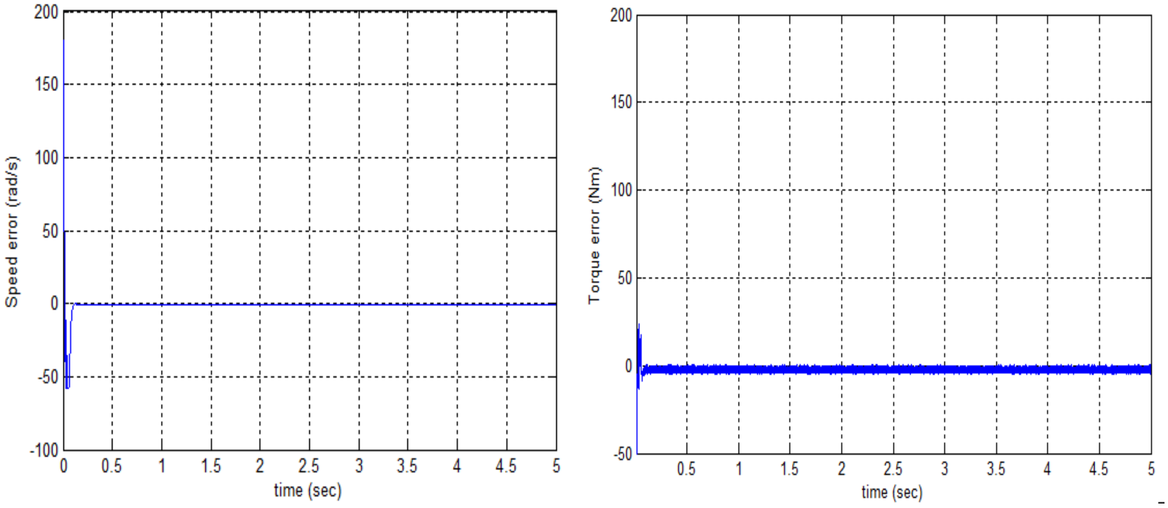

(a) (b)

Fig.6.3: Simulated response of the proposed backstepping based nonlinear controller at rated speed and 50% rated load: a) speed error; b) torque error.

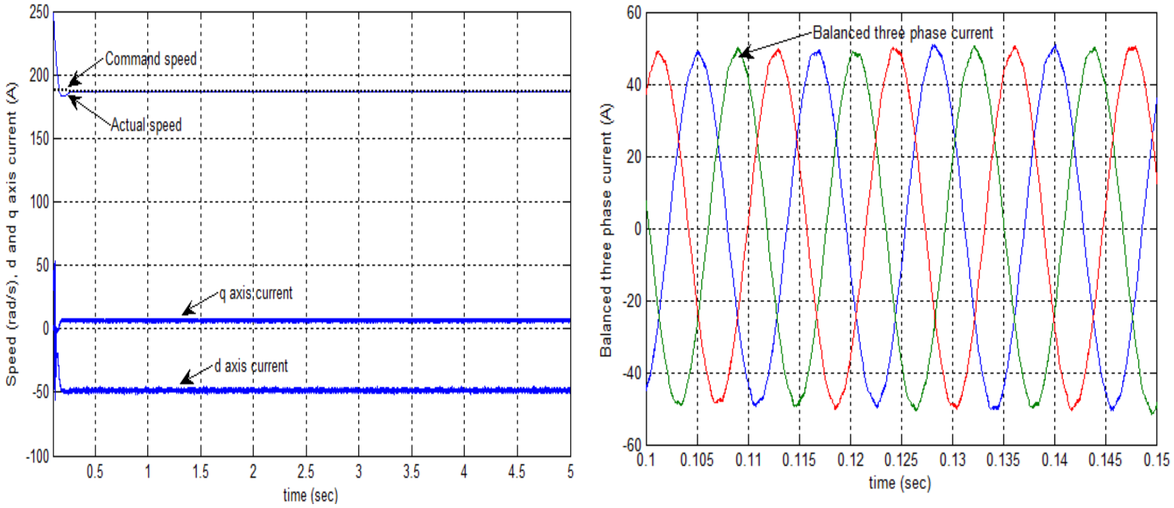

(a) (b)

Fig.6.4: Simulated responses of the proposed backstepping based nonlinear controller at rated speed and 50% rated load: a) speed, d and q axis current; b) balanced three phase currents.

Fig. 6.5 shows that the proposed backstepping based nonlinear controller of IPMSM drive can be operated above the rated speed where the motor speed follows the high command speed of 275 rad/s(1.5 times of the rated) speed with 15 Nm load. It is also found that the torque ripple is almost negligible compared to the torque response with earlier developed eighteen-sector based DTFC scheme incorporating LMA.

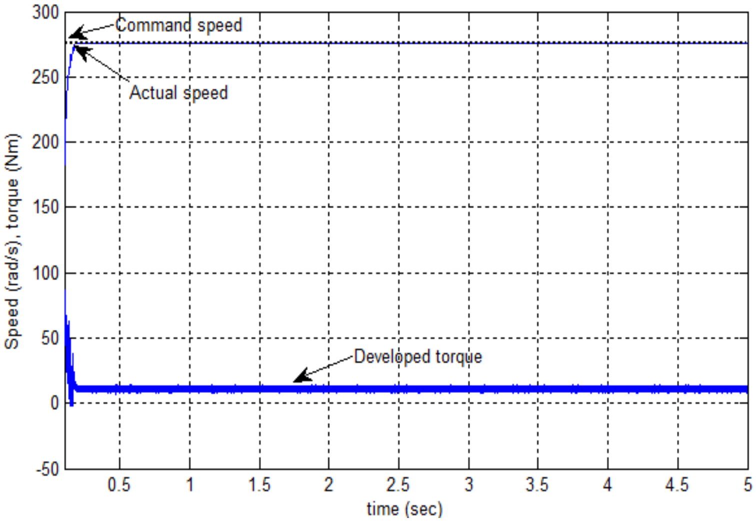

Fig.6.5: Simulated speed and developed torque response of the proposed backstepping based nonlinear controller of IPMSM drive at command speed of 275 rad/s and 15 Nm loads.

One important property of high performance drive is the robustness of the controller to the disturbance like change of load which is very common type of disturbance. The speed, torque, speed error and torque error responses with a step increase of load from 25% rated load to 50% rated load at rated speed of 183 rad/s are shown in Figs. 6.6, respectively. It is seen from the Fig. 6.6 that, the proposed controller shows better performance for sudden change in load at t= 2.5 sec. Although there is a small deviation of speed with change of load but it converges within minimum time to the reference speed. It is seen that for the proposed controller due to increase of load from 25% rated load to 50% rated load, the torque component of the current increases. The developed torque converges to load torque with change of load and all error variables converge to zero. The developed torque response shows that at steady state condition there are lower torque ripples.

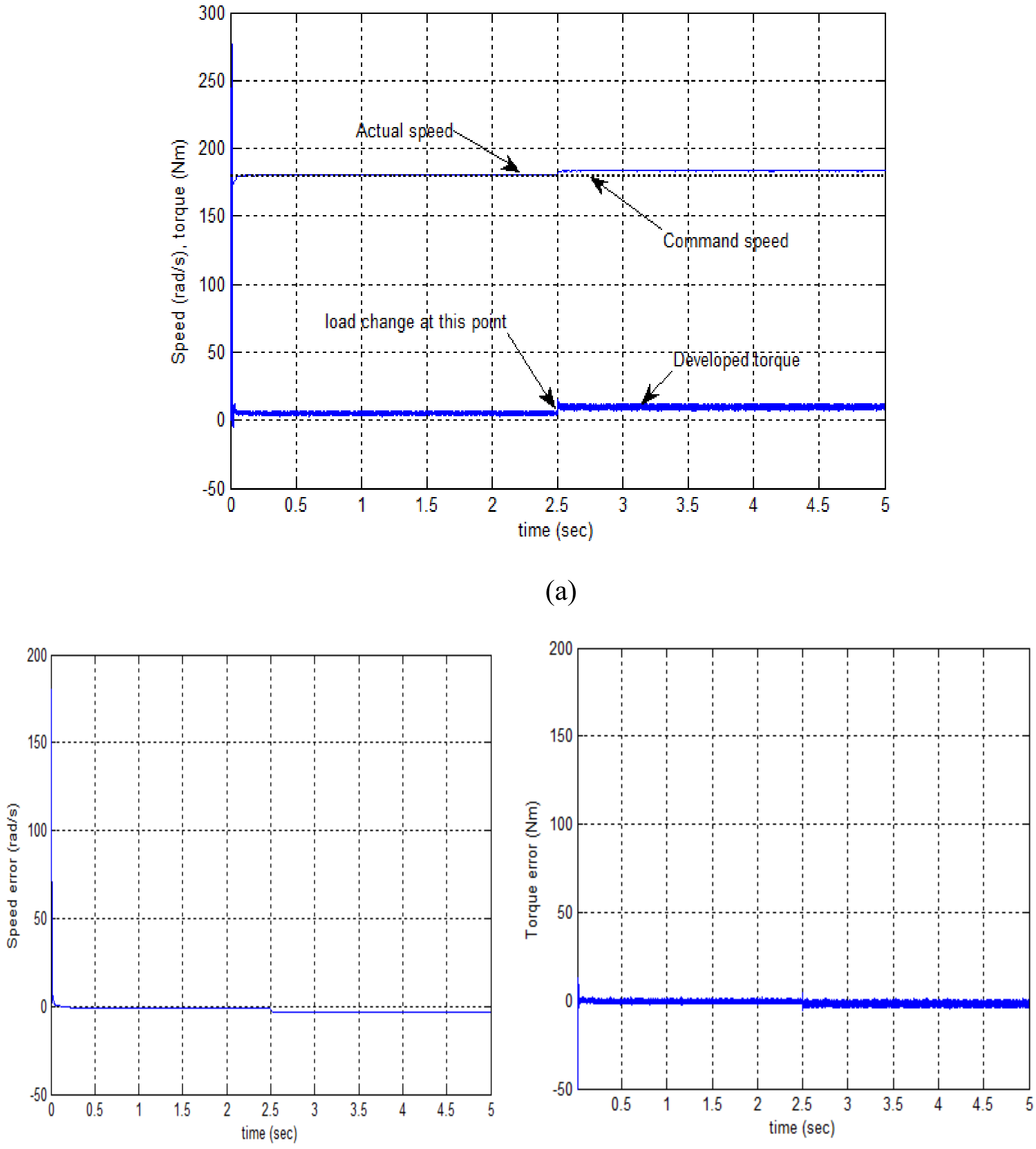

(a)

(b)

(c)

Fig.6.6: Simulated response of the proposed backstepping based nonlinear controller for a step increase of load from 25% rated load to 50% rated load at rated speed: a) speed and torque; b) speed error; c) torque error.

The d and q axis current converge to new value with the change of load so that the motor actual speed follows the reference speed. It is seen from Fig. 6.7 (a) that, for the change of load from 25% rated load to 50% rated load, d axis current remains almost constant whereas torque current i_q increases. The corresponding balanced three phase currents of the proposed nonlinear controller based IPMSM drive is shown in Fig 6.7 (b).

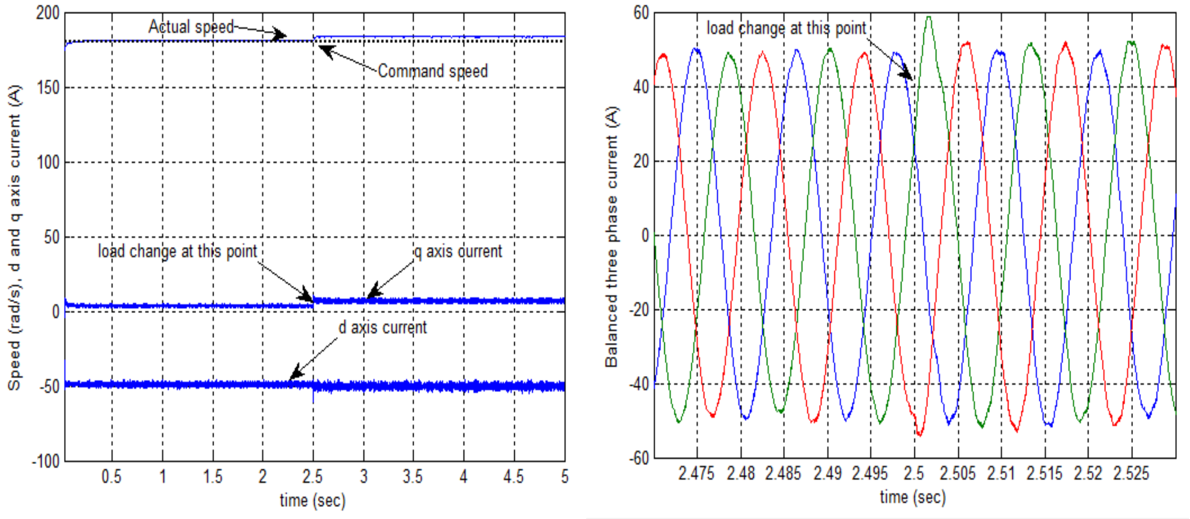

(a) (b)

Fig.6.7: Simulated response of the proposed backstepping based nonlinear controller for a step increase of load from 25% rated load to 50% rated load at rated speed: a) speed, d and q axis current; b) balanced three phase current.

It is an essential property for HPD application to follow the command speed with sudden change of command speed. The responses of the proposed controller for a step change of command speed from 183 rad/s to 260 rad/s with load of 13 Nm at is shown in Figs. 6.8. The speed is changed at t=2.5 sec. It is seen from Fig. 6.8 (a), IPMSM drive can follow the command speed with zero steady state error. The corresponding torque error in shown in Fig. 6.8 (b). Developed torque response shows that, it has lower torque ripples in steady state even above the rated speed. The performance of the proposed controller is also tested for sudden change in load at t= 2.5 sec from 50% to 75% rated load at rated speed. It is seen from Fig. 6.9 that the proposed drive can follow the command speed while maintain lowest torque ripples.

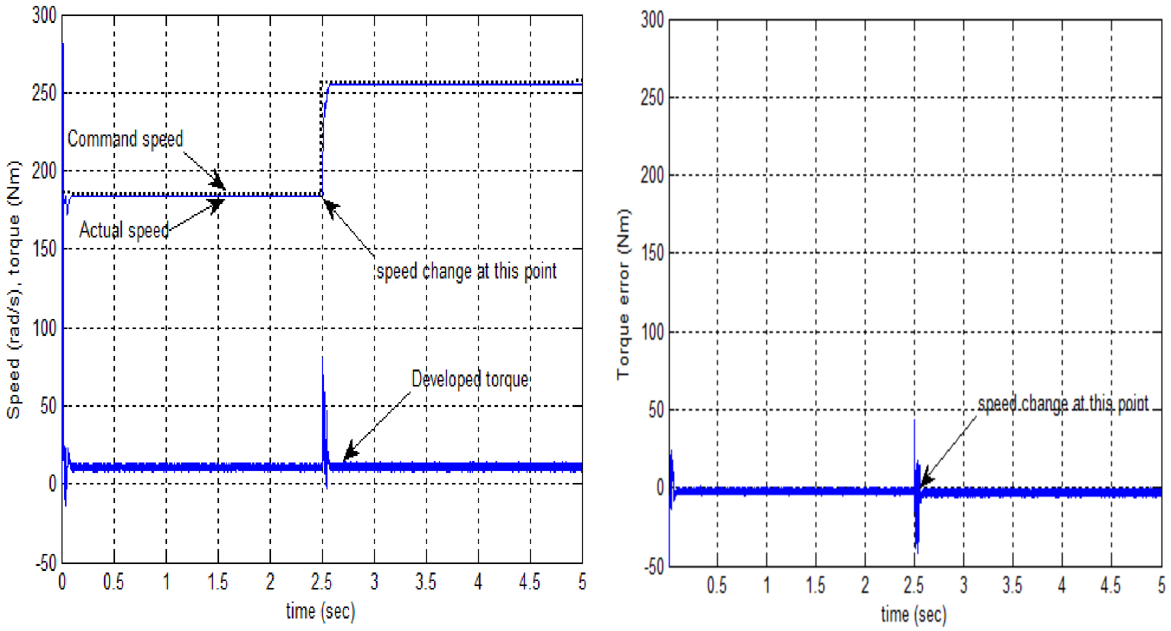

(a) (b)

Fig.6.8: Simulated response of the proposed backstepping based nonlinear controller for a step increase of command speed from 183 rad/s to 260 rad/s with 13 Nm of load: a) speed and torque.

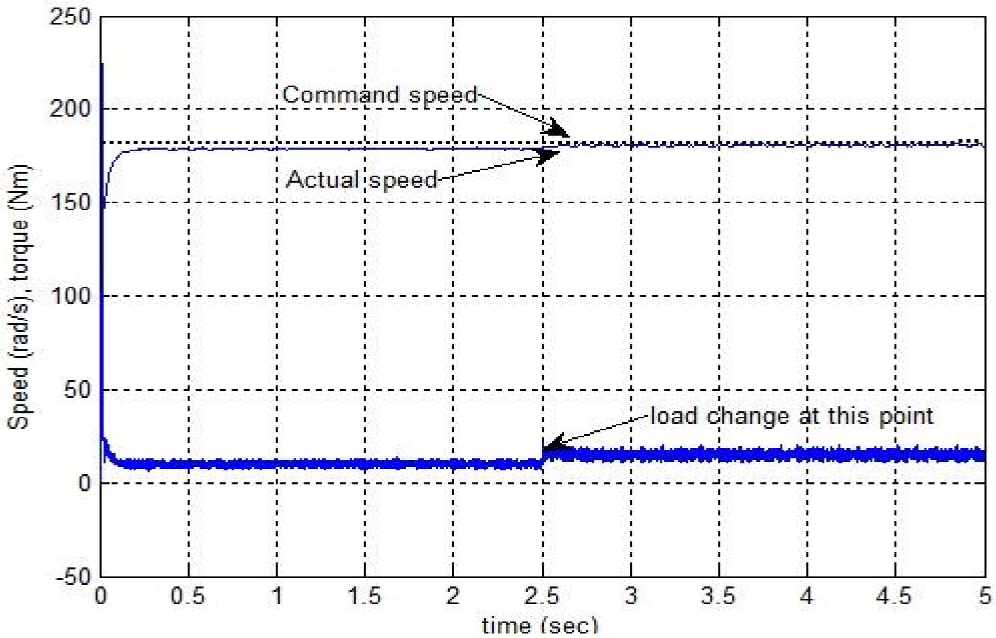

Fig.6: 9: Simulated speed and developed torque response of the proposed backstepping based nonlinear controller for a step increase of load from 50% to 75% rated load and rated speed conditions.

For IPMSM drive, ability to withstand the motor parameter variations is important criterion of the control system where the motor parameters are affected by saturation and temperature effects. The change of stator resistance with temperature variation is common. The speed and developed torque responses at rated speed and 25% rated load are shown in Fig. 6.10 (a), where stator resistance is increased by 25%. The similar responses are shown for rated speed and 50% rated load conditions in Fig. 6.10 (b). In both cases it is shown that the drive maintains lower torque ripples at steady state and follows the command speed with zero steady state error even after a change of armature resistance at different loading conditions.

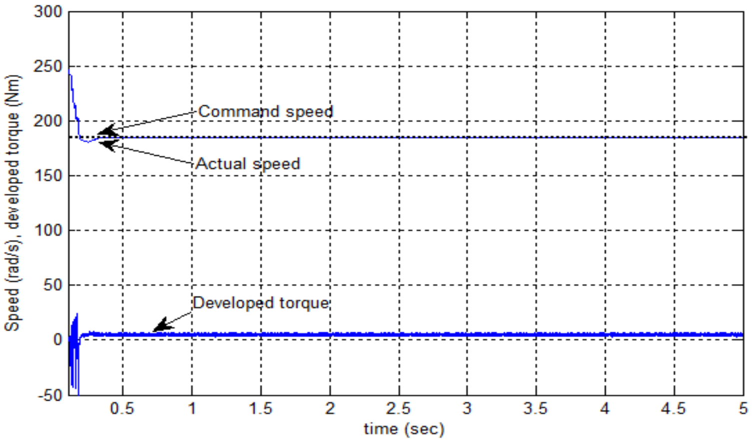

(a)

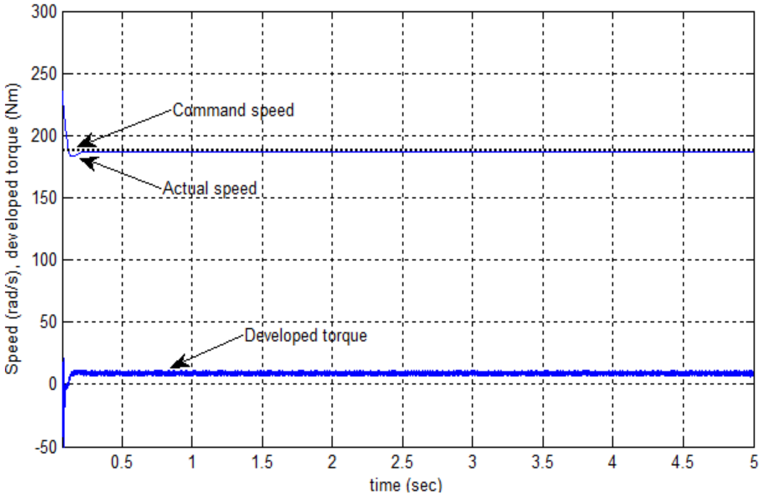

(b)

Fig.6.10: Simulated speed and developed torque responses of the proposed nonlinear controller with change in stator resistance, R_s→1.25 R_s: (a) rated speed and 25% rated load; (b) rated speed and 50% rated load conditions.

The inertia of the motor may change at different operating conditions so it is important to investigate the dynamic performance of the drive with increased inertia. Fig. 6.11 (a) shows the speed and developed torque responses with 25% increased inertia at rated speed and 25% rated load conditions. The similar responses at 50% rated load condition are shown in Fig. 6.11 (b). The results show that the drive follows the rated command speed smoothly without overshoot or undershoot even with increased inertia. The torque ripples are confined to small bandwidth at steady state for the increased inertia.

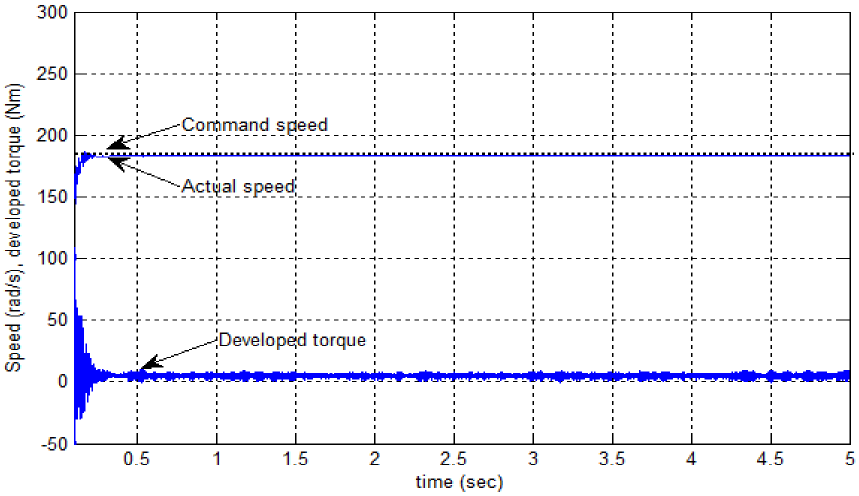

(a)

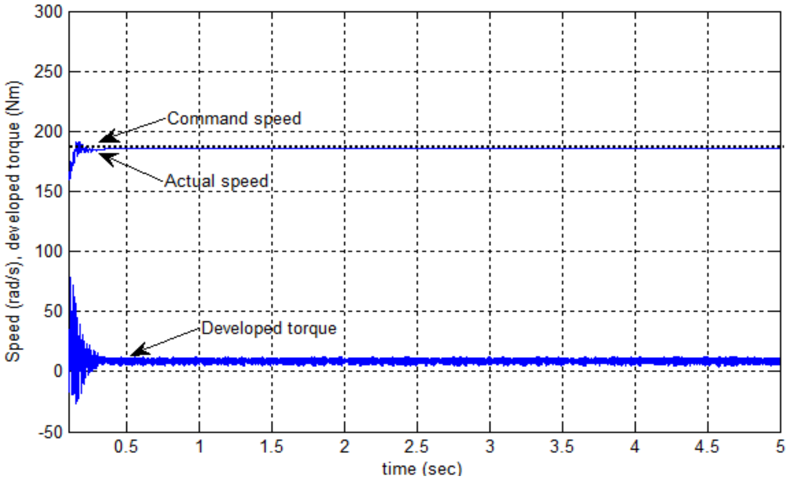

(b)

Fig.6.11: Simulated speed and developed torque responses of the proposed nonlinear controller with change in rotor inertia, $J \rightarrow 1.25\,J$: (a) rated speed and 25% rated load; (b) rated speed and 50% rated load conditions.

The q axis inductance L_q varies significantly with magnetic saturations. As the d axis inductance L_d is not affected by the magnetic saturation therefore parameter L_d is assumed constant and the effect of variation of L_d is not investigated. The speed and developed torque responses are shown in Fig. 6.12 (a) for the proposed nonlinear controller with torque as virtual variable, where L_q is increased by 25% under rated speed and 25% rated load conditions. The similar responses at 50% rated load conditions are shown in Fig. 6.12 (b). It is shown that the proposed backstepping based nonlinear controller is capable of handling the variations of inductance parameters while maintaining reduced torque ripples at steady state at both 25% and 50% rated load conditions.

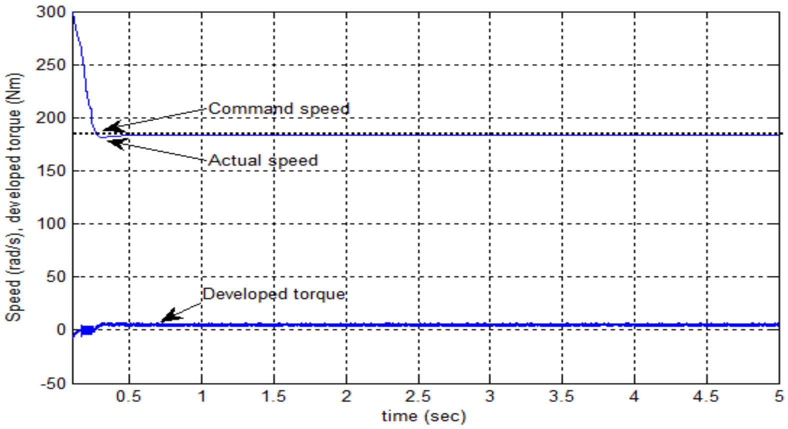

(a)

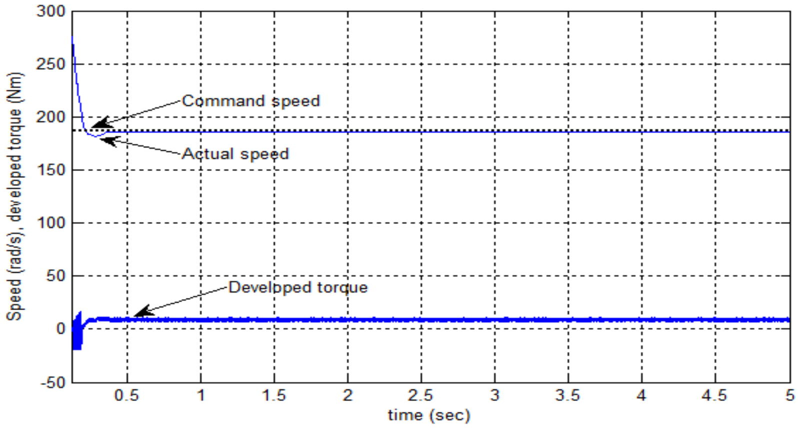

(b)

Fig.6.12: Simulated speed and developed torque responses of the proposed nonlinear controller with change in q axis inductance, $L_q \rightarrow 1.25\ L_q$: (a) rated speed and 25% rated load; (b) rated speed and 50% rated load conditions.

Fig. 6.13 (a) and (b) show the speed and developed torque responses of the proposed nonlinear controller at rated speed under 25% and 50% rated load, respectively with increased inertia constant ($B_m \rightarrow 1.25B_m$). It is evident from the Fig. 6.13 that the proposed nonlinear controller maintain reduced torque ripples at steady state with increased friction constant and IPMSM drive follow the command speed smoothly.

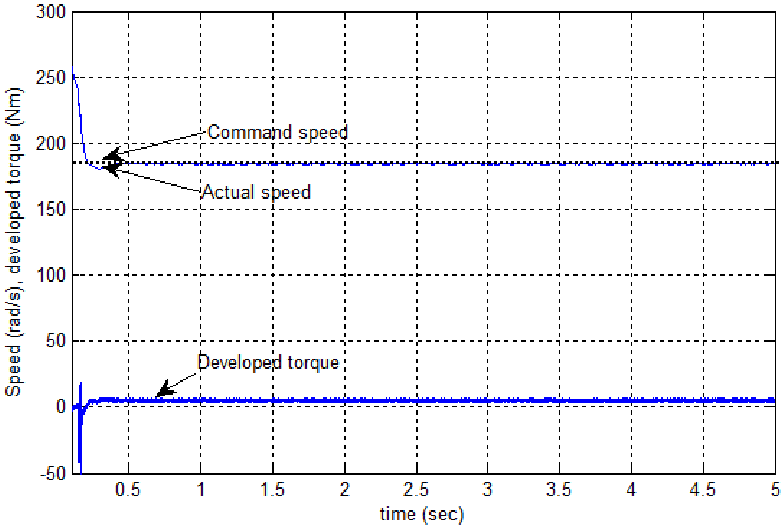

(a)

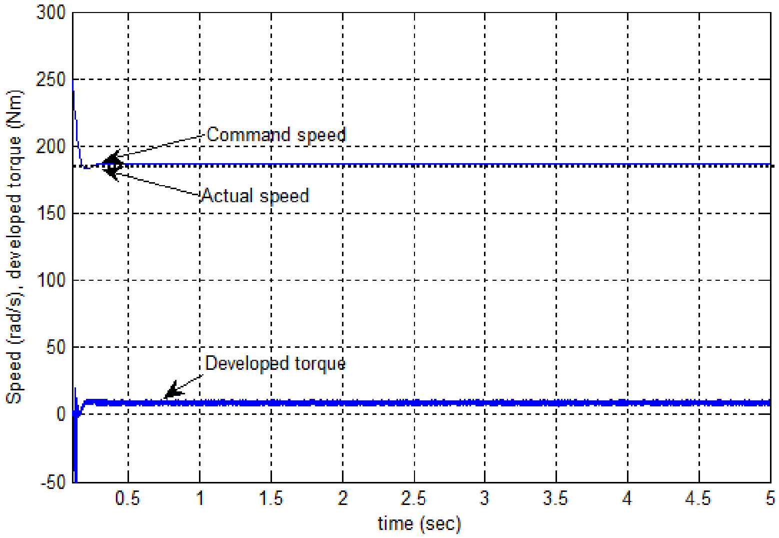

(b)

Fig.6.13: Simulated speed and developed torque responses of the proposed nonlinear controller with change in friction constant, $B_m \rightarrow 1.25\ B_m$: (a) rated speed and 25% rated load; (b) rated speed and 50% rated load conditions.

6.5 Experimental Results of Proposed Controller with Torque as Control Variable

Experimental test were done to verify the effectiveness of the proposed controller for dynamic performance improvement of IPMSM drive at different operating conditions. The closed loop gains of the controller are chosen as k_ω= 50 and k_T= 503 by trial and error method in order to get minimum overshoot and high dynamic performance. The experimental starting speed response for step change of command speed from 0 to 60 rad/s at no load of the proposed backstepping based nonlinear controller of IPMSM drive is shown in Fig. 6.14. It shows that it can follow the command speed smoothly without overshoot/undershoot. For the sake of safe operation, the voltage is applied to the inverter through variac and rectifier arrangement as quickly as possible. The performance for a step change of command speed is also investigated for sudden change of speed from 75 rad/s to 183 rad/s at 25% rated load. From Fig. 6.15 it is seen that, the motor can follow the command speed smoothly for a step increase of speed. The drive converges to its command speed quickly without any overshoot or undershoots at light load condition.

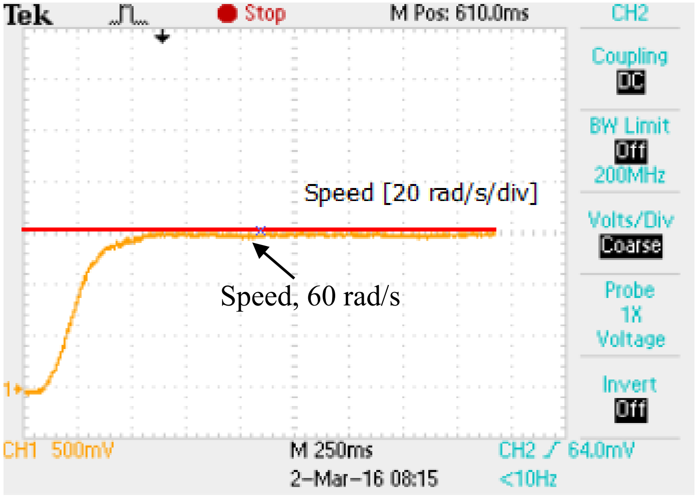

Fig. 6.14: Experimental starting speed response for a step change of command speed (0 to 60 rad/s).

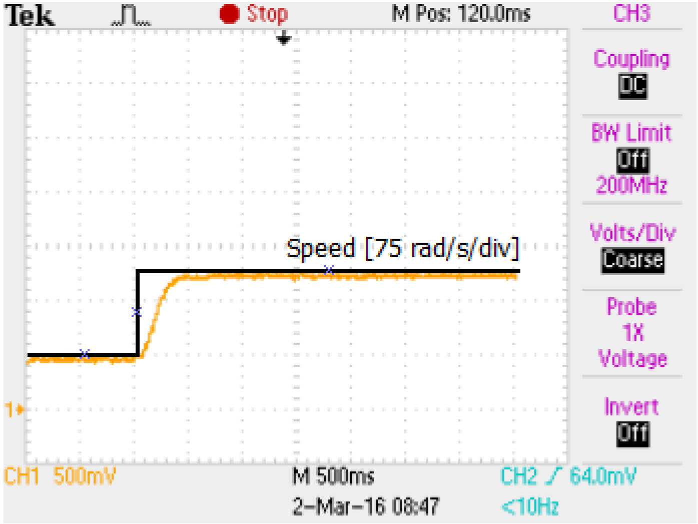

Fig. 6.15: Experimental speed response of the proposed nonlinear controller for step increase in command speed from 75 rad/s to 183 rad/s at 25% rated load.

The experimental speed and torque response at different operating conditions are also investigated. It is found that, the speed follows the command speed of 100 rad/s at 25% rated load. Additionally, the torque ripples have been significantly reduced both in transient and steady state conditions which verifies the simulation environment also is shown in Fig. 6.16.

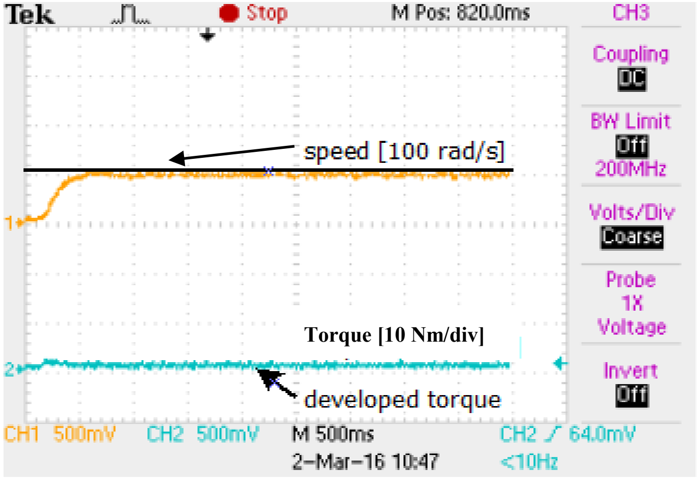

Fig. 6.16: Experimental speed and torque response of the proposed nonlinear controller for a step change of command speed from 0 to 100 rad/s and 25% rated load.

The dynamic performance of the proposed controller is also investigated for a sudden step decrease of command speed. Fig. 6.17 shows the experimental speed and torque response of the proposed nonlinear controller for a step decrease of command speed from 100 to 50 rad/s at 10% rated load. It is clearly seen from the figure that at starting there is some torque ripples but at steady state condition it is almost ripple free which ensures the robustness of the controller for dynamic performance improvement. The experimental torque and speed response of the proposed controller for a step increase of command speed from 50 to 100 rad/s and step decrease of command speed from 100 rad/s to 50 rad/s at 25% rated load is shown in Fig. 6.18. It is shown that, torque ripples are confined to low bandwidth for the step increase and decrease of speed.

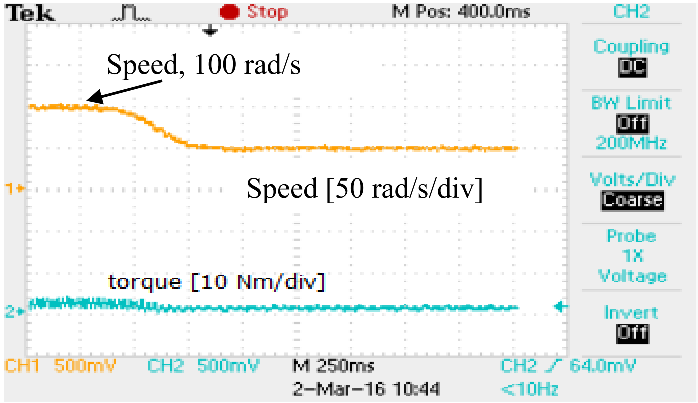

Fig. 6.17: Experimental speed and torque response of the proposed nonlinear controller for a step decrease of command speed from 100 rad/s to 50 rad/s at 10% rated load.

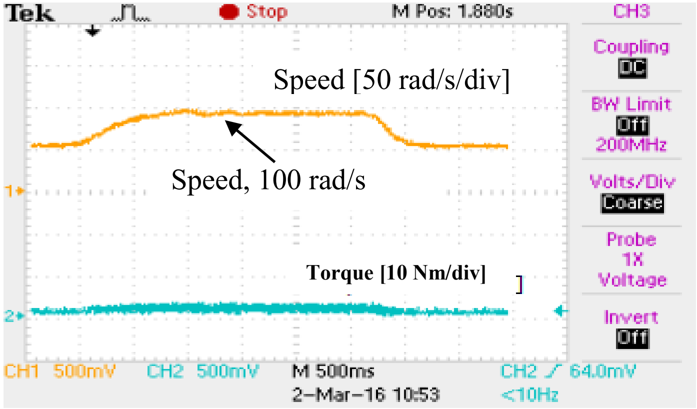

Fig. 6.18: Experimental speed and torque response of the proposed nonlinear controller for step increase and decrease of command speed at 25% rated load.

The steady state speed and torque response for a command speed of 100 rad/s at 60% rated load is shown in Fig. 6.19. It is seen that, real time steady state toque response is almost ripple free. Finally, to verify that the phase currents are balanced, Fig. 6.20 shows the phase currents under 50% rated load at a low speed to validate the assumption made for controller design. This validation is essential to confirm that the phase currents are indeed separated by ~120 degrees with closely matching magnitudes. In summary, the phase currents shown in Fig. 6.20 provide confirmation of this balanced status, and thus ensure that all assumptions made for reference frame transformation are corroborated experimentally.

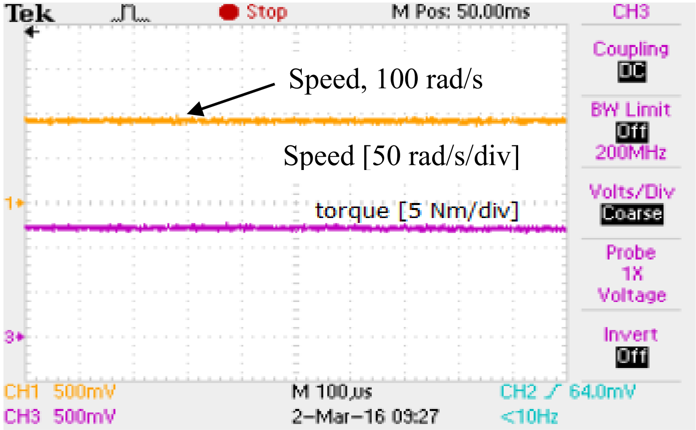

Fig. 6.19: Experimental steady state speed and torque response at 100 rad/s and 60% rated load.

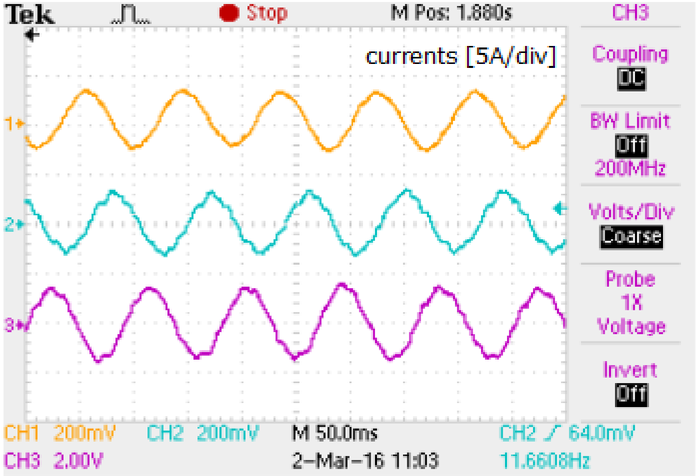

Fig. 6.20: Balanced phase currents of the proposed backstepping based nonlinear controller.

6.6 Nonlinear Controller with both Torque and Flux as Virtual Control Variable

As DTFC utilizes both motor electromagnetic developed torque and stator air-gap flux linkage as control variable therefore this thesis further attempts to design a backstepping based nonlinear controller considering both torque and flux as virtual control variable. In the controller development, speed, torque and flux linkages error variables are stabilized by selecting proper control inputs. These inputs are determined from Lyapunov's stability analysis. Starting with the basis of control, where the error between the reference speed and the actual speed is forced to zero. For the speed error dynamics the stability equation remains same as shown from equation 6.1 to 6.10. The block diagram of the proposed nonlinear controller scheme is shown in Fig. 6.21.

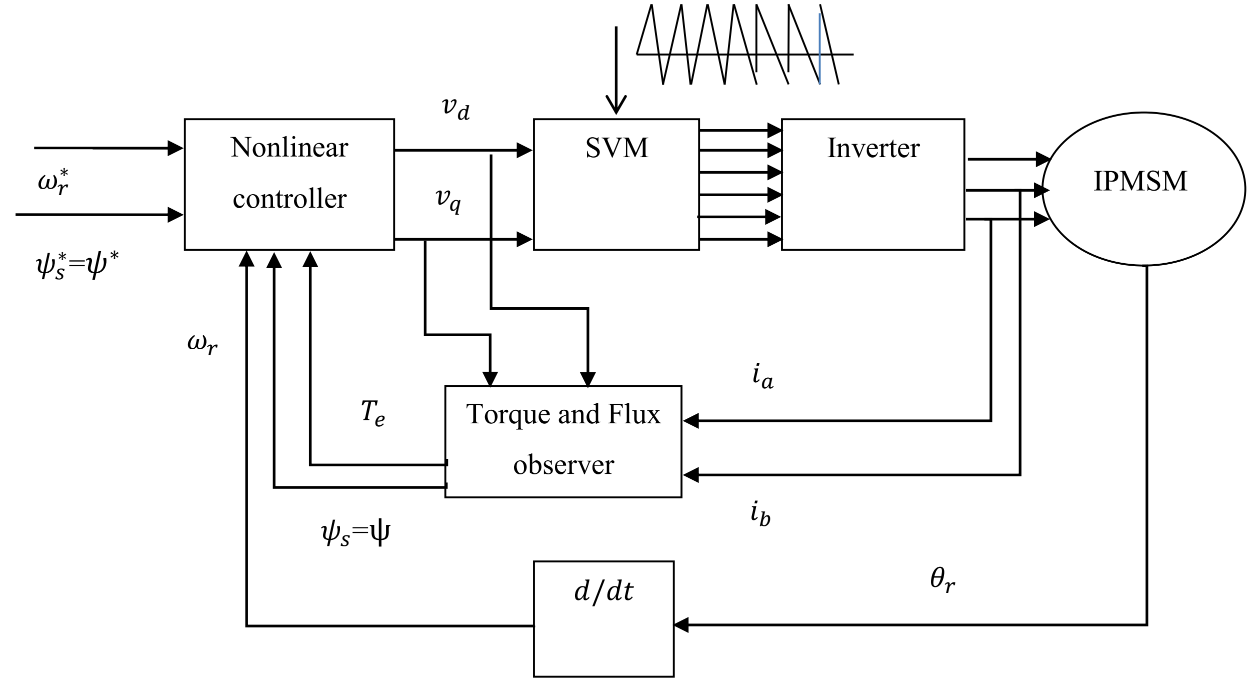

Fig. 6.21: Block diagram of backstepping based nonlinear controller with torque and flux as control variables.

Command electromagnetic developed torque and stator air-gap flux linkage can be chosen as,

$$T_e^*=B_m\omega_r+T_L+k_\omega J e_\omega \text{ and } \psi^*=\psi_{ref} \tag{6.25}$$

Electromagnetic torque error and flux linkage error are given by,

$$e_T = T_e^* \text{ -} T_e \tag{6.26}$$

$$e_\psi = \psi^* \text{ -} \psi \tag{6.27}$$

For stabilizing the electromagnetic torque and stator flux linkage, the derivative of torque and flux error can be defined as,

$$\dot{e_T} = \dot{T_e^*} - \dot{T_e} \tag{6.28}$$

$$\dot{e_\psi} = \dot{\psi}^* - \dot{\psi} \tag{6.29}$$

The derivative of reference electromagnetic torque can be found from (6.15) as,

$$\dot{T_e^*} = \frac{(B_m - k_\omega J)}{J}(T_e \text{-} T_L \text{-} B_m \omega_r) \tag{6.30}$$

The derivative of actual electromagnetic torque can be found from (6.16) as,

$$\dot{T_e} = \frac{3}{2} P[\psi_d \frac{d}{dt}(i_q) + \dot{\psi_d} i_q \text{-} \psi_q \frac{d}{dt}(i_d) \text{-} \dot{\psi_q} i_d] \tag{6.31}$$

The derivative of torque error dynamics can be found from (6.17) as,

$$\dot{e_T} = \frac{(B_m - k_\omega J)}{J}(T_e \text{-} T_L \text{-} B_m \omega_r) - \frac{3}{2} P \psi_d [\frac{1}{L_q}(\text{-}R_s i_q \text{-} P\omega_r L_d i_d \text{-} P\omega_r \psi_m)] + \frac{3}{2} P(i_d - \frac{\psi_d}{L_q}) v_q$$

$$+ \frac{3}{2} P \psi_q [\frac{1}{L_d}(\text{-}R_s i_d + P\omega_r L_q i_q)] \text{-} \frac{3}{2} P(i_q - \frac{\psi_q}{L_d}) v_d \tag{6.32}$$

Similarly, stator flux linkage error dynamic can be defined as,

$$\begin{aligned} \dot{e_\psi} = \dot{\psi}^* - \dot{\psi} &= \text{-}[2\psi_d \dot{\psi_d} + 2\psi_q \dot{\psi_q}] \\ &= \text{-}2\psi_d (v_d \text{-} R_s i_d) \text{ -}2\psi_q (v_q \text{-} R_s i_q) \\ &= 2\psi_d R_s i_d + 2\psi_q R_s i_q \text{-} 2\psi_d v_d \text{-} 2\psi_q v_q \end{aligned} \tag{6.33}$$

Based on the error dynamics, new Lyapunov's function including the motor electromagnetic developed torque and stator air-gap flux linkage variables can be defined as,

$$V_1 = \frac{1}{2}\left(e_\omega^2 + e_T^2 + e_\psi^2\right) \tag{6.34}$$

Differentiating the Lyapunov's function in (6.34) yields,

$$\dot{V}_1 = e_\omega \dot{e_\omega} + e_T \dot{e_T} + e_\psi \dot{e_\psi} \tag{6.35}$$

Substituting the error dynamics from (6.12), (6.32-6.33) in (6.35) yields,

$$\dot{V}_1 = -k_\omega e_\omega^2 + e_T \left\{ \frac{(B_m - k_\omega J)}{J}(T_e - T_L - B_m\omega_r) - \frac{3}{2}P\psi_d \left[\frac{1}{L_q}\left(-R_s i_q - P\omega_r L_d i_d - P\omega_r \psi_m\right)\right] + \frac{3}{2}P\left(i_d - \frac{\psi_d}{L_q}\right)v_q + \frac{3}{2}P\psi_q \left[\frac{1}{L_d}\left(-R_s i_d + P\omega_r L_q i_q\right)\right] - \frac{3}{2}P\left(i_q - \frac{\psi_q}{L_d}\right)v_d \right\} + e_\psi\left[2\psi_d R_s i_d + 2\psi_q R_s i_q - 2\psi_d v_d - 2\psi_q v_q\right] \tag{6.36}$$

The control d-q voltages are chosen from (6.36) such that Lyapunov's function becomes negative semi-definite.

$$v_d = \frac{1}{\psi_q\left(i_q - \frac{\psi_q}{L_d}\right) + \psi_d\left(i_d - \frac{\psi_d}{L_q}\right)} \left\{ \frac{2\psi_q(B_m - k_\omega J)}{3JP}(T_e - T_L - B_m\omega_r) - \psi_d\psi_q\left[\frac{1}{L_q}\left(-R_s i_q - P\omega_r L_d i_d - P\omega_r\psi_m\right)\right] + \psi_q^2\left[\frac{1}{L_d}\left(-R_s i_d + P\omega_r L_q i_q\right)\right] + \left(i_d - \frac{\psi_d}{L_q}\right)\left[\psi_d R_s i_d + \psi_q R_s i_q + \frac{1}{2}k_\psi e_\psi\right] + \frac{2\psi_q}{3P}k_T e_T \right\} \tag{6.37}$$

$$v_q = \frac{1}{-\left[\psi_q\left(i_q - \frac{\psi_q}{L_d}\right) + \psi_d\left(i_d - \frac{\psi_d}{L_q}\right)\right]} \left\{ \frac{2\psi_d(B_m - k_\omega J)}{3JP}(T_e - T_L - B_m\omega_r) - \psi_d^2\left[\frac{1}{L_q}\left(-R_s i_q - P\omega_r L_d i_d - P\omega_r\psi_m\right)\right] + \psi_d\psi_q\left[\frac{1}{L_d}\left(-R_s i_d + P\omega_r L_q i_q\right)\right] - \left(i_q - \frac{\psi_q}{L_d}\right)\left[\psi_d R_s i_d + \psi_q R_s i_q + \frac{1}{2}k_\psi e_\psi\right] + \frac{2\psi_d}{3P}k_T e_T \right\} \tag{6.38}$$

where, k_ω, k_ψ and k_T are feedback constants.

Substituting the v_d and v_q in equation (6.36) yield,

$$\begin{aligned}
&\dot{V}_1=-k_\omega e_\omega^2+e_T\Bigg\{\frac{(B_m-k_\omega J)}{J}(T_e-T_L-B_m\omega_r)-\frac{3}{2}P\psi_d[\frac{1}{L_q}(-R_si_q-P\omega_rL_di_d-P\omega_r\psi_m)]+\\
&\frac{3}{2}P(i_d-\frac{\psi_d}{L_q})\Bigg[\frac{1}{-[\psi_q\left(i_q-\frac{\psi_q}{L_d}\right)+\psi_d\left(i_d-\frac{\psi_d}{L_q}\right)]}\Bigg\{\frac{2\psi_d(B_m-k_\omega J)}{3JP}(T_e-T_L-B_m\omega_r)-\psi_d^2\Bigg[\frac{1}{L_q}\Big(-R_si_q-\\
&P\omega_rL_di_d-P\omega_r\psi_m\Big)\Bigg]+\psi_d\psi_q\Bigg[\frac{1}{L_d}\Big(-R_si_d+P\omega_rL_qi_q\Big)\Bigg]-\Big(i_q-\frac{\psi_q}{L_d}\Big)\Bigg[\psi_dR_si_d+\psi_qR_si_q+\\
&\frac{1}{2}k_\psi e_\psi\Bigg]+\frac{2\psi_d}{3P}k_Te_T\Bigg\}\Bigg]+\frac{3}{2}P\psi_q\,[\frac{1}{L_d}(-R_si_d+P\omega_rL_qi_q)]-\frac{3}{2}P(i_q-\\
&\frac{\psi_q}{L_d})\Bigg[\frac{1}{\psi_q\left(i_q-\frac{\psi_q}{L_d}\right)+\psi_d\left(i_d-\frac{\psi_d}{L_q}\right)}\Bigg\{\frac{2\psi_q(B_m-k_\omega J)}{3JP}(T_e-T_L-B_m\omega_r)-\psi_d\psi_q\Bigg[\frac{1}{L_q}\Big(-R_si_q-P\omega_rL_di_d-\\
&P\omega_r\psi_m\Big)\Bigg]+\psi_q^2\Bigg[\frac{1}{L_d}\Big(-R_si_d+P\omega_rL_qi_q\Big)\Bigg]+\Bigg(i_d-\frac{\psi_d}{L_q}\Bigg)\Bigg[\psi_dR_si_d+\psi_qR_si_q+\frac{1}{2}k_\psi e_\psi\Bigg]+\\
&\frac{2\psi_q}{3P}k_Te_T\Bigg\}\Bigg]\Bigg\}+e_\psi\Bigg[2\psi_dR_si_d+2\psi_qR_si_q-2\psi_d\Bigg[\frac{1}{\psi_q\left(i_q-\frac{\psi_q}{L_d}\right)+\psi_d\left(i_d-\frac{\psi_d}{L_q}\right)}\Bigg\{\frac{2\psi_q(B_m-k_\omega J)}{3JP}(T_e-T_L-\\
&B_m\omega_r)-\psi_d\psi_q\Bigg[\frac{1}{L_q}\Big(-R_si_q-P\omega_rL_di_d-P\omega_r\psi_m\Big)\Bigg]+\psi_q^2\Bigg[\frac{1}{L_d}\Big(-R_si_d+P\omega_rL_qi_q\Big)\Bigg]+\Bigg(i_d-\\
&\frac{\psi_d}{L_q}\Bigg)\Bigg[\psi_dR_si_d+\psi_qR_si_q+\frac{1}{2}k_\psi e_\psi\Bigg]+\frac{2\psi_q}{3P}k_Te_T\Bigg\}\Bigg]-\\
&2\psi_q\Bigg[\frac{1}{-[\psi_q\left(i_q-\frac{\psi_q}{L_d}\right)+\psi_d\left(i_d-\frac{\psi_d}{L_q}\right)]}\Bigg\{\frac{2\psi_d(B_m-k_\omega J)}{3JP}(T_e-T_L-B_m\omega_r)-\psi_d^2\Bigg[\frac{1}{L_q}\Big(-R_si_q-P\omega_rL_di_d-\\
&P\omega_r\psi_m\Big)\Bigg]+\psi_d\psi_q\Bigg[\frac{1}{L_d}\Big(-R_si_d+P\omega_rL_qi_q\Big)\Bigg]-\Big(i_q-\frac{\psi_q}{L_d}\Big)\Bigg[\psi_dR_si_d+\psi_qR_si_q+\frac{1}{2}k_\psi e_\psi\Bigg]+\\
&\frac{2\psi_d}{3P}k_Te_T\Bigg\}\Bigg]\Bigg]
\end{aligned}\tag{6.39}$$

Equation (6.39) can be simplified in the following form,

$$\dot{V}_1=-k_\omega e_\omega^2-k_Te_T^2-k_\psi e_\psi^2 \tag{6.40}$$

If k_ω, k_T and $k_\psi>0$, then the Lyapunov's function becomes negative semi-definite that guarantees asymptotic stability in the complete system.

6.7 Simulation Results of the Proposed Nonlinear Controller with Torque and Flux as Control Variables

An extensive simulation has been done to predict the performance of the proposed nonlinear controller based IPMSM drive considering motor electromagnetic developed torque and stator air-gap flux linkage as virtual control variable. Sample results are presented below. For the design purpose, motor electromagnetic developed torque and air-gap flux linkage is considered as virtual control variable. The speed, torque and flux errors for the proposed nonlinear controller at rated conditions (183 rad/s and 19 Nm) are shown in Figs. 6.22, respectively. Speed, motor electromagnetic torque and flux errors converge to zero which ensures global stability of the proposed nonlinear controller.

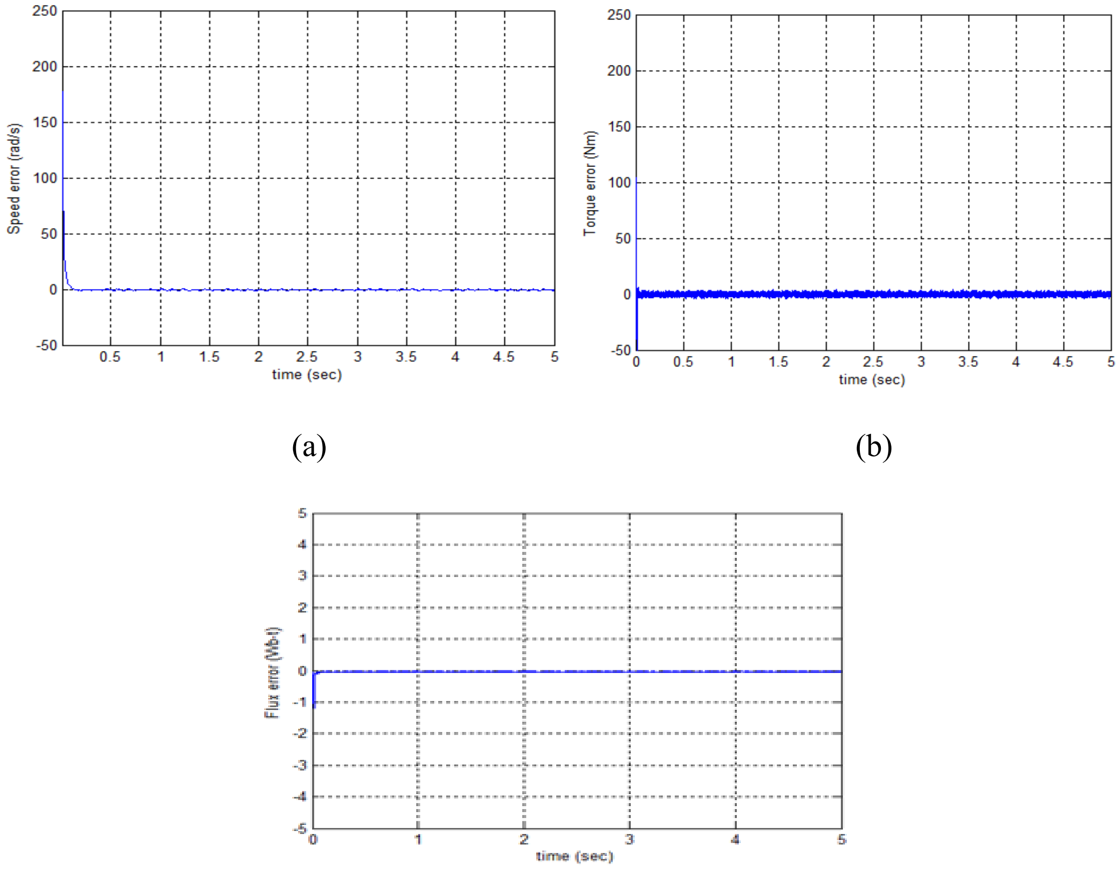

(a) (b)

(c)

Fig.6.22: Simulated response of the proposed nonlinear controller at rated conditions (183 rad/s and 19 Nm): (a) speed error; (b) torque error; (c) flux error.

The speed, developed torque and corresponding d-q axes currents, three phase line current of the proposed nonlinear controller with torque and flux as control variables at rated speed and rated load is shown in Fig. 6.23. The speed of the proposed drive can follow the command speed without any overshoot or undershoot and the settling time is lower. The torque response shows that the developed torque has low torque ripple both in transient and steady state. The speed overshoot problem of previously developed nonlinear controller (Fig.6.2) with torque as virtual control variable is solved by the proposed nonlinear controller.

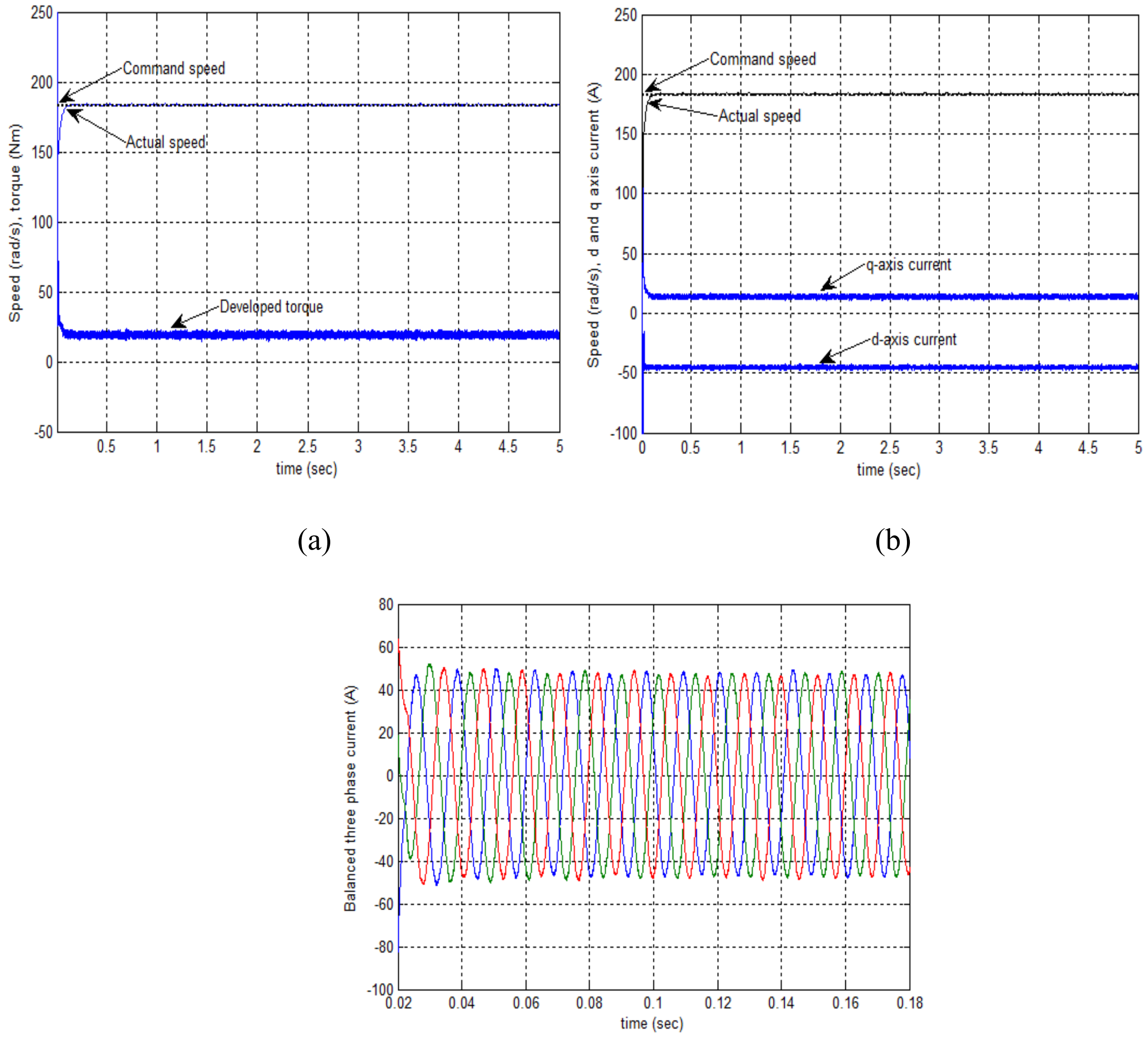

(a) (b)

(c)

Fig.6.23: Simulated response of the proposed nonlinear controller at rated conditions: (a) speed and developed torque; (b) d and q axis current; (c) three phase line current.

The speed, developed torque response and the corresponding speed error, torque error and flux error of the proposed nonlinear controller for step change of command speed from 50 to 183 rad/s at rated load is shown in Figs. 6.24, respectively. The speed can follow the command speed and all the error variables converge to zero which indicate the stability of the drive system at step change of speed with rated load. For the step change of speed, the motor developed torque has lower torque ripples both in transient and steady state with a small peak at the time of speed change.

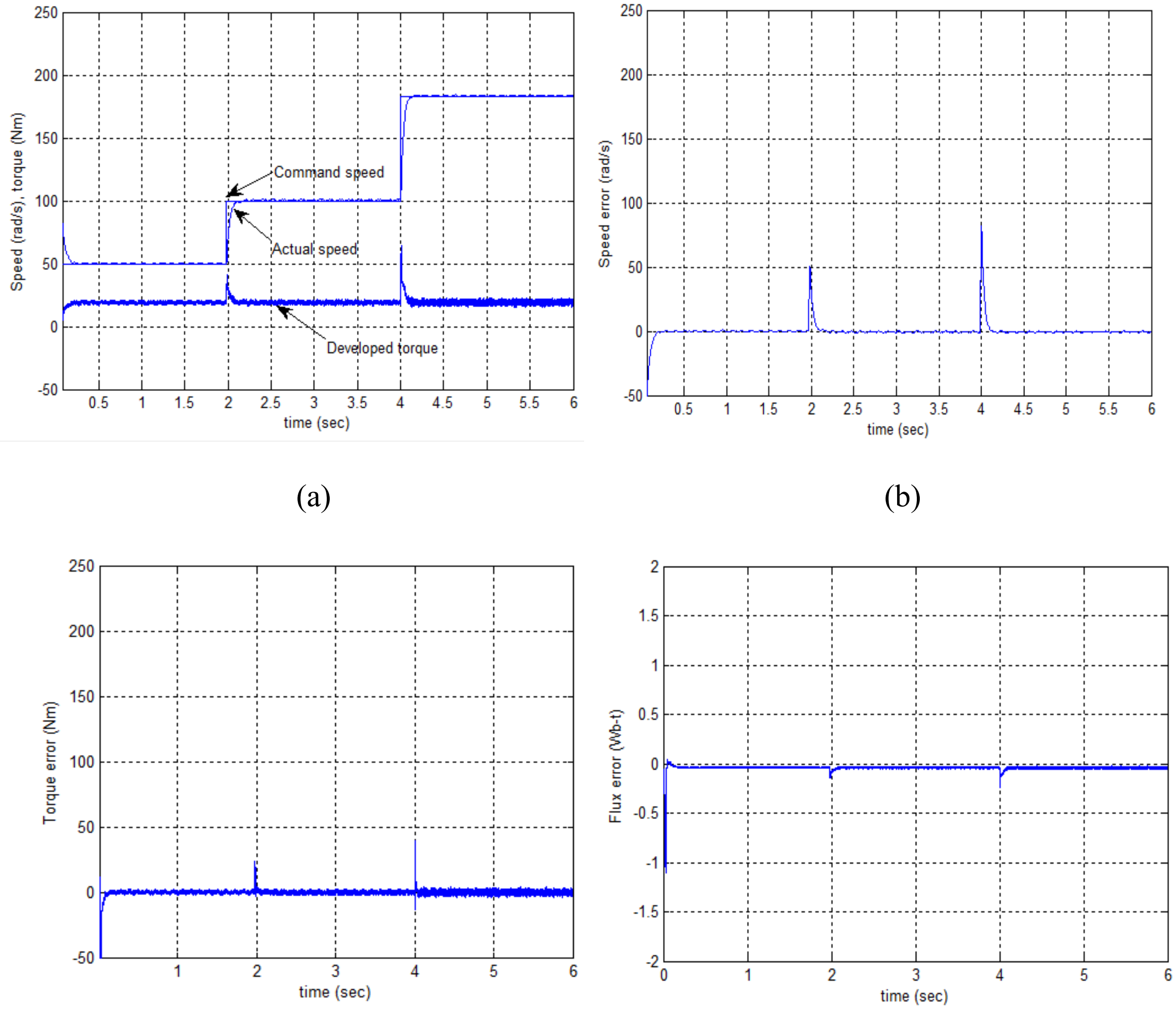

(a)

(b)

(c)

(d)

Fig.6.24: Simulated response of the proposed nonlinear controller at rated load (19 Nm) with step change of command speed from 50 to 183 rad/s: (a) speed and developed torque; (b) speed error; (c) torque error; (d) flux error.

The ability to withstand disturbances is an important feature of the proposed nonlinear controller with torque and flux as control variables. The change of load is a typical external disturbance and also for high performance drive, the load change is a very common situation. The speed, developed torque corresponding speed, torque and flux error responses for the proposed nonlinear controller are shown in Figs. 6.25 (a)-(d), respectively for a sudden increase of load at the rated speed. The motor is started with 75% rated load and at t= 2.5 second, the load is suddenly increased to rated load. It is shown that the proposed torque and flux virtual control variable based nonlinear controller of IPMSM drive is almost insensitive to this step change of load. Although there is a small deviation of speed with change of load but it converges within minimum time to the command speed. The motor developed torque maintains minimum torque ripples at steady state to this step increase of load. The error variables converge to zero which verifies the global stability of the controller for sudden change of load at rated speed. The balanced three phase current response at this condition is shown in Fig. 6.25 (e).

The responses of the IPMSM drive also need to be investigated for sudden change of speed and load. The speed is changed from 100 to 183 rad/s at t= 2 seconds and load is increased from 17 to 19 Nm at t= 3 seconds. The speed, developed torque and corresponding error variables are shown in Figs. 6.26 (a)-(d), respectively. It is clearly seen that, the developed torque has lower torque ripples at steady state which signifies the high dynamic performance of the proposed nonlinear controller for system disturbances and motor actual speed follows the command speed with no steady state error. The corresponding speed, torque and flux errors also converge to zero which signifies the better performance of the proposed nonlinear controller with stability criteria.

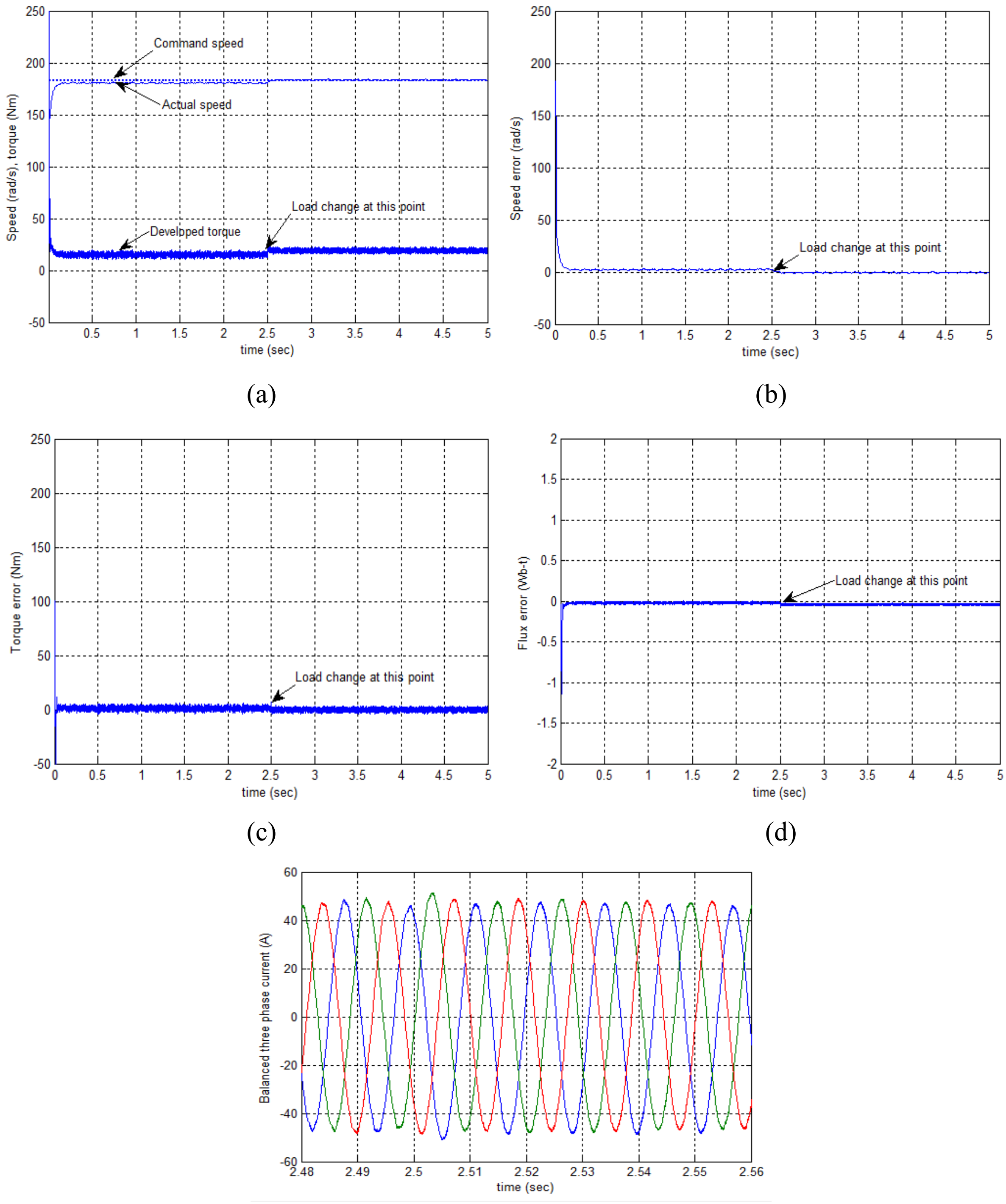

(a)

(b)

(c)

(d)

(e)

Fig.6.25: Simulated response of the proposed nonlinear controller at rated speed with step change of load (15-19 Nm): (a) speed and developed torque; (b) speed error; (c) torque error; (d) flux error; (e) balanced three phase current.

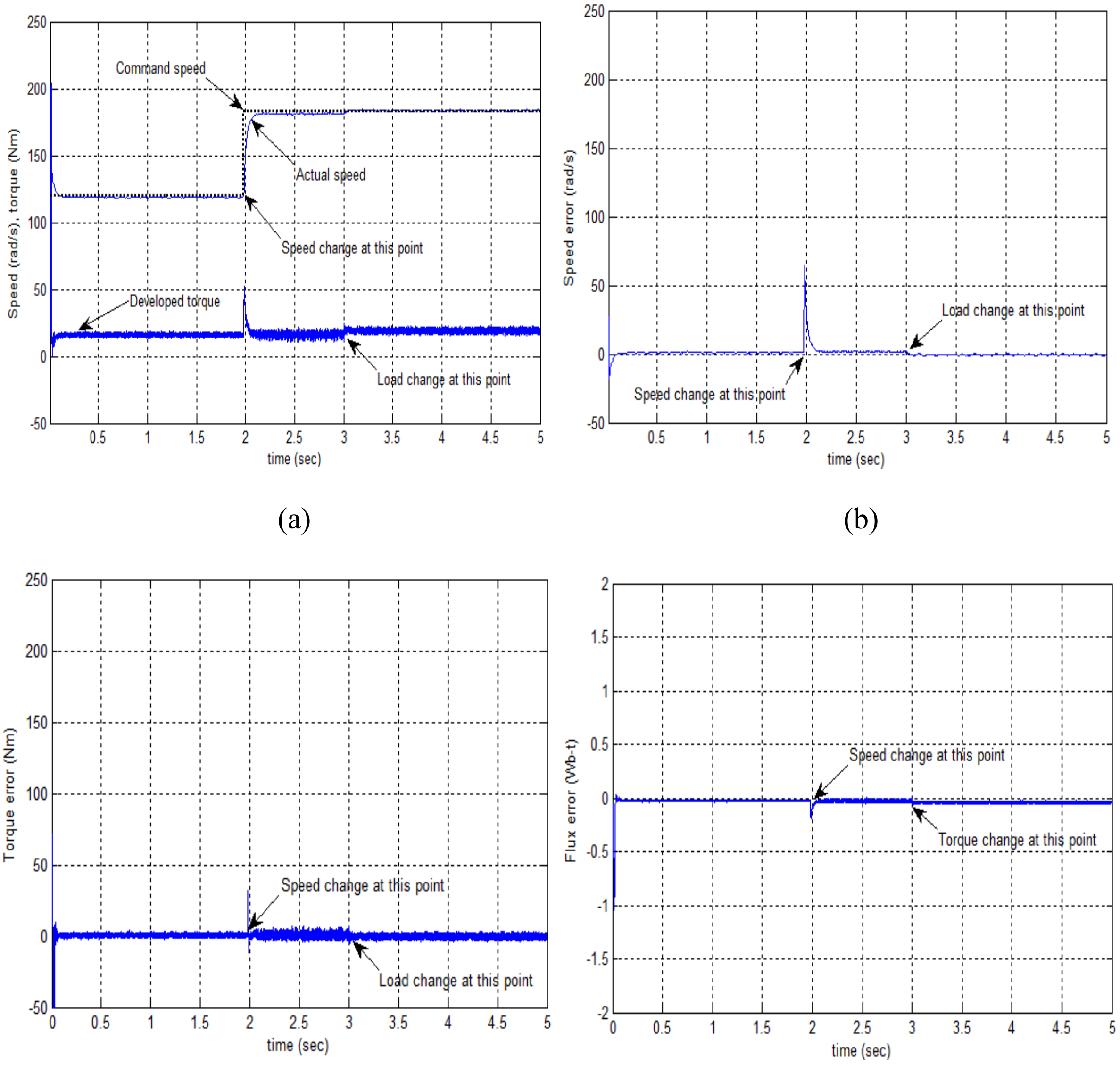

(a)

(b)

(c)

(d)

Fig.6.26: Simulated response of the proposed nonlinear controller at step change of command speed (100-183 rad/s) with step change of load (17-19 Nm): (a) speed and developed torque; (b) speed error; (c) torque error; (d) flux error.

The ability to withstand the motor parameter variations is another important criterion of the control system, particularly for IPMSM drive where the motor parameters are affected by saturation and temperature effects. The change of motor stator resistance with temperature is common phenomenon. The speed and developed torque responses are shown in Fig. 6.27 where the stator resistance is increased by twice, under rated speed with 25% rated load. The similar responses for rated load are shown in Fig. 6.28. In both cases it is shown that the drive follow the command speed with reduced torque ripples at steady state even after a change of armature resistance at different loading conditions.

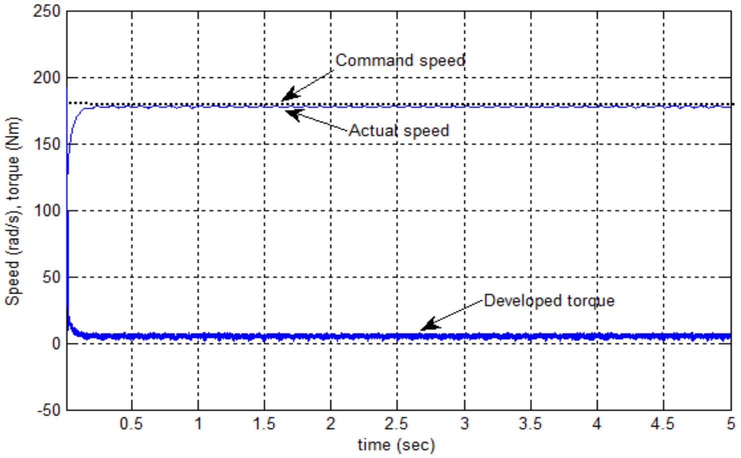

Fig.6.27: Simulated speed and developed torque responses of the proposed nonlinear controller with change in stator resistance $R_s \rightarrow 2R_s$ at 25% rated load and rated speed conditions.

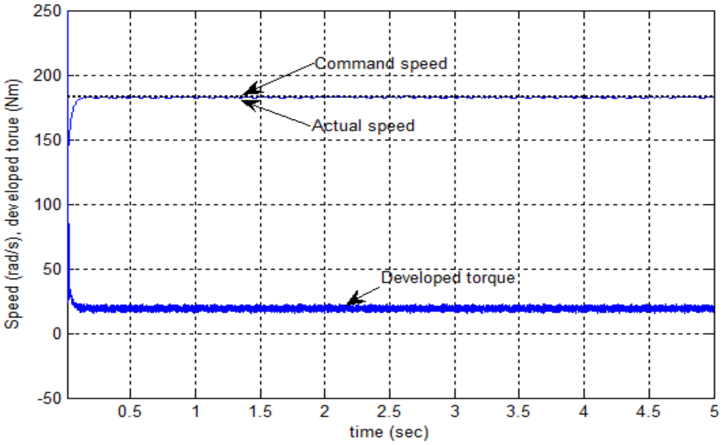

Fig.6.28: Simulated speed and developed torque responses of the proposed nonlinear controller with change in stator resistance $R_s \rightarrow 2R_s$ at rated load and rated speed conditions.

The inertia of the motor may change at different loading conditions, so it is important to investigate the starting performance of the drive with increased inertia. Figs. 6.29 and 6.30 show the speed and developed torque responses of the proposed nonlinear controller with doubled rotor inertia with 25% rated load and rated load, respectively. The results show that the drive follows the rated command speed smoothly even with doubled rotor inertia and motor developed torque has lower ripples remain lower in steady state.

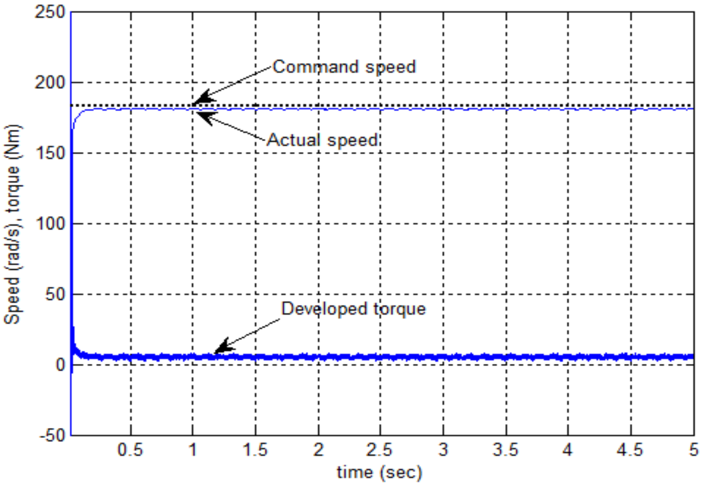

Fig.6.29: Simulated speed and developed torque responses of the proposed nonlinear controller with change in inertia J→2J at 25% rated load and rated speed conditions.

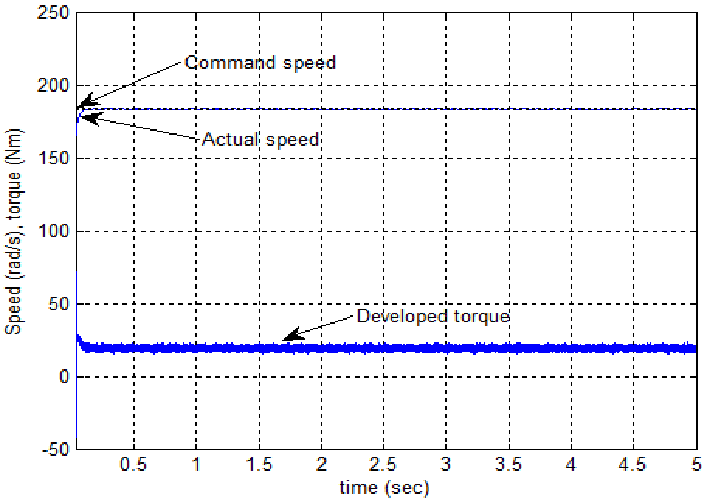

Fig.6.30: Simulated speed and developed torque responses of the proposed nonlinear controller with change in inertia J→2J at rated load and rated speed conditions.

Among the various motor parameters the q-axis inductance parameters L_q is another important parameter as it varies significantly with the magnetic saturation. As direct axis inductance parameter L_d is assumed constant, the effect of variation of L_d is not investigated. The speed and developed torque responses of the proposed nonlinear controller under 25% rated load and rated load at rated speed is shown in Figs. 6.31 and 6.32, respectively with 25% reduced L_q. It is shown that the proposed nonlinear controller is capable of handling the variations of inductance at both low load and rated load conditions while maintain reduced torque ripples which verifies that proposed nonlinear controller improves the dynamic performance of the IPMSM drive system.

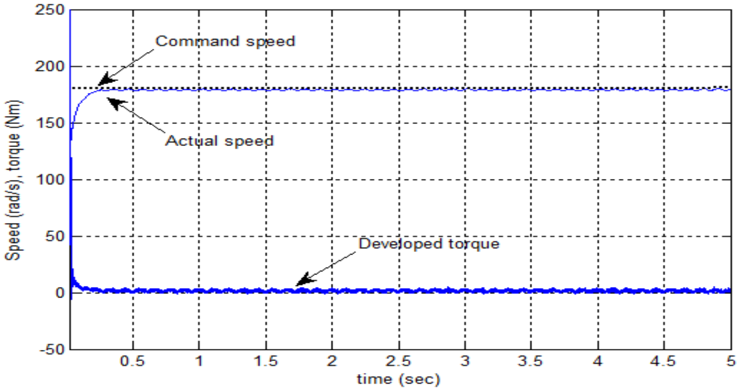

Fig.6.31: Simulated speed and developed torque responses of the proposed nonlinear controller with 25% decrease of L_q at 25% rated load and rated speed conditions.

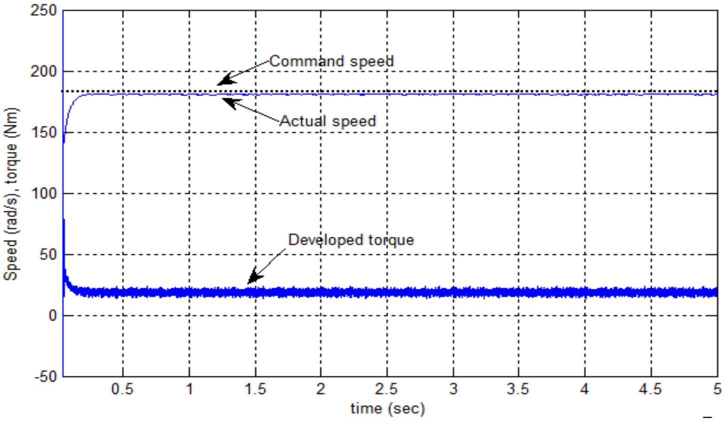

Fig.6.32: Simulated speed and developed torque responses of the proposed nonlinear controller with 25% decrease of L_q at rated load and rated speed conditions.

Figs. 6.33 and 6.34 shows the speed and developed torque response of the proposed nonlinear controller under 25% rated load and rated load condition at rated speed with doubled friction constant ($B_m \rightarrow 2B_m$), respectively. It is clear that, the proposed nonlinear controller maintains reduced torque ripples in steady state with increased friction constant and IPMSM drive follow the command speed with lower settling time without overshoot and no steady state error.

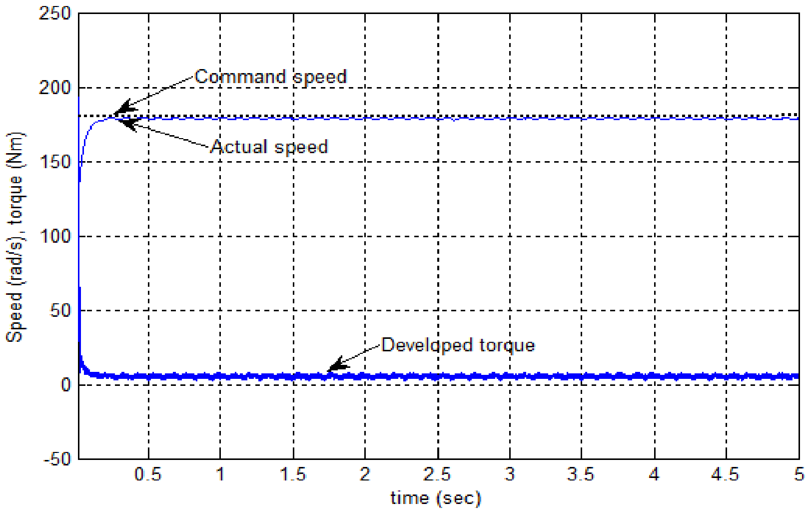

Fig.6.33: Simulated speed and developed torque responses of the proposed nonlinear controller with change in friction constant, $B_m \rightarrow 2B_m$ at 25% rated load and rated speed conditions.

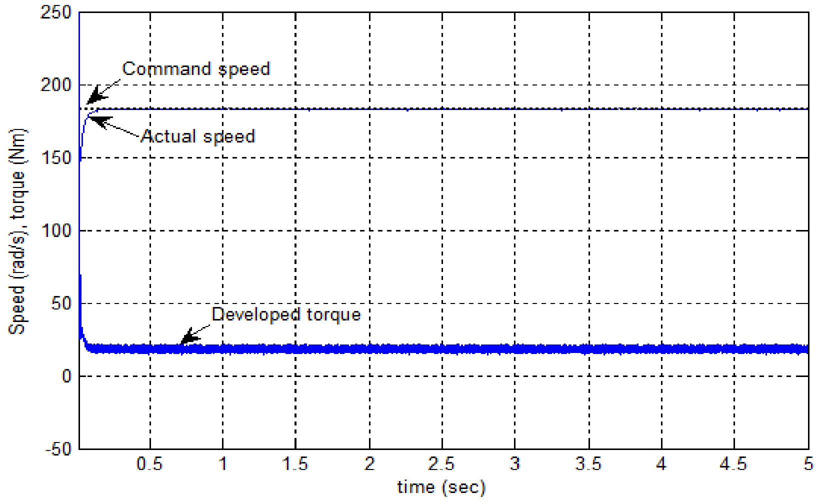

Fig.6.34: Simulated speed and developed torque responses of the proposed nonlinear controller with change in friction constant, $B_m \rightarrow 2B_m$ at rated load and rated speed conditions.

6.8 Experimental Results of the Proposed Nonlinear Controller with Torque and Flux as Control Variables

Numerous experimental tests have been completed to evaluate the performance of the proposed nonlinear controller of IPMSM drive. Some sample results have been presented in this thesis. Experimental results are also carried out for the modified eighteen-sector based DTFC scheme incorporating LMA in order to prove the superiority in terms of dynamic performance improvement of the proposed nonlinear controller. Experimental results are shown in Figs. 6.35 to 6.38. Figs. 6.35 shows the starting response of the proposed controller at no load condition. Fig. 6.35 (a) shows that, motor actual speed follows the command of 50 rad/s smoothly without any overshoots and steady-state error. Moreover, the settling time smaller and hence it is faster. Fig. 6.35 (b) shows that speed follows the command speed of 140 rad/s at no load. Fig. 6.36 shows the speed and developed torque responses of the proposed nonlinear controller at a command speed of 120 rad/s with 10% rated load. It is clearly seen that, at steady state condition, torque is almost ripple free which demonstrates the effectiveness of the proposed nonlinear controller for dynamic performance improvements.

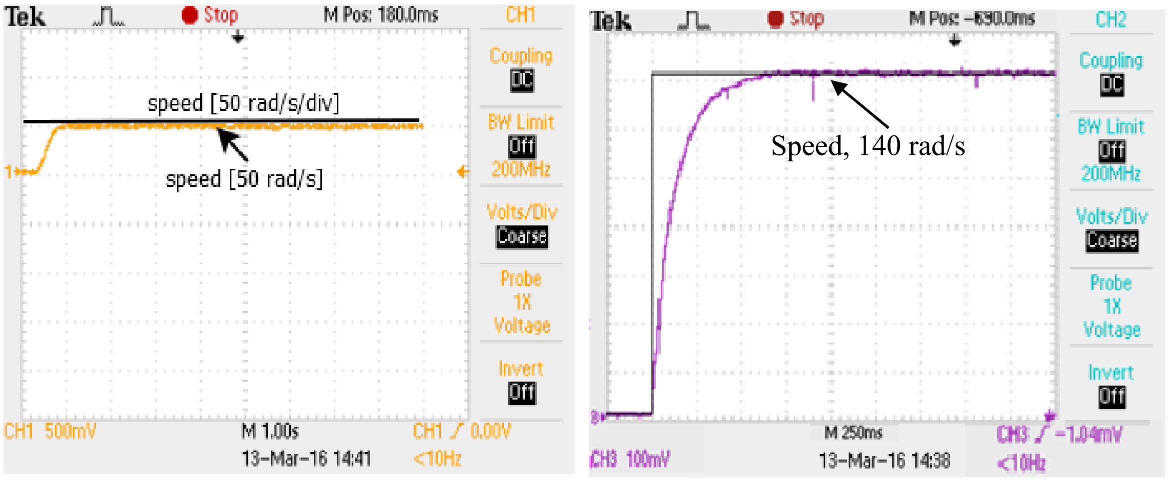

(a) (b)

Fig.6.35: Experimental starting speed response of the proposed nonlinear controller at no load: (a) command speed of 50 rad/s; (b) command speed of 140 rad/s.

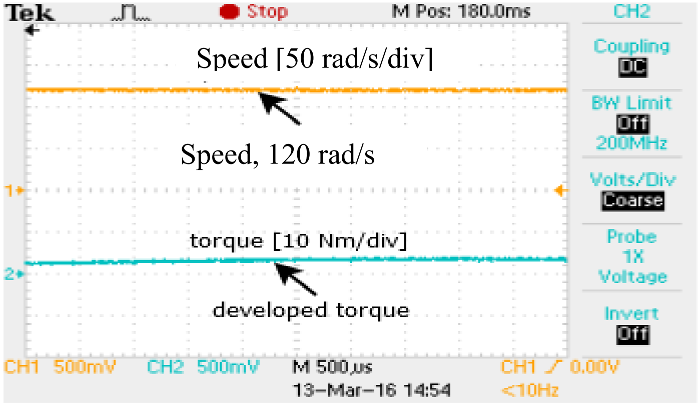

Fig.6.36: Experimental speed and developed torque responses of the proposed nonlinear controller at a command speed of 120 rad/s and 10% rated load.

Figs. 6.37 (a) and (b) show the experimental speed and developed torque responses of the modified eighteen-sector based DTFC scheme incorporating LMA and the proposed nonlinear controller with torque and flux as control variables, respectively, under 50% rated load and a command speed of 100 rad/s conditions. It is shown from Figs. 6.37 (a) and (b) that the modified eighteen-sector based DTFC with LMA has higher torque ripples at steady state, whereas the proposed nonlinear controller based IPMSM drive has lower torque ripples at steady state. Therefore, the proposed nonlinear controller based IPMSM drive is found superior to the eighteen-sector based DTFC with LMA regarding the dynamic performance of the drive.

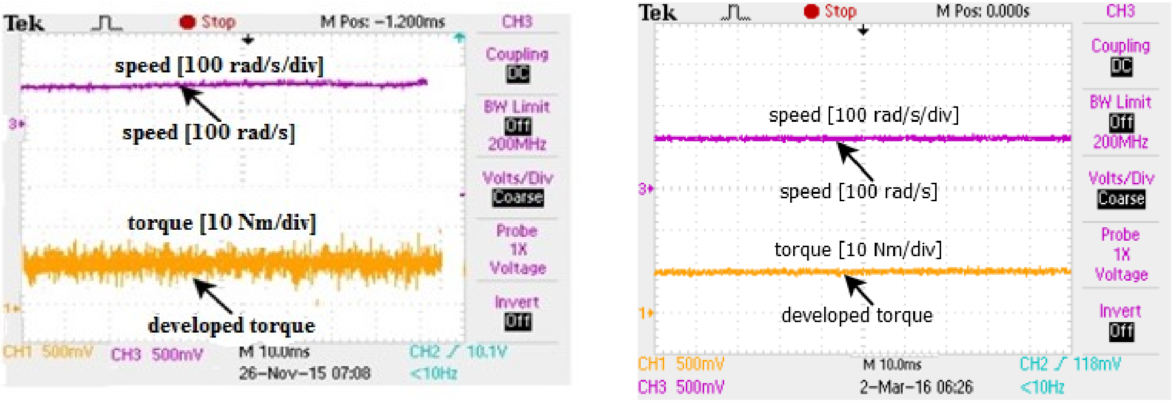

(a) (b)

Fig.6.37: Experimental speed and developed torque responses of the DTFC scheme: (a) eighteen- sector based DTFC with LMA; (b) proposed nonlinear controller.

Figs. 6.38 (a)-(d) show the comparative developed torque analysis of six-sector based DTFC with LMA, eighteen-sectors constant flux based DTFC, eighteen-sector based DTFC with LMA and proposed nonlinear controller based IPMSM drive, respectively at 50% rated load for a command speed of 100 rad/s. It is clearly seen from Figs. 6.38 (a), (b) and (c) that the torque ripples can be minimized by eighteen-sector based DTFC with LMA in compared to six- sector based DTFC with LMA and eighteen-sector constant flux based DTFC. Furthermore, torque ripples can be minimized at steady state by the proposed backstepping based nonlinear controller is shown in Fig. 6.38 (d). Therefore, the dynamic performance improvement by the proposed nonlinear controller scheme has been validated.

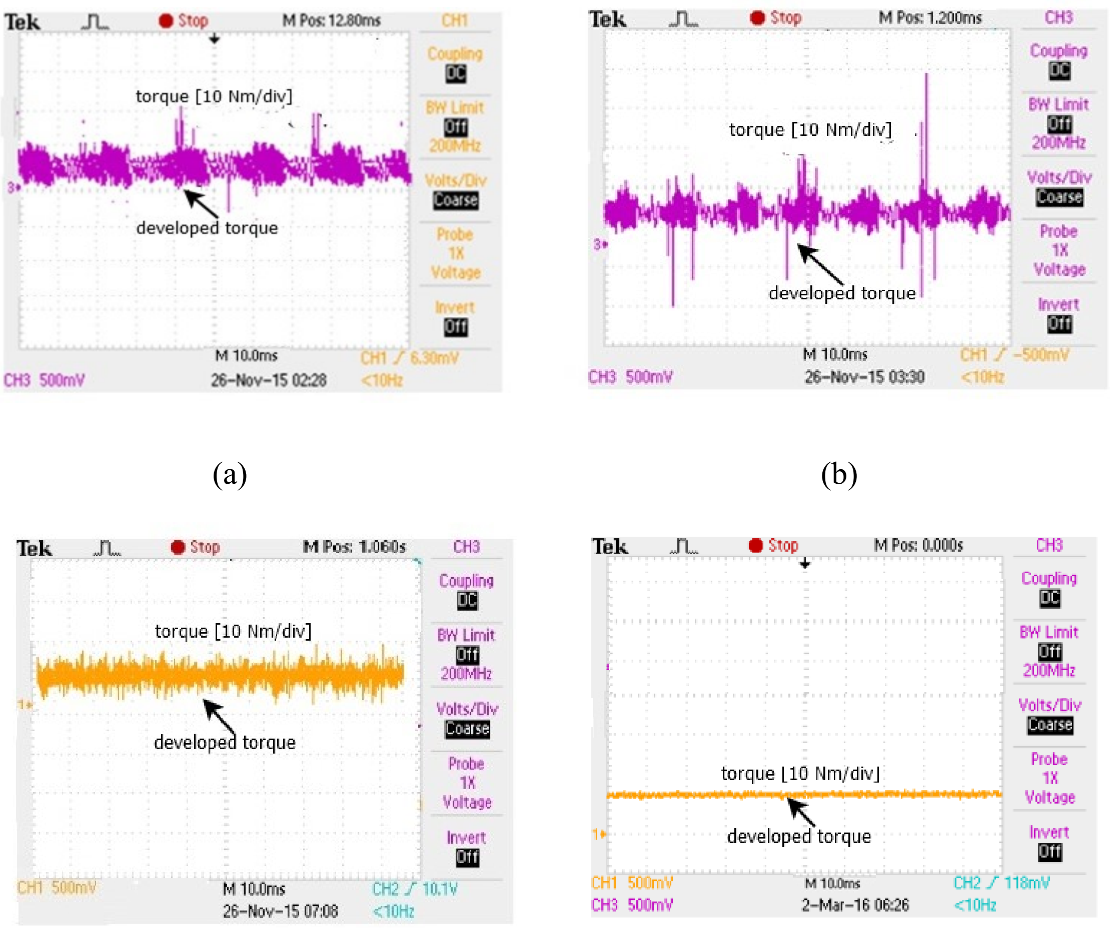

(a) (b)

(c) (d)

Fig.6.38: Experimental developed torque responses of the DTFC scheme: (a) six-sector based DTFC with LMA; (b) eighteen-sector constant flux based DTFC; (c) eighteen-sector based DTFC with LMA; (d) proposed nonlinear controller.

6.9 Conclusion

Initially, a novel backstepping based nonlinear controller is developed considering the motor electromagnetic developed torque as virtual control variable which suffers from speed overshoot problem at the starting and also speed overshoot problem for parameter variations. The developed nonlinear controller with motor electromagnetic developed torque as virtual control variable suffers from torque ripples in the transient conditions. To overcome the drawbacks of the controller, finally a backstepping based nonlinear controller is developed for IPMSM drive considering both motor electromagnetic developed torque and stator air-gap flux linkage as virtual control variables. The simulation results of the both nonlinear controller show encouraging performances of the proposed drive. The proposed nonlinear controller based IPMSM drive maintain the lowest torque ripples among all the DTFC scheme developed in this thesis. Therefore, proposed nonlinear controller based IPMSM drive could be a potential candidate for high performance industrial IPMSM drive.

Chapter 7

Conclusion

Based on the literature review in Chapter 1, it is concluded that the interior permanent magnet synchronous motor (IPMSM) drive can be used to meet the criteria of variable speed high performance electric motor drives. Therefore, this thesis was initiated on the basis of need for dynamic performance improvement while maintaining high efficiency and further analysis of past work performed in the area of permanent magnet synchronous machine (PMSM) dynamic performance improvement strategy. However, the system dynamic performance depends on the inverter control strategy mainly how the control variables in DTFC (electromagnetic torque and stator flux linkage) are controlled. Despite lot of research in the area of DTFC but still suffers from torque ripple. Thus, this thesis developed several control techniques for DTFC to reduce the torque ripple while maintaining high efficiency.

In Chapter 1, review of various electric motors has been provided which identifies the problems in the control and improvement of dynamic performance for the high performance drives. Conventional PI controller is used for the direct torque and flux control (DTFC) to control the speed of the drive systems which cannot reduce the torque ripples but suffers from system disturbances as parameter dependency. PI controllers are used for the simplicity of implementation and the broad knowledge base associated with years of work. Real-time implementation of PI controllers involves simple routines, permitting rapid loop execution, the key to a fast response.

In Chapter 2, the mathematical model of the IPMSM drive has been derived and basics of the conventional DTFC scheme are discussed. Based on the voltage vector look-up table how actual flux track the reference flux is also presented. The vector control operating principle is also presented in this Chapter.

In Chapter 3, based on the problems of conventional six-sector based DTFC scheme, a novel eighteen-sector based DTFC scheme incorporating LMA has been proposed. For the conventional DTFC scheme, a novel sector number determination algorithm has been developed to reduce computational burden of the microprocessor. In conventional DTFC, motor stator flux linkage has been considered constant which cannot optimize the motor efficiency and motor actual speed cannot follow the command speed. Therefore, loss minimization algorithm (LMA) has been developed to estimate the reference air gap flux linkage. Furthermore, in conventional DTFC, unbalanced effects of stator voltage in one sector can result unbalanced flux tracking which results high torque ripples. Therefore, Eighteen-sector based DTFC scheme has been proposed using the same six voltage vectors from the inverters. Finally, instead of torque and flux increase/decrease, small torque and flux increase/decrease concept has been introduced.

In Chapter 4, proposed novel eighteen-sector based DTFC with LMA has been simulated. Comparison of the proposed DTFC with conventional six-sector based DTFC scheme has been made. Furthermore, comparative performance analysis has been made with constant flux eighteen-sector based DTFC and conventional VC scheme. It is found that, the proposed eighteen-sector based DTFC with LMA maintains reduced torque ripples with high efficiency over a wide speed range. Finally, a five level torque hysteresis comparator based DTFC scheme has been simulated which further reduces the torque ripples.

In Chapter 5, Real-time implementation has been achieved using a DSP board DS1104 for a laboratory 5-hp IPMSM motor. The performance of the proposed DTFC has been experimentally investigated at different dynamic operating conditions. The experimental results validated the simulations presented in Chapter 4. Finally, in this Chapter, a comparison between the conventional six-sector based DTFC with LMA, eighteen-sector constant flux based DTFC, VC and proposed eighteen-sector based DTFC with LMA has been made. The experimental results are obtained under the same operating conditions to validate the superior performances of the proposed DTFC. The comparative results show that the proposed DTFC has lower torque ripples in steady state at different dynamic operating conditions.

As the earlier developed DTFC scheme suffers from torque ripples, therefore a nonlinear controller has been developed by considering both motor electromagnetic developed torque and stator air-gap flux linkage as virtual control variable has been presented in Chapter 6. In the first step, motor electromagnetic developed torque is considered as virtual control variable and based on the limitations of the controller, a novel nonlinear controller is developed considering both motor electromagnetic developed torque and stator air-gap flux linkage as control variable and stability of the proposed controller is verified by the Lyapunov's stability theory. The performance of the proposed nonlinear controller has been investigated in both simulation and experiment at different operating conditions. It is found from results that the proposed nonlinear controller with torque and flux as control variables has negligible torque ripples in steady state than the modified eighteen-sector based DTFC scheme.

7.1 Major Contributions of the Thesis

The key contributions of this thesis work are:

- A new stator flux linkage sector selection algorithm has been developed that is simpler as compared to the conventional trigonometric function based algorithm. The developed sector determination algorithm performs equivalent performance reducing the computational burden of the microprocessor.
- The conventional six-sector based DTFC has been modified into eighteen-sector based DTFC to reduce the unbalance stator voltage effects in any sectors. The performances have been investigated both in simulation and experimentally.
- Instead of conventional torque and flux increase/decrease, a look up table has been developed considering small torque and flux increase/decrease due to the tangential voltage vector reduction for sector number modifications. Therefore, torque ripples are significantly reduced.
- The proposed eighteen-sector based DTFC incorporating LMA has been successfully implemented in a real-time environment using DSP board DS1104. The dynamic performance of the proposed DTFC has been rigorously tested in this experimental environment with a laboratory 5-hp IPMSM. Comparative results to a conventional six-sector based DTFC have demonstrated the superior performance of the proposed eighteen-sector based DTFC scheme.
- Finally, a backstepping based nonlinear controller has been developed which further reduce the torque ripples and performs better in dynamic performance in terms of

torque ripples at steady state. For the nonlinear controller development both motor electromagnetic developed torque and stator air-gap flux linkage has been considered as virtual control variables. The stability of the proposed controller has been verified by the Lyapunov's stability theory and identifies the negative definite.

7.2 Future Work

Although the complete novel DTFC scheme of IPMSM drive has been successfully implemented in real time but still there are some issues which can be improved. Further, in terms of control development and potential for improvement of control algorithms, the following observations have been made.

- Instead of conventional PI controller, fuzzy logic, TSK-type neuro-fuzzy, neural networks or intelligent controllers for speed control of IPMSM can be used.
- R_s, L_d , L_q and T_L parameter estimations should be included in the nonlinear controller design. Then, the performance may be compared with the developed nonlinear controller developed in this thesis.
- Core loss should be included in the nonlinear controller design. Then, the performance may be compared with the eighteen-sector based DTFC scheme incorporating LMA.

In terms of experimental implementation, the following devices/components may be improved.

- Hall Effect current sensors can be improved. While the effect on control is less significant than might be thought, using a compact linear Hall sensor array like the ACS715 from Allegro Microsystems is space efficient, more reliable and accurate, with factory calibration.
- In addition to the current and position sensor, a torque sensor should be used, the current lack of direct shaft torque measurement limits potential comparison and analysis, and forces approximation of loading using other techniques with high error margins.
- Better routing and shielding can improve the noise problems of the control and feedback systems.

References

[1] P.C. Sen, "Electric Motor Drives and Control-Past, Present and Future," IEEE Transactions on Industrial Electronics, vol. 39, no. 2, pp. 562-575, December 1990.

[2] P.C. Sen, "Principles of Electric Machines and Power Electronics," New York: Wiley, 1988.

[3] B.K. Bose, "Power Electronics and AC drives," Englewood Cliffs, NJ: Prentice Hall, 1986.

[4] R.M. Crowder, "Electric Drives and Their Controls," Clarendon Press, 1995.

[5] S.J. Chapman, "Electric Machinery Fundamentals," New York, NY: McGraw-Hill, 1999.

[6] E.C. Lister and M.R. Golding, "Electric Circuits and Machines," McGraw-Hill Ryerson Limited, 1987.

[7] M.A. Rahman, "Permanent Magnet Synchronous Motor- A Riview of the State of Design Art," Proceedings of International Conference on Electric Machines, pp. 312-319, Athens, 1980.

[8] M.N. Uddin, "Intelligent control of an Interior Permanent Magnet Synchronous Motor," PhD. Thesis, Memorial University of Newfoundland, St. John, 2000.

[9] A.V. Gummaste and G. R. Slemon, "Steady State Analysis of a Permanent Magnet Synchronous Motor Drive with Voltage Source Inverter," IEEE Transaction on Industrial applications, vol. 17, no. 2, pp. 143-151, March/April 1981.

[10] G.R. Slemon and A. V. Gummaste, "Steady State Analysis of a Permanent Magnet Synchronous Motor Drive with Current Source Inverter," IEEE Transaction on Industrial applications, vol. 19, no. 2, pp. 190-197, March/April 1983.

[11] M.N. Uddin and M. Hafeez, "FLC Based Scheme to Improve the Dynamic Performance of an IM Drive," IEEE Industry Applications Society Annual Meeting, pp. 1-7, October 2010.

[12] M.N. Uddin, HonBin Zou and F. Azevedo, "Online Loss-Minimization-Based Adaptive Flux Observer for Direct Torque and Flux Control of PMSM Drive," IEEE Transactions on Industry Applications, vol. 52, no. 1. pp. 425-431, January/February 2016.

[13] J. Faiz, and Zonoozi, "A Novel Technique for Estimation and Control of Stator Flux of a Salient-Pole PMSM in DTC method based on MTPF," IEEE Transactions on Industrial Electronics, vol. 50, no. 2, pp. 262-271-1494, April 2003.

[14] S. Bolognani, L. Peretti and M.Zigliotto, "Online MTPA Control Strategy for DTFC Synchronous Reluctance Motor Drives," IEEE Transactions on Power Electronics, vol. 26, no.1, pp.20-28, january 2011.

[15] M. Hafeez, M. N. Uddin and R.S. Rebeiro, "FLC Based Hysteresis Band Adaptation to Optimize Torque and Stator Flux Ripples of a DTC Based IM Drive," IEEE Electric Power and Energy Conference, pp. 1-5, August 2010.

[16] M.N. Uddin, Hao Wen, R.S. Rebeiro and M. Hafeez, "Experimental Performance of a Model Reference Adaptive Flux Observer Based NFC for IM Drive," IEEE Industry Applications Society Annual Meeting, pp. 1-8, October 2011.

[17] Y. Inoue, S.Morimoto and M. Sanada, "Comparative Study of PMSM Drive Systems Based on Curent Control and Direct Torque Control in Flux-Weakening Control Region," IEEE Transactions on Industry Applications, vol. 48, no. 6, pp. 2382-2389, December 2012.

[18] A. Khoobroo and B. Fahimi, "Magnetic Flux Estimation in a Permanent Magnet Synchronous Machine Using Field Reconstruction Method," IEEE Transactions on Energy Conversion, vol. 26, no. 3, pp. 757-765,September 2011.

[19] K. Jun-Koo and S. Seung-Ki, "New Direct Torque Control of Induction Motor for Minimum Torque Ripple and Constant Switching Frequency," IEEE Transactions on Industry Applications, vol. 35, no. 5, pp. 1076-1082, September/October 1999.

[20] L.K. Beum, S.J.Ho, I. Choy and Y. Ji-Yoon, "Torque Ripple Reduction in DTC of Induction Motor Driveb by Three-Level Inverter with Low Switching Frequency," IEEE Transactions on Power Electronics, vol. 17, no. 2, pp. 255-264, March 2002.

[21] L. Yaohua and D. Gerling, "Voltage Vector Selection Strategy for the Interior PMSM DTC system," Proceedings of the 14th European Conference on Power Electronics and Applications, pp. 1-9, September 2011.

[22] G. Foo and M.F. Rahman, "Direct Torque and Flux Control of an IPM Synchronous Motor Drive Using Backstepping Approach ," IET on Electric Power Applications, vol.3, no. 5, pp. 413-421, September 2009.

[23] Z. Yongchang and Z. Jianguo, "A Novel Duty Cycle Control Strategy to Reduce Both Torque and Flux Ripples for DTC of Permanenet Magnet Synchronous Motor Drives With Switching Frequency Reduction," IEEE Transactions on Power Electronics, vol. 16, no. 10, pp. 3055-3067, October 2011.

[24] J. Mengjja, S. Cenwei, Q. Jianqi and L. Ruiguang, "Stator Flux Estimation for Direct Torque Controlled Surface Mounted Permanent Magnet Synchronous Motor Drives Over Wide Speed Region," Proceedings of the 18th International Conference on Electrical Machines and Systems, vol. 1, pp. 350-354, September 2005.

[25] Z. Chunmei, L. Heping, C. Shujin and W. Fangjun, "Application of Neural Networks for Permanent Magnet Synchronous Motor Direct Torque Control," Journal of Systems Engineering and Electronics, vol. 19, no. 3, pp. 555-561, June 2008.

[26] L. Zhong, M.F. Rahman, W.Y. Hu, K.W. Lim and M.A. Rahman, "A Direct Torque Controller for Permanent Magnet Synchronous Motor Drives," IEEE Transactions on Energy Conversion, vol. 14, no. 3, pp. 637-642, September 1999.

[27] M.N. Uddin and M. Hafeez, "FLC Based DTC Scheme to Improve the Dynamic Performance of an IM Drive," IEEE Transactions on Industry Applications, vol. 48, no. 2, pp. 823-831, March/April 2012.

[28] R.S. Colby and D.W. Novotny, "An Efficiency-Optimizing Permanent Magnet Synchronous Motor Drive," IEEE Transactions on Industry Applications, vol. 24, no. 3, pp. 462-469, May/June 1988.

[29] I. Kioskeridis and N. Margaris, "Loss Minimization in Scalar-Controlled Induction Motor Drives With Search Controllers," IEEE Transactions on Power Electronics, vol. 11, no. 2, pp. 213-220, March 1996.

[30] M.N. Uddin and S.W. Nam, "Online Loss-Minimization-Based Control of an Induction Motor Drive," IEEE Transactions on Power Electronics, vol. 23, issue. 2, pp. 926-931, March 2008.

[31] S. Morimoto, Y. Tong, Y. Takeda and T. Hirasa, "Loss Minimiozation Control of Permanent Magnet Synchronous Motor Drives," IEEE Transactions on Industrial Electronics, vol. 41, no. 5, pp. 511-517, October 1994.

[32] S. Vaez-Zadeh and M. Khayamy, "Efficiency-Optimizing Direct Torque Control of Interior Permanent Magnet Synchronous Machines With Fast Start Up," 4th IET Conference on Power Electronics, pp. 218-224, 2008.

[33] S. Vaez, V.I. John and M.A. Rahman, "An On-line Loss Minimization Controller for Interior Permanent Magnet Synchronous Motor Drives," IEEE Transactions on Energy Conversion, vol. 14, no. 4, pp. 1435-1440, December 1999.

[34] S. Vaez-Zadeh, M. Zamanifar and J. Soltani, "Nonlinear Efficiency Optimization Control of IPM Synchronous Motor Drives With Online Parameter Estimation," 37th IEEE Power Electronics Specialists Conference, pp. 1-6, June 2006.

[35] Y. Kaipin, G. Hong, S. Zedong and Z. Zhiyoung, "Efficiency Optimization Control of Permanent Magnet Synchronous Motor For Electric Propulsion System," International Conference on Electrical Machines and Systems, pp. 56-61, October 2013.

[36] Alberto Pigazo, and Victor M. Moreno, "Accurate and Computationally Efficienct Implementation of the IEEE 1459-2000 Standard in Three-Phase Three-Wire Power Systems" IEEE Transactions on Power Delivery, vol. 22, no. 2, pp. 752-757, April 2007.

[37] R. E. Fowkes, "Hardware Efficiency Algorithms for Trigonometric Functions," IEEE Transactions on Computers, vol. 42, no. 2, pp. 235-239, February 1993.

[38] M.A. Khan, M.N. Uddin and M.A. Rahman, "A New Loss Minimization Control of Interior Permanent Magnet Motor Drives Operating with a Wavelet based Speed Controller," IEEE Industry Application Society Annual Meeting, pp. 1-8, October 2011.

[39] C. Mademlis, I. Kioskeridis and N. Margaris, "Optimal Efficiency Control Strategy for Interior Permanent-Magnet Synchronous Motor Drives" IEEE Transactions on Energy Conversion, vol. 19, no. 4, pp. 715-723, December 2004.

[40] Data sheets of SEMIKRON, SKHI 22 AR inverter manual.

[41] P.A. Hokayem and E. Gallestey, "Lyalunov Stability Theory," Nonlinear Systems and Control, Spring 2015,

[42] J. Soltani and M. Pahlavaninezhad, "Adaptive Backstepping Based Controller Design for Interior type PMSM Using Maximum Torque Per Ampere Strategy," International Conference on Power Electronics and Drives Systems, vol. 1, pp. 596-601, November 2005.

[43] D.F. Chen, T.H. Liu and C.K. Hung, "Nonlinear Adaptive Backstepping Controller Design for a Matrix-Converter Based PMSM Control SystemInterior type PMSM Using Maximum Torque Per Ampere Strategy," The 29th Annual Conference of the IEEE Industrial Electronics Society, vol. 1, pp. 673-678, November 2003.

[44] Md. M. I. Chy. and M.N. Uddin, "Development of a Nonlinear Speed Controller Controller of IPMSM Drive Incorporating MTPA with Mechanical Parameter Estimation," IEEE International Electric Machines and Drives Conference, pp. 322-327, May 2007.

[45] dSPACE, "Digital signal processing and Control Engineering", Implementation Guide, Paderborn, Germany, 2003.

[46] dSPACE GmbH, "DS1104 R&D Controller Board: Hardware Installation & Configuration," dSPACE GmbH, Paderborn, 2008.

[47] dSPACE GmbH, "DS1104 R&D Controller Board: RTLib Reference," dSPACE GmbH, Paderborn, 2008.

Appendix A

Parameters & Coefficients

This appendix provides numerical values for all system parameters, including machine, switch elements, and controller coefficients used in simulation and real-time scenarios.

Table A-1: IPMSM parameters

Parameter	Label	Value	Unit	Abbreviation/Symbol
Rated power	P_{rated}	3.7	Kilo-watt	kW
Rated voltage[1]	V_{rated}	183	volt	V
Rated current	I_{rated}	14.2	Ampere	A
Rated Frequency	f_{rated}	87.5	cycle/second	Hz
Rated speed	ω_{rated}	183.3	rad/second	rad/s
Pole pairs	P	3		
d-axis inductance	L_d	5.06	milli-Henry	mH
q-axis inductance	L_q	6.42	milli-Henry	mH
Stator resistance	R_s	0.242	Ohm	Ω
Inertia constant	J	0.0133	Kg(meter^2)	Kgm^2
Damping coefficient	B_m	0.001	Nm/rad/s	Nm/rad/s
Magnetic flux constant	Φ_m	0.2449	volt/rad/s	v/rad/s

Table A-2: Switch element parameters

Parameter	Label	Value	Unit
Transistor saturation voltage	V_{ce}^{sat}	2.5	V
Transistor resistance	R_{trans}	2.00E-02	Ω
Diode threshold	V_{thresh}	2	v
Diode resistance	R_{diode}	2.20E-02	Ω

---

[1] Voltages cited in line-line root mean square quantity unless otherwise specified

Appendix B

Simulink Subsystems

The details of the subsystem blocks for the Simulink schematic of the complete proposed novel DTFC scheme as shown in Fig. 3.4 have been presented in this appendix.

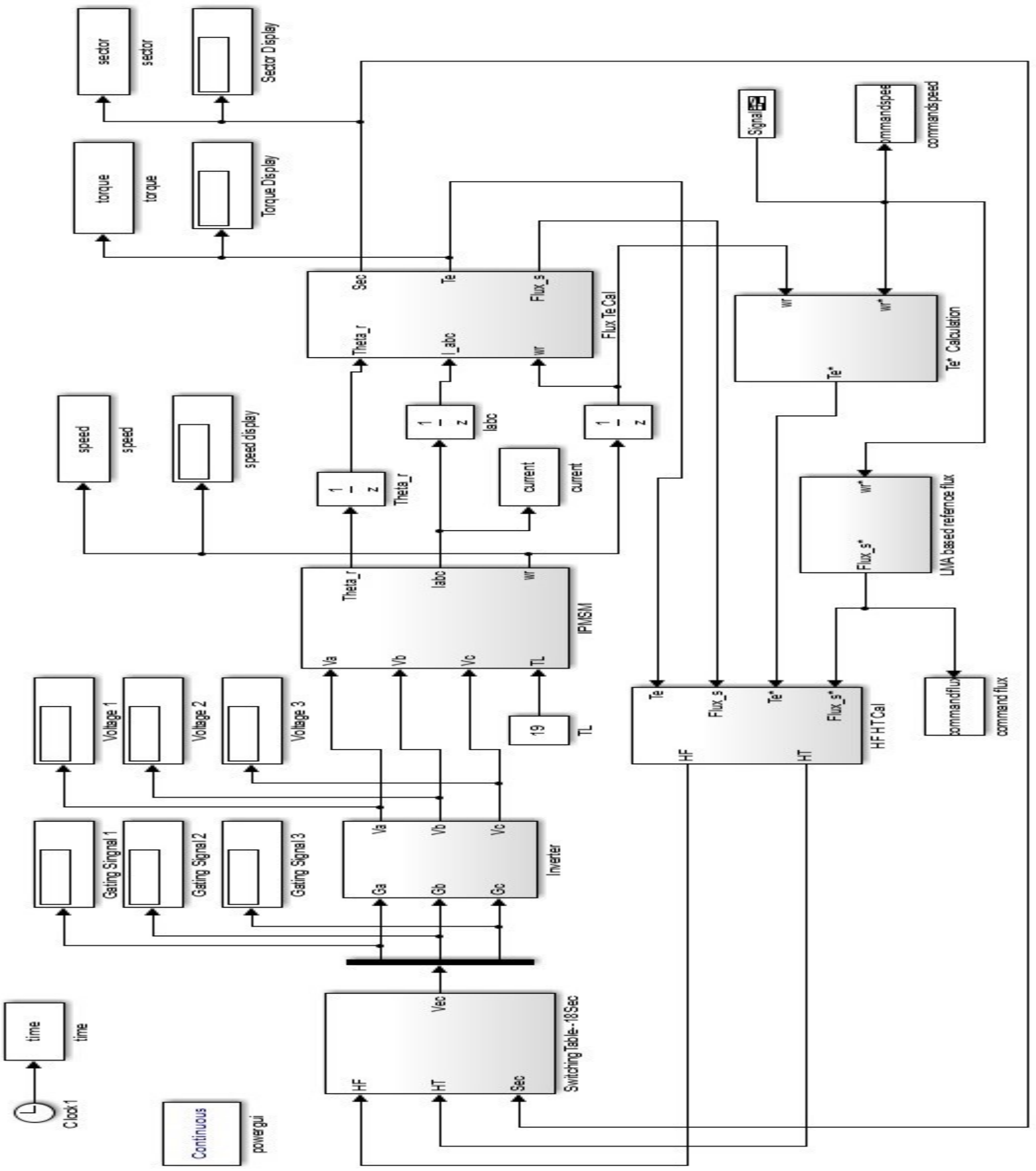

B.1 Complete Simulink model of the proposed novel eighteen-sector based DTFC scheme incorporating LMA.

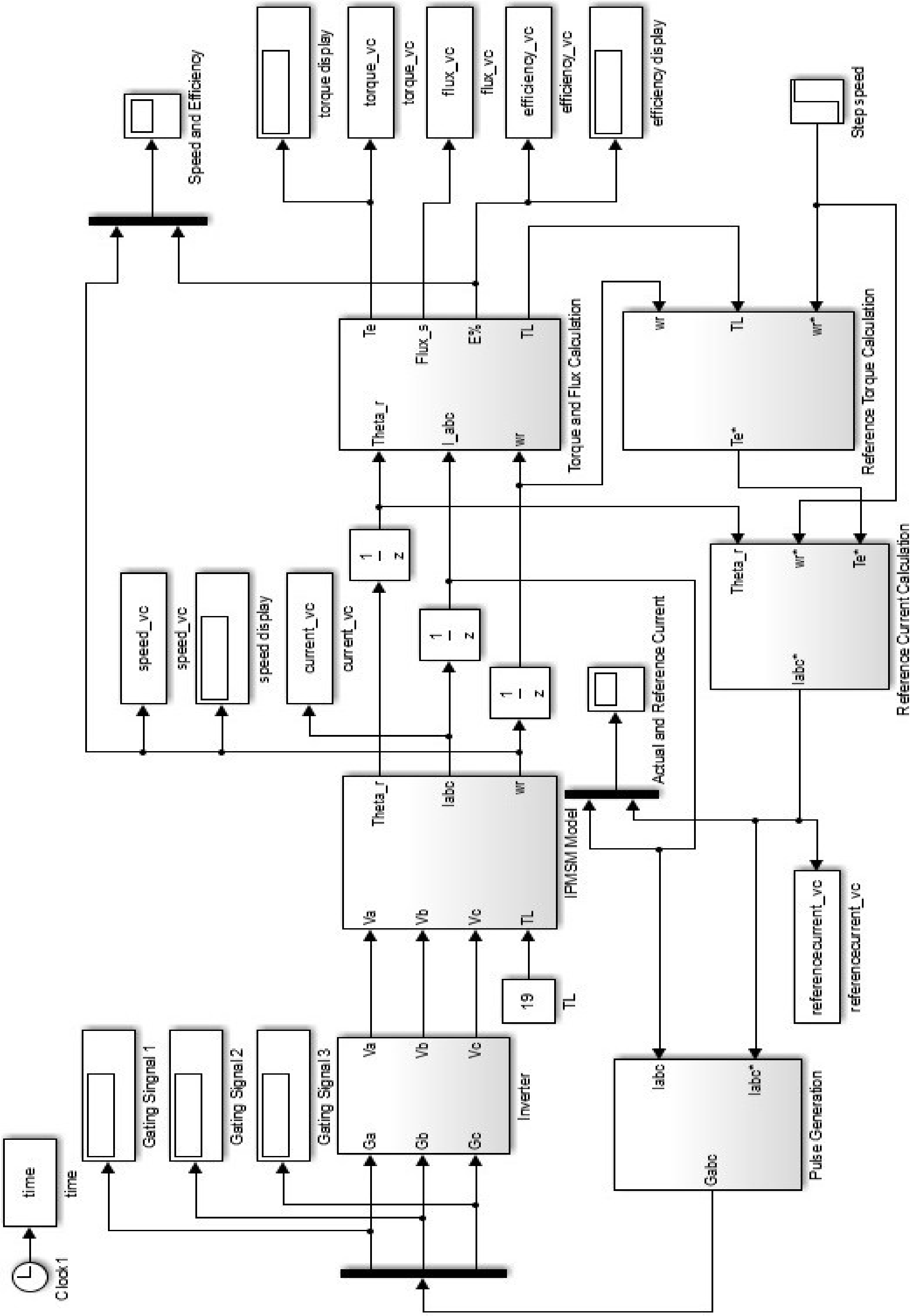

B.2 Complete Simulink model of the VC scheme incorporating LMA.

Appendix C

Simulink Subsystems of the Proposed Nonlinear Controller with Torque and Flux as Control Variable

The details of the subsystem blocks for the Simulink schematic of the backstepping based proposed nonlinear controller of IPMSM drive as shown in Fig. 5.11 have been presented in this appendix. The inputs to the controller subsystem are command speed (ω_r^*), the feedback actual speed (ω_r), motor actual torque (T_e), flux linkage ψ_s and reference flux linkage (ψ_s^*). The vector rotator generates the voltages (v_a,v_b,v_c). The output of the subsystem acts as an input to the gate signal generator subsystem and output of the subsystem are the logic signals NA. NB and NC which hare used to turn the inverter switches 'ON' and 'OFF'. The input of the inverter subsystem (C.4) is logic signals NA, NB, NC and the dc bus voltage VDC. The outputs of this subsystem are the d-q axis voltages in the stationary reference frame. The coordinate transformation subsystem (C.5) transforms d-q axis voltages from the stationary frame to the synchronously rotating rotor reference frame. The d-q axis currents generation subsystem (C.6) generates d-q axis currents in the rotating reference frame from the synchronously rotating d-q axis voltages and motor parameters. In the same subsystem motor electromagnetic torque (T_e) and stator flux linkage (ψ_s) determination is shown. The actual current generation subsystem (C.7) generates actual currents (i_a,i_b,i_c) from the synchronously rotating d-q axis currents and the rotor position angle. The motor output subsystem (C.8) generates the rotor position angle θ_r (theta) and the motor speed (ω_r) from the synchronously rotating d^r-q^r axis currents and motor parameters using the motor dynamics. Using the synchronously rotating current, voltage and stator flux linakges d and q axis flux linkages also flux errors are determined in subsystem C.9.

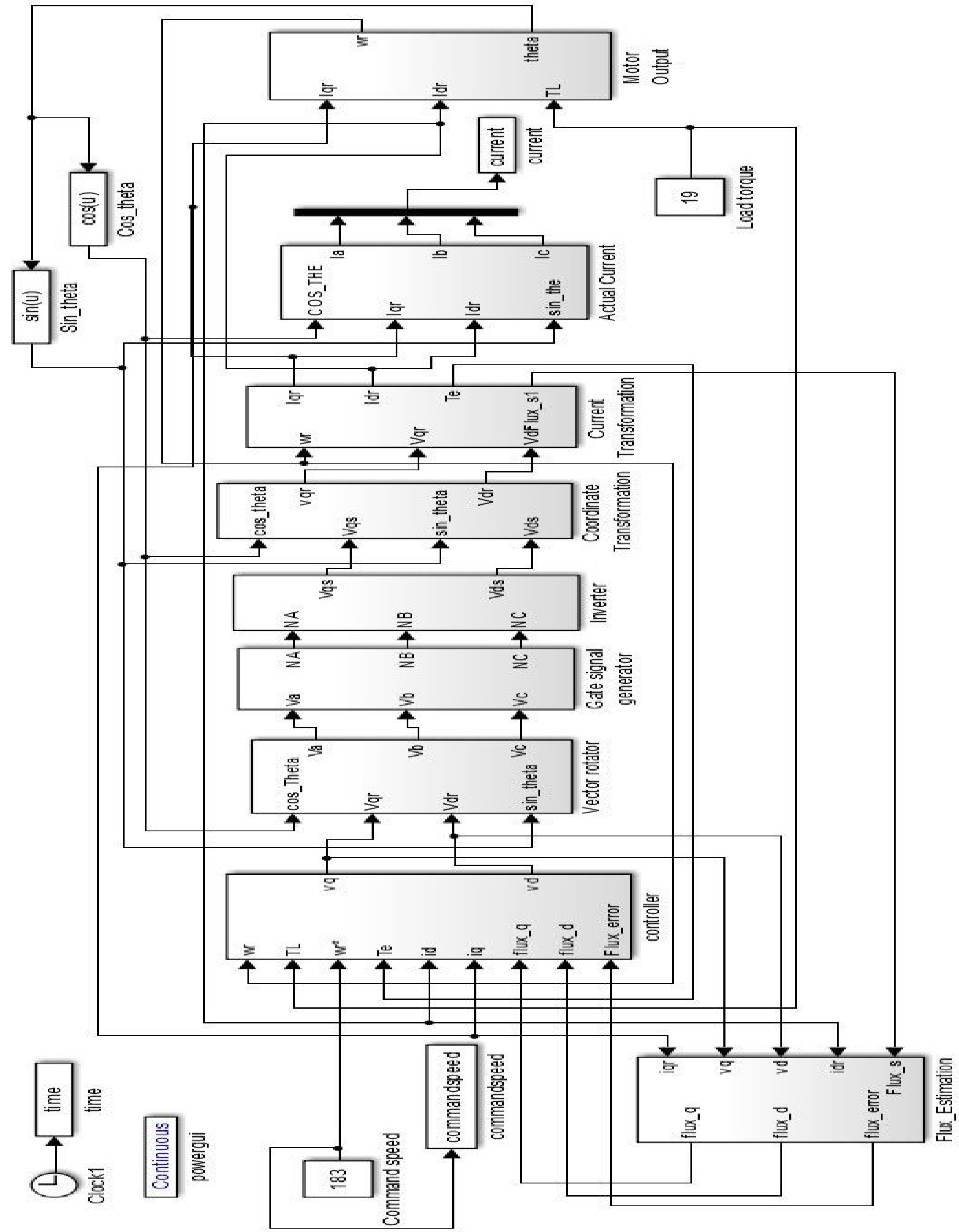

Figure C.1: Complete Simulink model of the proposed nonlinear controller of IPMSM drive.

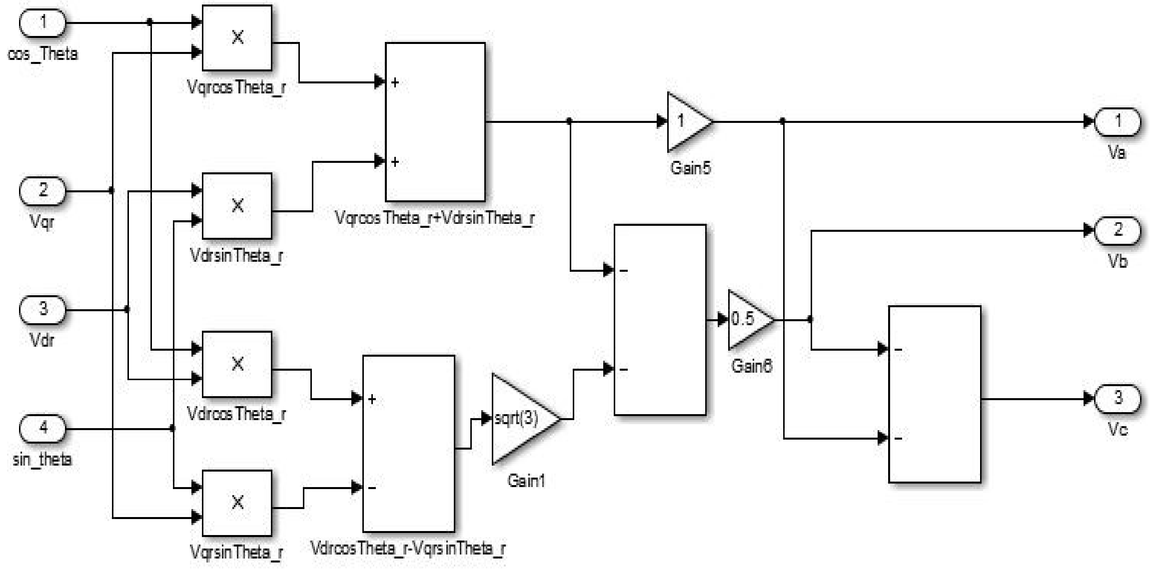

Figure C.2: Command voltage generator or vector rotator subsystem.

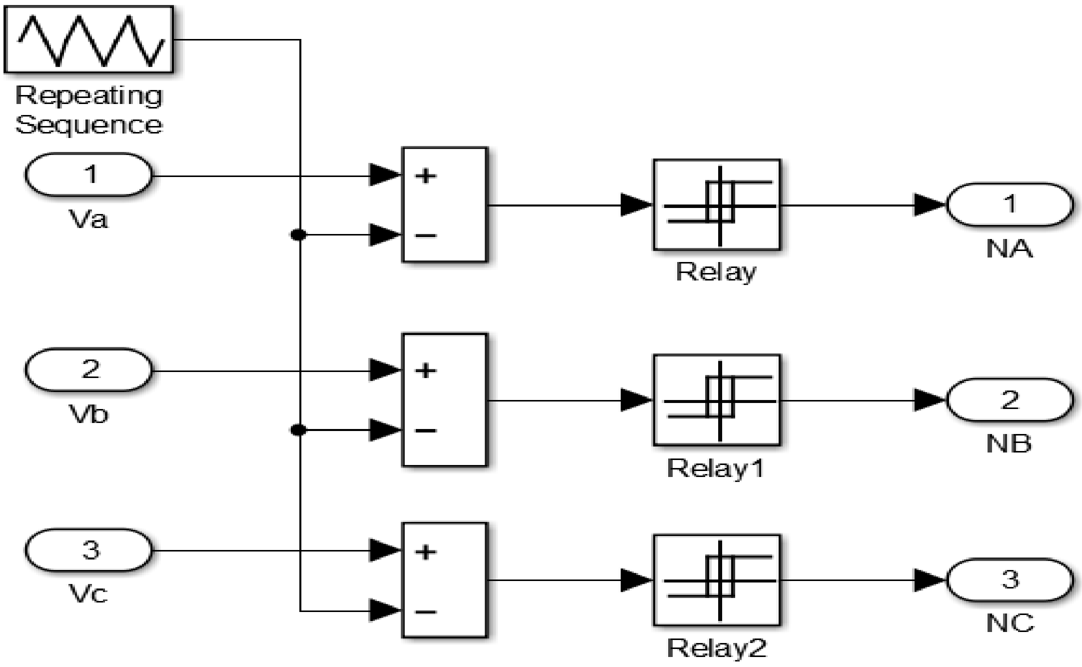

Figure C.3: Gate signal generator subsystem.

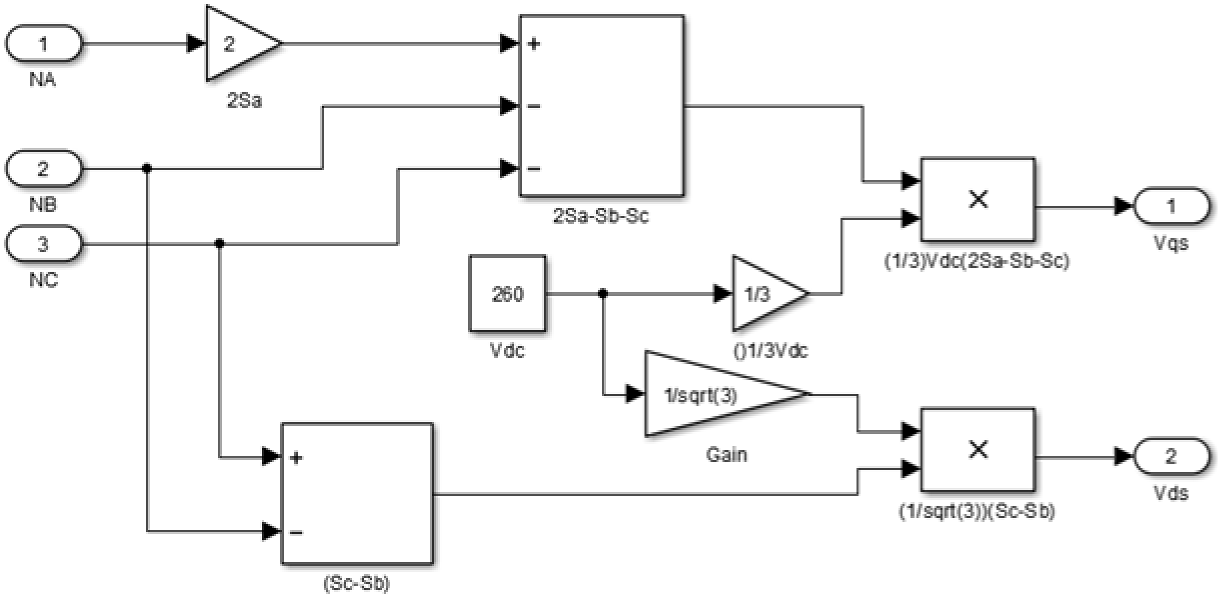

Figure C.4: 3-phase inverter subsystem.

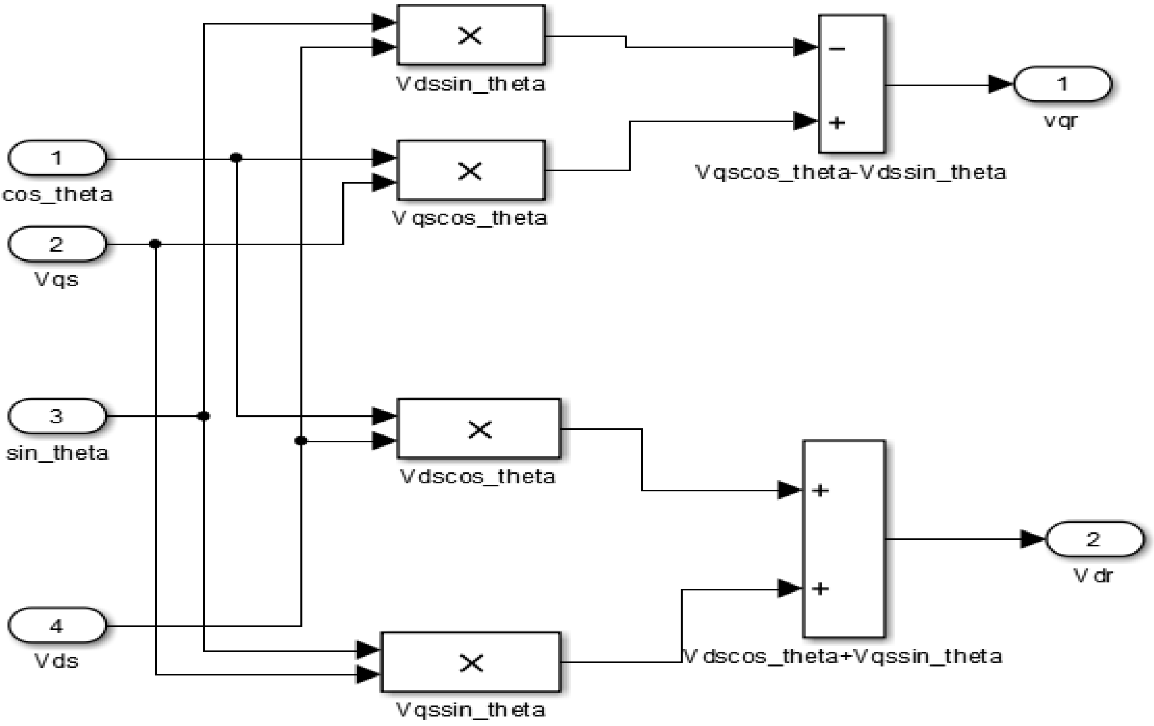

Figure C.5: Co-ordinate transformation subsystem.

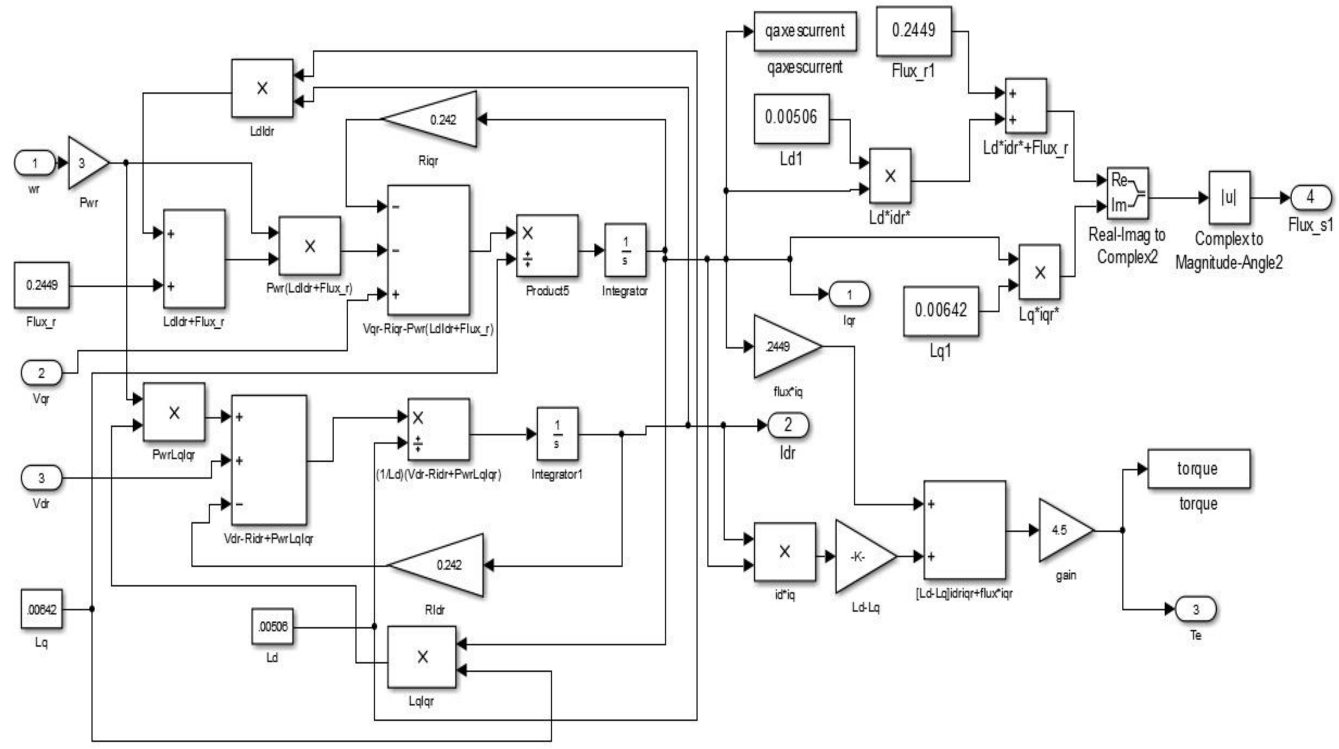

Figure C.6: Current transformation subsystem.

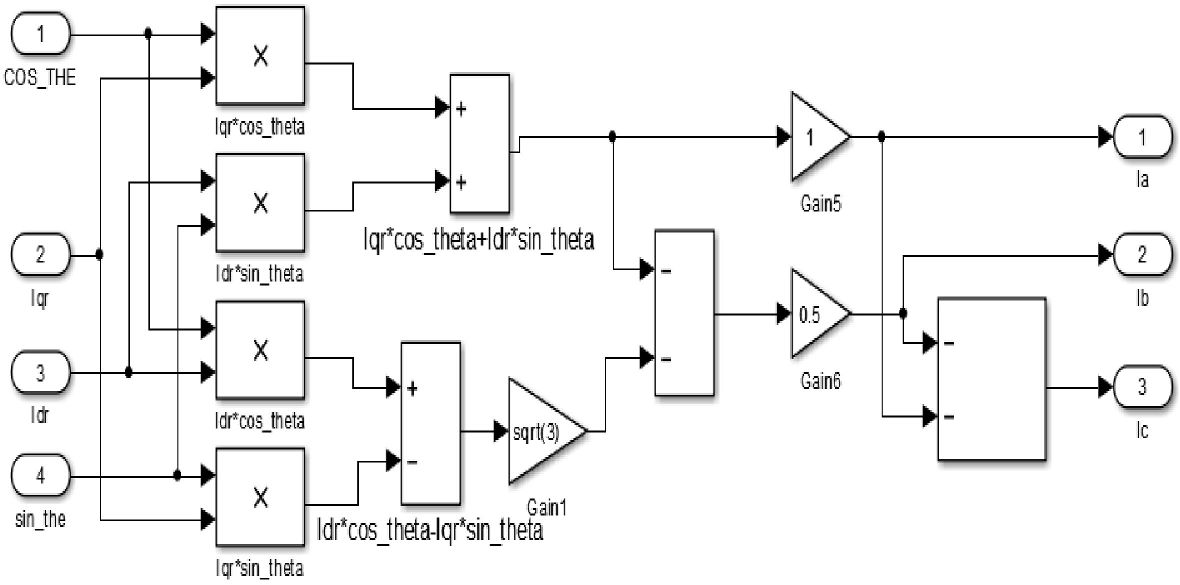

Figure C.7: Actual current subsystem.

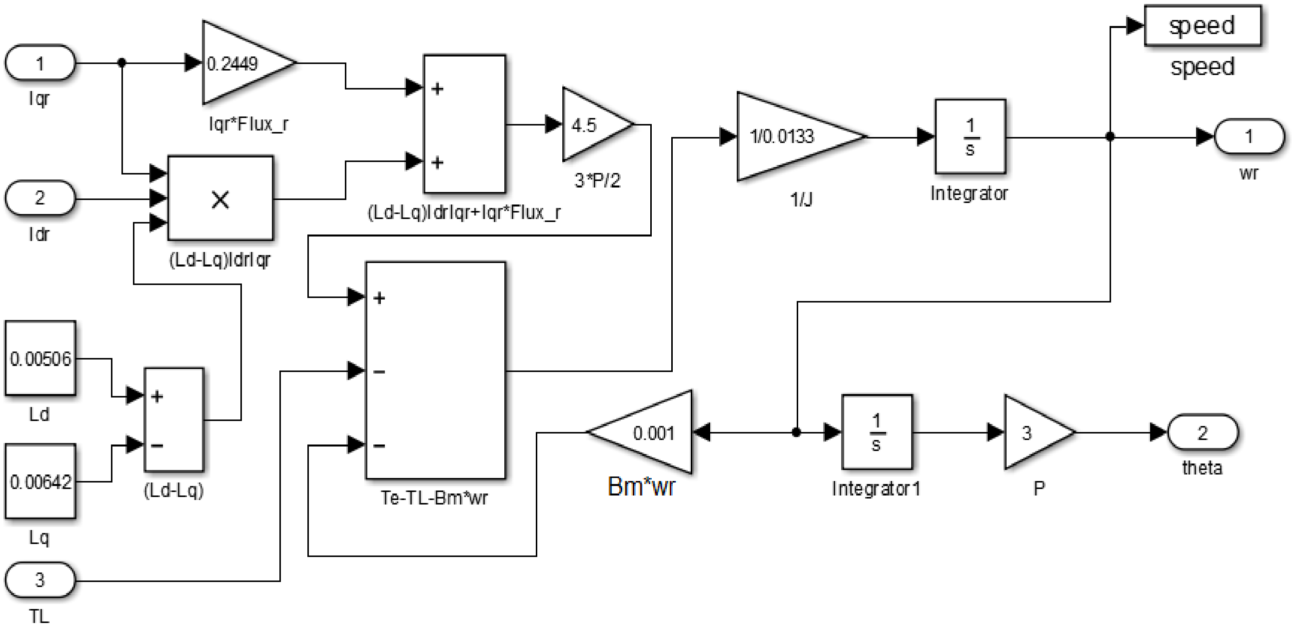

Figure C.8: Motor output subsystem.

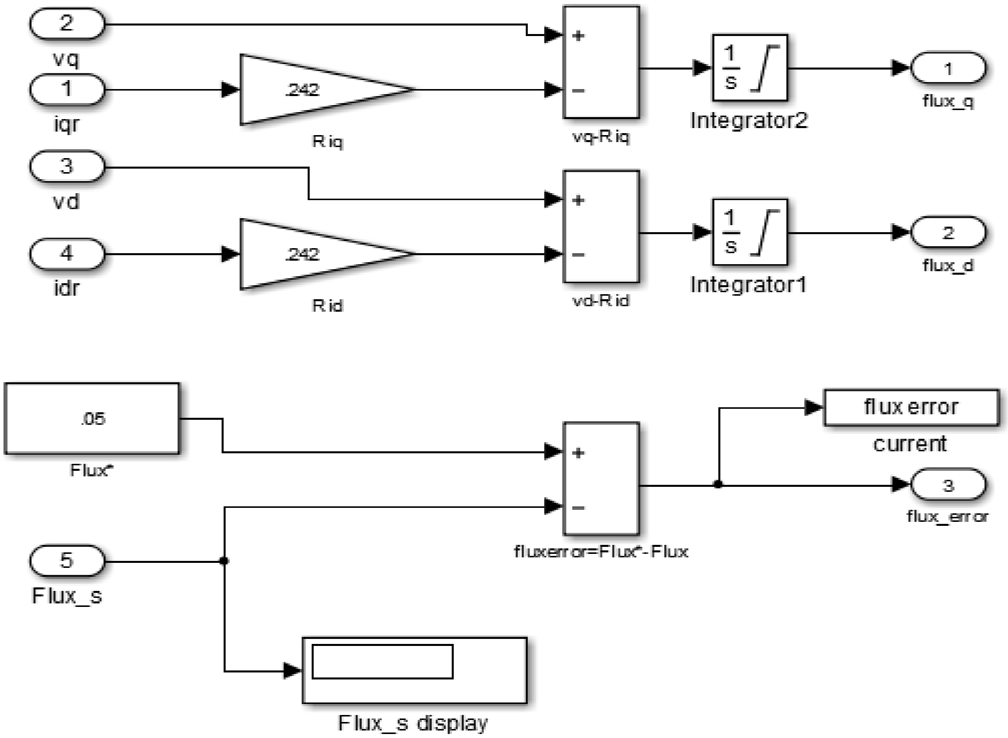

Figure C.9: Flux estimation subsystem.

Appendix D
IGBT Inverter

The advantages of bipolar junction transistors (BJTs) and metal-oxide semiconductor field-effect transistor (MOSFETs) are combined in an insulated gate bipolar transistor (IGBT). An IGBT has high input impedance like MOSFETs and low conduction loss like BJTs. Because of high input impedance the gate draws a very small leakage current. An IGBT has no second breakdown like the BJT. A BJT is a current controlled device and requires base current for following current in the collector. Since, the collector current is dependent on the base current so that current gain is highly dependent on the base current. However, an IGBT is a voltage controlled device like a power MOSFET. It has lower switching and conduction losses. IGBT is faster than the BJT but slower than a power MOSFET. The current and voltage ratings of a single IGBT can be up to 400 A, 1200 V and the switching frequency can be up to 20 kHz. The schematic of IGBT inverter is shown in Fig. D.1.

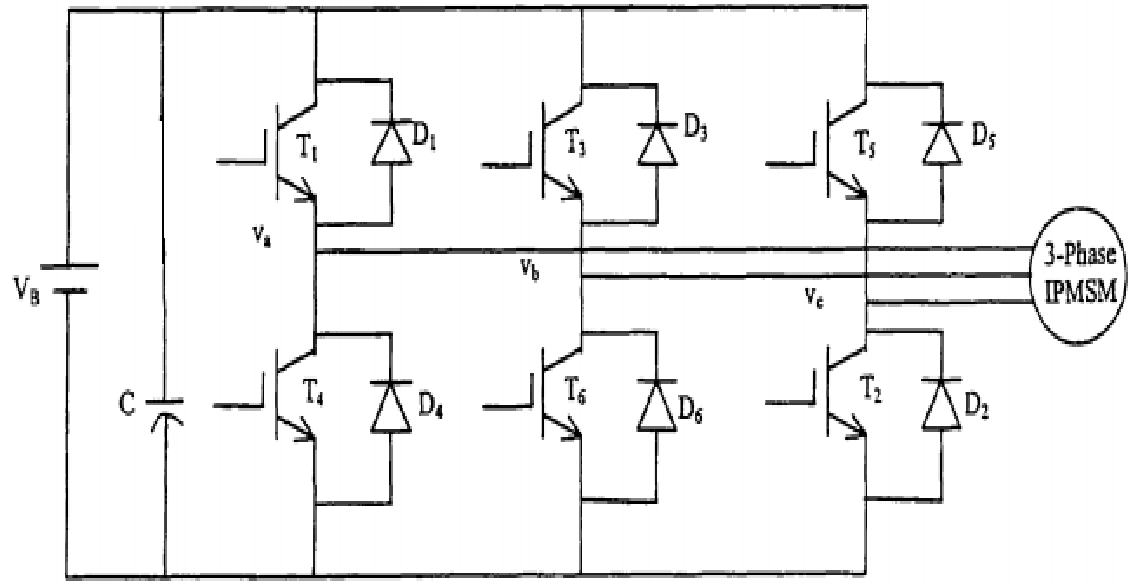

Figure D.1: Basic circuit of an IGBT inverter module.

Appendix E

Base Drive Circuits

For operating IGBTs as switches the gate voltage must be appropriate so that the IGBTs are into the saturation for low on-state voltage. The main function of the base drive circuit is to generate six pulses having proper voltage level for the six IGBTs of the inverter. The outputs of the digital I/O subsystem of the DSP board DS1104 are six pulses having magnitude of 5 V that is not sufficient for the gate drive of IGBTs. Moreover, isolation is needed between the logic circuits and IGBTs because the logic signal should be applied between the gate and the emitter. Thus, a base drive circuit is essential for the inverter to provide an isolation and appropriate voltage to the gate of IGBTs. The base drive circuit for the inverter is shown in Fig. E.1. The chip SN7407N has been used as level shifter that shifts the voltage level from +5V to +15V. An optocoupler is used to provide the isolation between the logic circuit and power circuit of the inverter. The base driver circuit provides six driving pulses for the switches of the inverter. The interface circuit for the current sensor is shown in Fig. E.2.

Resistance values are: R_1=R_2=R_3=R_4=R_5=R_6= 1.5 k.ohm

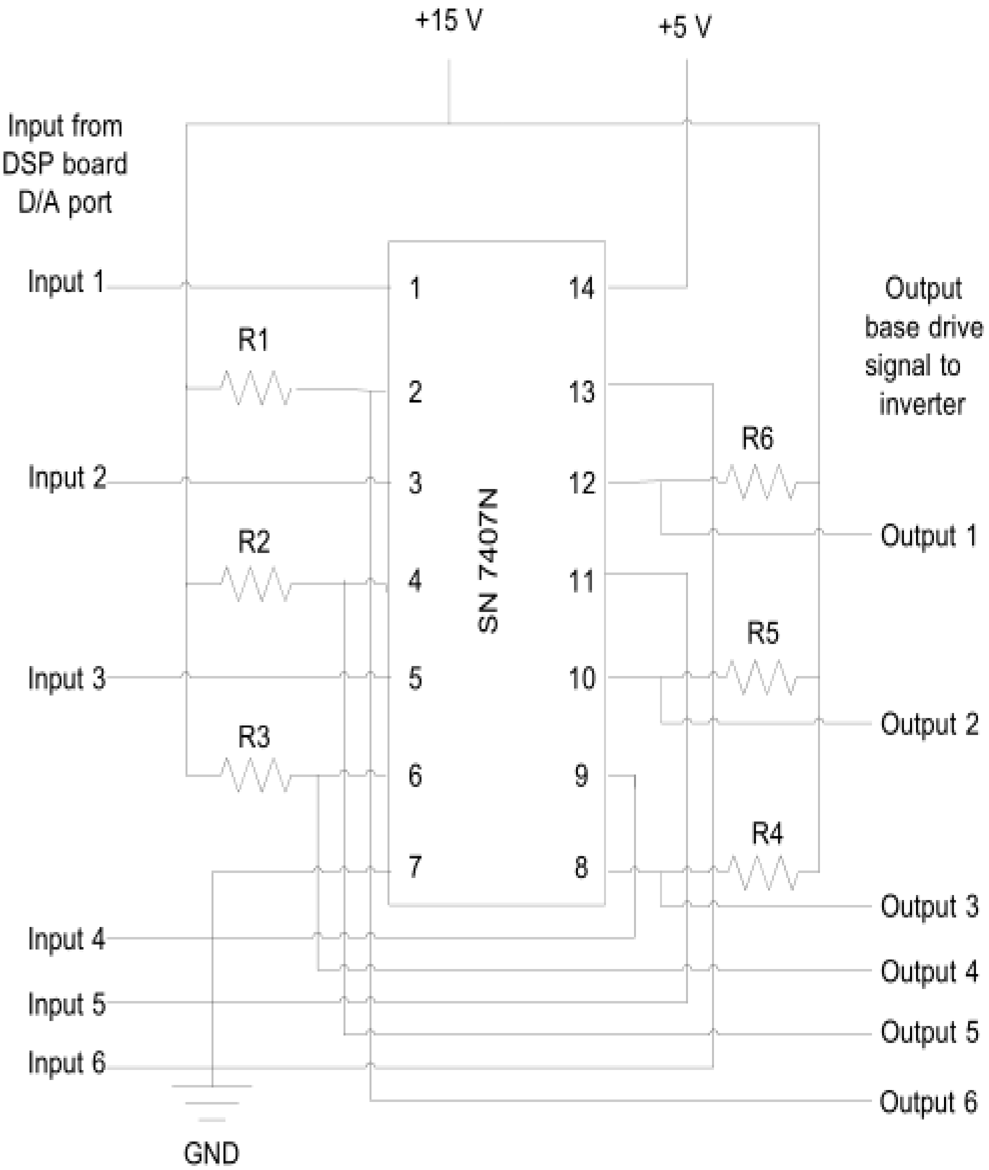

Figure E.1: Base drive circuit for the inverter.

Gain of Op-Amp (741CN)= $1+\frac{R_3}{R_2}$

Magnitude of Resistors:

	Current sensor for phase ‘a’	Current sensor for phase ‘b’
R_1	98.7 ohm	99 ohm
R_2	1.8 k	2 k
R_3	5.5 k	5.1 k

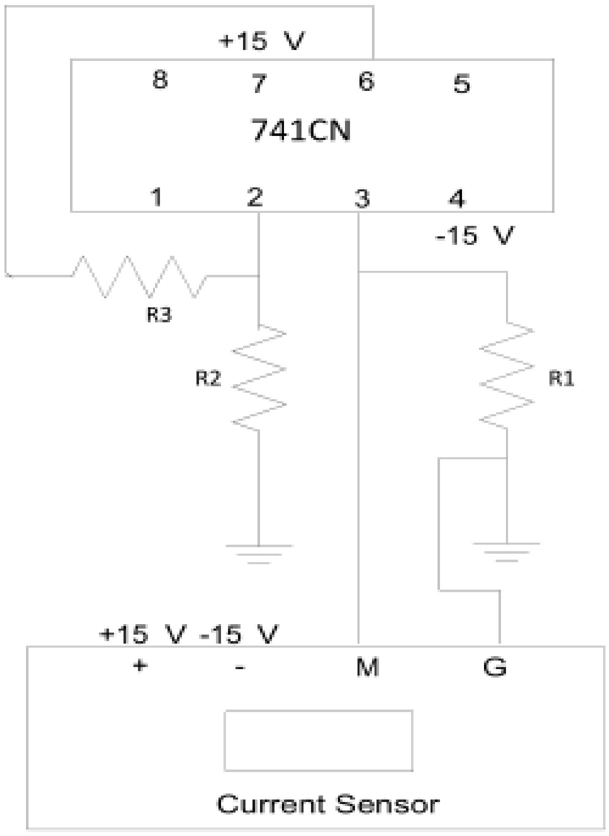

Figure E.2: Interface circuit for the current sensor.

Appendix F

Real-Time Simulink Model of IPMSM Drive

The following diagram details the major components of the real-time implementation block, with peripheral interface modules at the left (inputs) and right (outputs) margins. The Simulink model can be directly used for real-time applications using the software real-time interface (RTI) supplied by the dSPACE. The RTI's board library provides Simulink blocks representing DSPACE I/O hardware. The complete system Simulink diagram of the proposed eighteen-sector based DTFC incorporating LMA scheme is shown in Fig. F.1. It is shown in the figure that the board DS1104 has two incremental encoders but only encoder 1 is used for this work. The encoder 2 is terminated by a terminator. The A/D converters are used to read the actual motor currents from phase 'a' and 'b'. The output ports are used from the RTI library and the number of channel is selected according to the configuration required. The signals to be captured by the stored oscilloscope are fed to the D/A ports of the board.

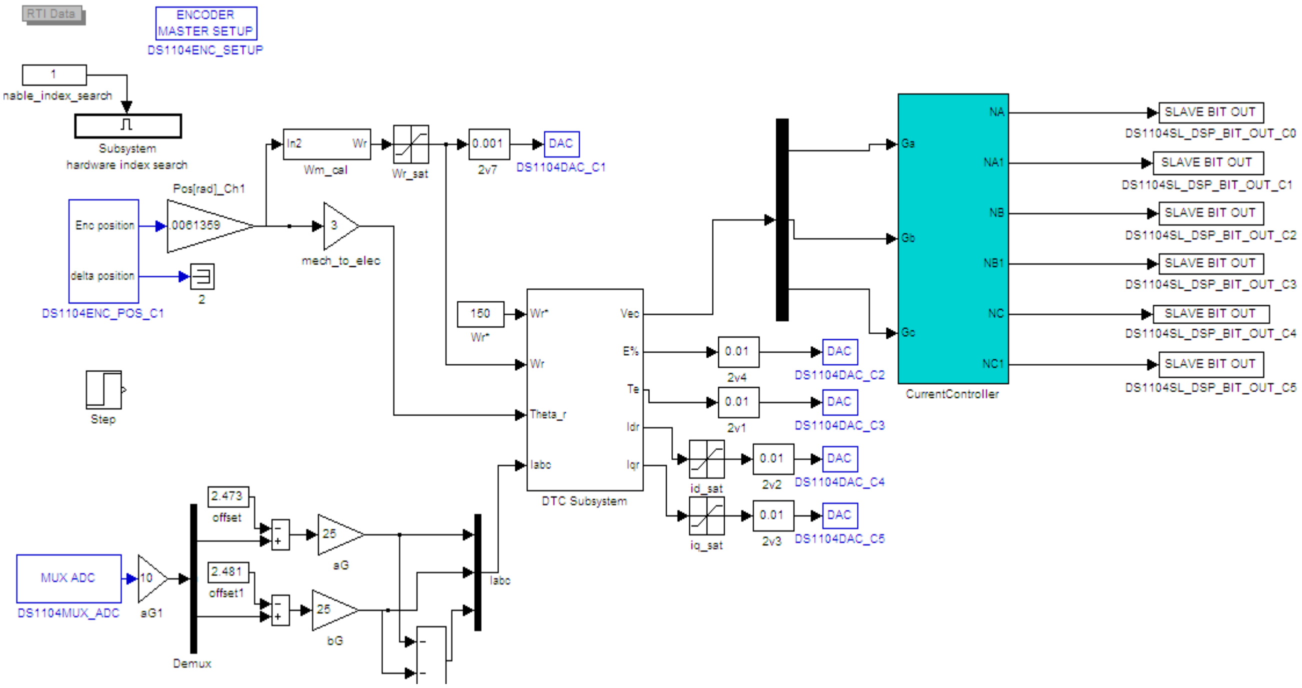

Figure F.1:Real-time Simulink model of proposed novel eighteen-sector based DTFC scheme incorporating LMA.

Figure F.2 shows the real-time Simulink model of VC scheme incorporating LMA.

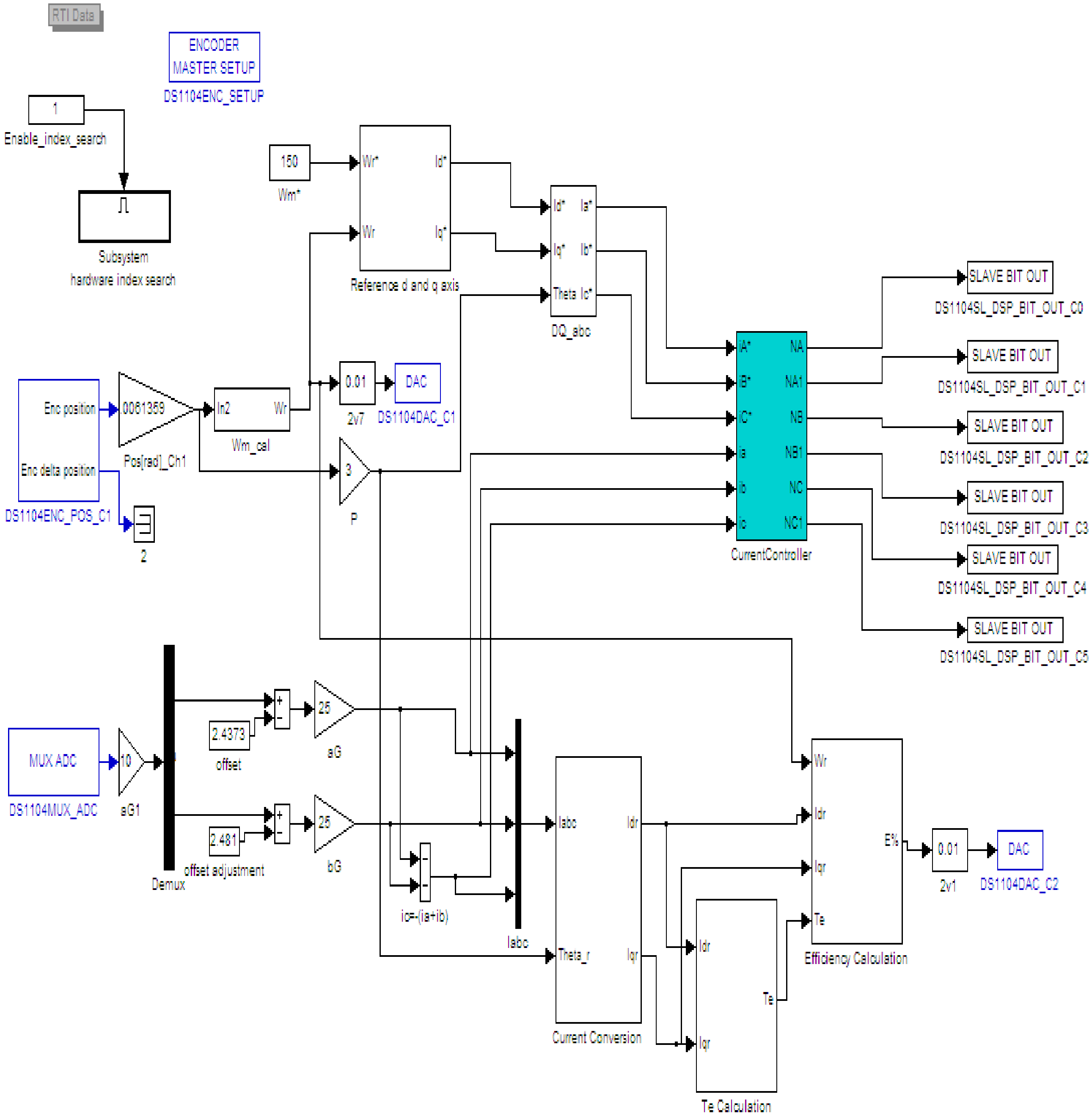

Figure F.2:Real-time Simulink model of VC scheme incorporating LMA.

Figure F.3 shows the real-time Simulink model of the proposed nonlinear controller based IPMSM drive considering motor electromagnetic developed torque and stator air-gap flux linkage as virtual control variables.

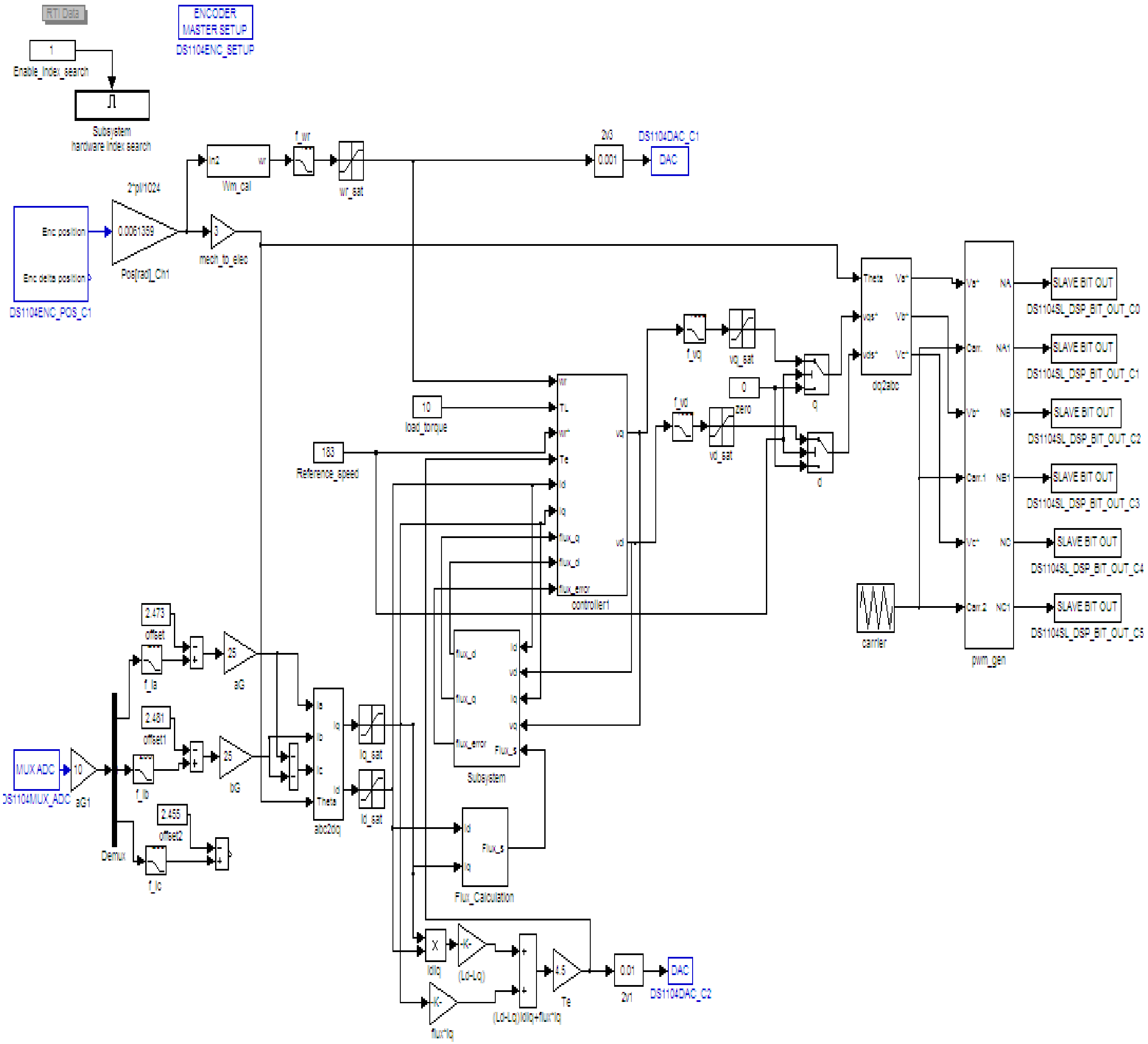

Figure F.3:Real-time Simulink model of proposed nonlinear controller based IPMSM drive.

Appendix G

Associated Publications

Submitted Paper:

[1] Md. Mizanur Rahman and M.N. Uddin, "A Novel DTFC Based IPMSM Drive with Improved Dynamic Performance and Efficiency," IEEE IAS Annual Meeting 2016, Portland, OR, USA.

[2] M.N. Uddin and Md. Mizanur Rahman, "Nonlinear Controller Based Direct Torque and Flux Control of IPMSM Drive with Reduced Torque Ripple," IEEE IAS Annual Meeting 2016, Portland, OR, USA.